

CAPITAL UNIVERSITY OF SCIENCE AND  
TECHNOLOGY, ISLAMABAD



**Effect of Linear Thermal  
Radiation and  
Magnetohydrodynamics on  
Non-Newtonian Fluids**

by

**Shahzada Muhammad Atif**

A thesis submitted in partial fulfillment for the  
degree of Doctor of Philosophy

in the

Faculty of Computing

Department of Mathematics

2020

# Effect of Linear Thermal Radiation and Magnetohydrodynamics on Non-Newtonian Fluids

By

Shahzada Muhammad Atif  
(DMT161001)

Prof. Dr. Ishak Hashim

Universiti Kebangsaan Malaysia, Malaysia (Foreign Evaluator 1)

Dr. Masoud Nickaeen

Assistant Professor, Center for Cell Analysis & Modeling, Farmington,  
USA (Foreign Evaluator 2)

Dr Shafqat Hussain

(Thesis Supervisor)

Dr. Muhammad Sagheer

(Head, Department of Mathematics)

Dr. Muhammad Abdul Qadir

(Dean, Faculty of Computing)

DEPARTMENT OF MATHEMATICS  
CAPITAL UNIVERSITY OF SCIENCE AND TECHNOLOGY  
ISLAMABAD

2020

Copyright © 2020 by Shahzada Muhammad Atif

All rights reserved. No part of this thesis may be reproduced, distributed, or transmitted in any form or by any means, including photocopying, recording, or other electronic or mechanical methods, by any information storage and retrieval system without the prior written permission of the author.

DEDICATED TO  
**My Beloved Father and Family**

All this became possible just because  
of their prayers and cooperation



**CAPITAL UNIVERSITY OF SCIENCE & TECHNOLOGY  
ISLAMABAD**

Expressway, Kahuta Road, Zone-V, Islamabad  
Phone:+92-51-111-555-666 Fax: +92-51-4486705  
Email: [info@cust.edu.pk](mailto:info@cust.edu.pk) Website: <https://www.cust.edu.pk>

**CERTIFICATE OF APPROVAL**

This is to certify that the research work presented in the thesis, entitled “**Effect of Linear Thermal Radiation and Magnetohydrodynamics on Non-Newtonian Fluids**” was conducted under the supervision of **Dr. Shafqat Hussain**. No part of this thesis has been submitted anywhere else for any other degree. This thesis is submitted to the **Department of Mathematics, Capital University of Science and Technology** in partial fulfillment of the requirements for the degree of Doctor in Philosophy in the field of **Mathematics**. The open defence of the thesis was conducted on **July 16, 2020**.

**Student Name :** Mr. Shahzada Muhammad Atif  
(DMT161001)

The Examining Committee unanimously agrees to award PhD degree in the mentioned field.

**Examination Committee :**

(a) External Examiner 1: Dr. Muhammad Ayub,  
Professor  
HITEC University, Taxila

(b) External Examiner 2: Dr. Mazhar Hussain,  
Professor  
FAST-NUCES, Islamabad

(c) Internal Examiner : Dr. Muhammad Sagheer  
Professor  
CUST, Islamabad

**Supervisor Name :** Dr. Shafqat Hussain  
Associate Professor  
CUST, Islamabad

**Name of HoD :** Dr. Muhammad Sagheer  
Professor  
CUST, Islamabad

**Name of Dean :** Dr. Muhammad Abdul Qadir  
Professor  
CUST, Islamabad

## AUTHOR'S DECLARATION

I, **Mr. Shahzada Muhammad Atif (Registration No. DMT-161001)**, hereby state that my PhD thesis titled, '**Effect of Linear Thermal Radiation and Magnetohydrodynamics on Non-Newtonian Fluids**' is my own work and has not been submitted previously by me for taking any degree from Capital University of Science and Technology, Islamabad or anywhere else in the country/ world.

At any time, if my statement is found to be incorrect even after my graduation, the University has the right to withdraw my PhD Degree.



**(Mr. Shahzada Muhammad Atif)**

Dated: 16 July, 2020

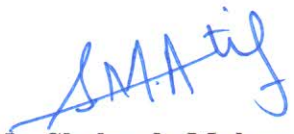
Registration No : DMT-161001

## PLAGIARISM UNDERTAKING

I solemnly declare that research work presented in the thesis titled “**Effect of Linear Thermal Radiation and Magnetohydrodynamics on Non-Newtonian Fluids**” is solely my research work with no significant contribution from any other person. Small contribution/ help wherever taken has been duly acknowledged and that complete thesis has been written by me.

I understand the zero tolerance policy of the HEC and Capital University of Science and Technology towards plagiarism. Therefore, I as an author of the above titled thesis declare that no portion of my thesis has been plagiarized and any material used as reference is properly referred/ cited.

I undertake that if I am found guilty of any formal plagiarism in the above titled thesis even after award of PhD Degree, the University reserves the right to withdraw/ revoke my PhD degree and that HEC and the University have the right to publish my name on the HEC/ University Website on which names of students are placed who submitted plagiarized thesis.

  
(Mr. Shahzada Muhammad Atif)

Dated: 16 July, 2020

Registration No : DMT-161001

---

## *List of Publications*

It is certified that following publications have been made out of the research work that has been carried out for this thesis:-

1. **S. M. Atif**, S. Hussain, M. Sagheer, “Effect of thermal radiation and variable thermal conductivity on MHD squeezed flow of Carreau fluid over a sensor surface,” *Journal of Nanofluids*, vol. 8, pp. 806- 816, 2019.
2. **S. M. Atif**, S. Hussain, M. Sagheer, “Effect of viscous dissipation and Joule heating on MHD radiative tangent hyperbolic nanofluid with convective and slip conditions”, *Journal of the Brazilian Society of Mechanical Sciences and Engineering*, vol. 41(4), pp.189-206, 2019
3. **S. M. Atif**, S. Hussain, M. Sagheer, “Heat and mass transfer analysis of time-dependent tangent hyperbolic nanofluid flow past a wedge,” *Physics Letters A*, vol. 383(11), pp. 1187-1198, 2019
4. **S. M. Atif**, S. Hussain, M. Sagheer, “Magnetohydrodynamic stratified bio-convective flow of micropolar nanofluid due to gyrotactic micro-organisms,” *AIP Advances*, vol. 9(2), 025208, 2019

**Shahzada Muhammad Atif**

(Registration No. DMT161001)



## *Acknowledgements*

I am thankful to my Creator Allah Subhana-Watala, to have guided me throughout this work at every step and for every new thought which He setup in my mind to improve it. Indeed I could have done nothing without His priceless help and guidance. Who so ever helped me throughout the course of my thesis, whether my family or any other individual was His will. So indeed none be worthy of praise but Allah.

May blessings be upon Prophet Muhammad (peace be upon Him) after whom there is no other Prophet. Bundles of thanks to Prophet (peace be upon Him), who by religion makes it imperative for us to seek education by stating “it is obligatory for every muslim man and woman to seek knowledge from cradle to grave”. Prophet (peace be upon Him) is always a source of courage and hope for me.

I owe honour, gratitude and indebtedness to my accomplished supervisor and mentor **Dr. Shafqat Hussain**, Associate Professor, Capital University of Science and Technology, Islamabad, whose affectionate guidance, authentic supervision, keen interest and ingenuity was a source of inspiration for commencement, advancement and completion of the present study.

A lot of appreciation is extended to **Dr. Muhammad Sagheer**, for his devotion, commitment, dedication and help during this project. He provided me with the opportunity to learn the method that finally led to complete this thesis. I express my heartiest and deepest thanks to all my lab fellows who were there in the lab during my PhD session. I take great pride to mention the unresisting support that came from my family throughout this process. I hope that I will be able to open new vistas for the others through this dissertation and inspire countless souls.

## *Abstract*

In this dissertation, boundary layer flow of Carreau fluid flow over a sensor surface in a squeezed channel, micropolar fluid past a vertically stretching sheet in the presence of gyrotactic micro-organisms and tangent hyperbolic fluid past a stretching sheet and a wedge have been analyzed with some realistic effects. To enhance the thermophysical properties the concept of nanoparticles has been used in few cases. In all the problems, Buongiorno model has been used to study the flow fields. The effect of magnetohydrodynamics in fluid mechanics is used to modified the flow fields in the desired direction. In the study of heat transfer, the effect of thermal radiation phenomenon is significantly important and cannot be ignored. In all problems the magnetohydrodynamics and linear thermal radiation effects have been considered. Furthermore, the Joule heating, viscous dissipation effect, convective and slip boundary conditions, stratification, suction and injection parameters have been considered in different discussed problems.

Modeled equations are based on the conservation laws under the boundary layer approximation in the form of differential equations. With the assistance of appropriate similarity transformation, the governing set of partial differential equations are rendered into nonlinear ordinary differential equations. In all problems the resulting ordinary differential equations are solved with the help of the well known shooting technique along with the Runge-Kutta integration scheme of order four. In all problems the authentication of the computed results is obtained through benchmark with the previously reported cases in the literature. The present computations of all the problems have good concord with the results of the published articles. The influence of various pertinent parameters on the velocity, temperature and concentration profiles has been analyzed graphically and discussed in detail. The quantities of interest like the skin friction coefficient, the Nusselt number and Sherwood number are also computed and analyzed.

# Contents

<b>Author's Declaration</b>	<b>v</b>
<b>Plagiarism Undertaking</b>	<b>vi</b>
<b>List of Publications</b>	<b>vii</b>
<b>Acknowledgements</b>	<b>viii</b>
<b>Abstract</b>	<b>ix</b>
<b>List of Figures</b>	<b>xiv</b>
<b>List of Tables</b>	<b>xvi</b>
<b>Symbols</b>	<b>xvii</b>
<b>1 Introduction</b>	<b>1</b>
1.1 Literature Review . . . . .	2
1.1.1 Tangent Hyperbolic Fluids . . . . .	3
1.1.2 Carreau Fluids . . . . .	4
1.1.3 Micropolar Fluids . . . . .	5
1.1.4 Magnetohydrodynamics . . . . .	6
1.1.5 Nanofluids . . . . .	7
1.1.6 Stagnation Point . . . . .	9
1.1.7 Thermal Radiation . . . . .	10
1.1.8 Microcantilever Sensor Surface . . . . .	10
1.1.9 Gyrotactic Micro-Organism . . . . .	11
1.2 The Structure of the Thesis . . . . .	14
<b>2 Preliminaries</b>	<b>16</b>
2.1 Boundary Layer Phenomenon . . . . .	16
2.1.1 Drag [85] . . . . .	16
2.1.2 Skin Friction [85] . . . . .	16
2.2 Fundamental Laws . . . . .	17
2.2.1 Mass Conservation [86] . . . . .	17

2.2.2	Momentum Equation(Law of Conservation of Linear Momentum) [86]	18
2.2.3	Energy Equation (Energy Conservation Law) [86]	18
2.3	Non-Newtonian Fluids [87]	19
2.3.1	Tangent Hyperbolic Fluids [3–8]	20
2.3.2	Carreau Fluids [13–15]	21
2.4	Micropolar Fluids [16]	22
2.5	Nanofluids [88]	23
2.5.1	Buongiorno Model [89]	25
2.6	Magnetohydrodynamics (MHD) [90]	27
2.7	Gyrotactic Micro-Organism [71–77]	29
2.8	Microcantilever Sensor [91]	30
2.9	Shooting Method [92]	31
<b>3</b>	<b>MHD Driven Flow of Carreau Fluid over a Sensor Surface</b>	<b>34</b>
3.1	Problem Formulation	34
3.2	Quantities of Interest	38
3.2.1	The Surface Drag and Nusselt Number	38
3.3	Implementation of the Numerical Scheme	38
3.3.1	Validation of Code	39
3.4	Results and Discussion	40
3.4.1	The Skin Friction Coefficient and Nusselt Number	40
3.4.2	Effect of Squeezed Flow Parameter $b$	42
3.4.3	Effect of Magnetic Number $M$	42
3.4.4	Effect of Suction/Injection Parameter $f_0$	43
3.4.5	Effect of Power-Law Index $n$	44
3.4.6	Effect of Weissenberg Number $We$	45
3.4.7	Effect of Thermal Conductivity Parameter $\epsilon$ and Thermal Radiation Parameter $Rd$	46
3.5	Conclusions	46
<b>4</b>	<b>MHD Tangent Hyperbolic Nanofluid Flow with Slip and Convective Conditions</b>	<b>48</b>
4.0.1	Problem Formulation	49
4.1	Quantities of Interest	51
4.1.1	The Skin Friction Coefficient	52
4.1.2	The Nusselt Number	52
4.2	Implementation of the Numerical Scheme	53
4.2.1	Validation of Code	54
4.3	Results and Discussion	54
4.3.1	The skin friction coefficient	54
4.3.2	The Nusselt Number	55
4.3.3	Effect of Weissenberg Number $We$	56
4.3.4	Effect of Magnetic Number $M$	57
4.3.5	Effect of Power-Law Index $n$	58

---

4.3.6	Effect of Slip Parameter $\delta$	59
4.3.7	Effect of Biot Number $Bi$	60
4.3.8	Effect of Prandtl Number $Pr$	61
4.3.9	Effect of Thermal Conductivity Parameter $\epsilon$	62
4.3.10	Effect of Thermal Radiation Parameter $Rd$	62
4.3.11	Effect of Eckert Number $Ec$	63
4.3.12	Effect of Thermophoresis Parameter $Nt$	64
4.4	Conclusions	65
<b>5</b>	<b>Heat and Mass Transfer Analysis of Time-Dependent Tangent Hyperbolic Nanofluid Flow Past a Wedge</b>	<b>66</b>
5.1	Problem Formulation	66
5.2	Quantities of Interest	69
5.2.1	The Skin Friction Coefficient	69
5.2.2	The Nusselt Number	70
5.2.3	The Sherwood Number	70
5.3	Implementation of the Numerical Scheme	71
5.3.1	Validation of Code	72
5.4	Results and Discussion	73
5.4.1	The Skin Friction Coefficient	73
5.4.2	The Nusselt Number	74
5.4.3	The Sherwood Number	75
5.4.4	Effect of Unsteadiness Parameter $A$	76
5.4.5	Effect of Magnetic Parameter $M$	77
5.4.6	Effect of Weissenberg Number $We$	78
5.4.7	Effect of Power-Law Index $n$	79
5.4.8	Effect of Thermophoresis Parameter $Nt$	80
5.4.9	Effect of Brownian Motion Parameter $Nb$	81
5.4.10	Effect of Thermal Radiation Parameter $Rd$	82
5.4.11	Effect of Generalized Biot Number $\gamma$	82
5.5	Conclusions	83
<b>6</b>	<b>MHD Stratified Bioconvective Flow of Micropolar Nanofluid due to Gyrotactic Micro-Organisms</b>	<b>84</b>
6.1	Problem Formulation	85
6.1.1	Quantities of Interest	88
6.2	Implementation of the Numerical Scheme	89
6.2.1	Validation of Code	90
6.3	Results and Discussion	91
6.3.1	The Skin Friction Coefficient and the Microrotation Parameter	91
6.3.2	The Nusselt Number	92
6.3.3	The Sherwood Number	94
6.3.4	The Density Number	94
6.3.5	Effect of Magnetic Number $M$	96
6.3.6	Effect of Material Parameter $K$	97

---

6.3.7	Effect of Mix Convection Parameter $\lambda^*$ . . . . .	98
6.3.8	Effect of Buoyancy Ratio Parameter $Nr$ . . . . .	99
6.3.9	Effect of Thermal Stratification Parameter $S$ . . . . .	100
6.3.10	Effect of Thermal Radiation Parameter $Rd$ . . . . .	102
6.3.11	Effect of Thermophoresis Parameter $Nt$ . . . . .	102
6.3.12	Effect of Brownian Motion Parameter $Nb$ . . . . .	103
6.3.13	Effect of Mass Stratification Parameter $Q$ . . . . .	105
6.3.14	Effect of Concentration Difference Parameter $\Omega$ and Peclet Number $Pe$ . . . . .	105
6.4	Conclusions . . . . .	106
<b>7</b>	<b>Conclusions and Future Work</b> . . . . .	<b>108</b>
7.1	Conclusions . . . . .	108
7.2	Future Work . . . . .	110
	<b>Bibliography</b> . . . . .	<b>111</b>

# List of Figures

1.1	Types of time dependent fluid behaviour. . . . .	3
2.1	Boundary layer thickness over a flat surface. . . . .	17
2.2	Working of cantilever . . . . .	31
3.1	Schematic illustration of the physical problem. . . . .	35
3.2	Impact of $b$ on (a) velocity and (b) temperature profile. . . . .	42
3.3	Impact of $M$ on (a) velocity and (b) temperature profile. . . . .	43
3.4	Impact of $f_0$ on velocity and temperature profile. . . . .	44
3.5	Impact of $n$ on (a) velocity and (b) temperature profile. . . . .	45
3.6	Impact of $We$ on (a) velocity and (b) temperature profile. . . . .	45
3.7	Impact of (a) $\epsilon$ and (b) $Rd$ on temperature profile. . . . .	46
4.1	Flow configuration. . . . .	49
4.2	Impact of $We$ on (a) velocity, (b) temperature and (c) concentration profile. . . . .	57
4.3	Impact of $M$ on (a) velocity, (b) temperature and (c) concentration profile. . . . .	58
4.4	Impact of $n$ on (a) velocity, (b) temperature and (c) concentration profile. . . . .	59
4.5	Impact of $\delta$ on (a) velocity, (b) temperature and (c) concentration profile. . . . .	60
4.6	Impact of $Bi$ on (a) temperature and (b) concentration profile. . . . .	61
4.7	Impact of $Pr$ on (a) temperature and (b) concentration profile. . . . .	61
4.8	Impact of $\epsilon$ on (a) temperature and (b) concentration profile. . . . .	62
4.9	Impact of $Rd$ on (a) temperature and (b) concentration profile. . . . .	63
4.10	Impact of $Ec$ on (a) temperature and (b) concentration profile. . . . .	63
4.11	Impact of $Nt$ on (a) temperature and (b) concentration profile. . . . .	64
5.1	Geometrical illustration of the problem. . . . .	67
5.2	Impact of $A$ on (a) velocity, (b) temperature and (c) concentration profile. . . . .	77
5.3	Impact of $M$ on (a) velocity, (b) temperature and (c) concentration profile. . . . .	78
5.4	Impact of $We$ on (a) velocity, (b) temperature and (c) concentration profile. . . . .	79

---

5.5	Impact of $n$ on (a) velocity, (b) temperature and (c) concentration profile. . . . .	80
5.6	Impact of $Nt$ on (a) temperature and (b) concentration profile. . . . .	80
5.7	Impact of $Nb$ on (a) temperature and (b) concentration profile. . . . .	81
5.8	Impact of $Rd$ on (a) temperature and (b) concentration profile. . . . .	82
5.9	Impact of $\gamma$ on (a) temperature and (b) concentration profile. . . . .	83
6.1	Schematic illustration of the physical problem. . . . .	85
6.2	Impact of $M$ on (a) velocity, (b) angular velocity, (c) temperature and (d) motile density profile. . . . .	97
6.3	Impact of $K$ on (a) velocity, (b) angular velocity, (c) temperature and (d) concentration profile. . . . .	98
6.4	Impact of $\lambda^*$ on (a) velocity, (b) temperature, (c) concentration and (d) motile density profile. . . . .	99
6.5	Impact of $Nr$ on (a) velocity, (b) temperature, (c) concentration and (d) motile density profile. . . . .	100
6.6	Impact of $S$ on (a) velocity, (b) temperature and (c) concentration profile. . . . .	101
6.7	Impact of $Rd$ on (a) temperature and (b) concentration profile. . . . .	102
6.8	Impact of $Nt$ on (a) temperature, (b) concentration and (c) motile density profile. . . . .	103
6.9	Impact of $Nb$ on (a) temperature, (b) concentration and (c) motile density profile. . . . .	104
6.10	Impact of $Q$ on (a) temperature and (b) concentration profile. . . . .	105
6.11	Impact of $\Omega$ and $Pe$ on concentration profile. . . . .	106



# List of Tables

3.1	Comparison of $C_f Re_x^{1/2}$ values against different values $We$ and $n$ .	40
3.2	Variation in the $C_f Re_x^{1/2}$ and $Nu_x Re_x^{-1/2}$ for different physical parameters.	41
4.1	Comparison of the presently computed values of $C_f Re_x^{1/2}$ .	54
4.2	Variation in the $C_f Re_x^{1/2}$ due to different values $M, We, n$ and $\delta$ when $Bi = Pr = 2, Ec = 0.2, Le = 5, Nb = Nt = 0.5, Rd = 0.8, \epsilon = 0.1$ .	55
4.3	Variation in the $Nu_x Re_x^{-1/2}$ due to different values of $Nt, We, Bi, Rd, n$ , and $\epsilon$ when $M = Ec = 0.2, Le = 5, Pr = 2, Nb = 0.5, \delta = 1$ .	55
5.1	Comparison of the presently computed values of $-f''(0)$ .	72
5.2	Variation in the $C_f Re_x^{1/2} \sqrt{\frac{2}{m+1}}$ various physical parameters when $Le = Rd = Pr = 1, Nt = Nb = 0.3, \gamma = 0.1$ .	73
5.3	Variation in the $-Re_x^{-1/2} Nu_x \sqrt{\frac{2}{m+1}}$ , various physical parameters when $M = We = Le = 1, n = 0.2$ .	74
5.4	Variation in the $-Re_x^{-1/2} Sh_x \sqrt{\frac{2}{m+1}}$ for various physical parameters when $M = We = Rd = 1, n = 0.2$ .	75
6.1	Comparison of the presently computed values of $-f''(0)$ and $g'(0)$ with those of Eldabe [22] and Hsiao [25].	90
6.2	Variation in the $C_f Re_x^{1/2}$ and $g'(0)$ parameter for different parameters when $S = Q = B = \delta_1 = Nb = Nt = 0.1, \Omega = Sc = 0.2, Ec = 0.02, Pr = Pe = Lb = 1.2$ .	91
6.3	Variation in $Nu_x Re_x^{-1/2}$ for various parameters when $\Omega = Sc = 0.2, Pe = Lb = 1.2, \lambda^* = Nr = B = Rb = 0.1$ .	93
6.4	Variation in $Sh_x Re_x^{-1/2}$ for various parameters when $\Omega = K = 0.2, Pe = Pr = Lb = 1.2, Rd = 1, M = 0.05, B = Rb = Nr = \lambda^* = 0.1$ .	94
6.5	Variation in $Nn_x Re_x^{-1/2}$ for various parameters when $Pr = 1.2, \lambda^* = Nt = \delta_1 = Nb = 0.1, Rd = 1, M = 0.05, K = 0.2$ .	95

# Symbols

$B_0$	applied magnetic field
$B$	motile density stratification
$Bi$	Biot number
$b$	squeezed flow index
$b^*$	chemotaxis constant
$\tilde{C}$	fluid concentration inside the boundary layer
$\tilde{C}_\infty$	ambient concentration
$\tilde{C}_w$	concentration at the surface
$C_f$	skin friction coefficient
$C_p$	specific heat
$D$	coefficient of mass diffusivity
$D_B$	Brownian diffusion coefficient
$D_T$	thermophoresis diffusion coefficient
$D_m$	diffusion coefficient of micro-organisms
$Ec$	Eckert number
$f$	dimensionless velocity
$f_0$	permeable velocity
$Gr$	Grashof number
$h_f$	heat transfer coefficient
$j$	microinertia density
$k$	thermal conductivity
$k^*$	micro-inertia density
$K$	material parameter

---

$Le$	Lewis parameter
$Lb$	bioconvection Lewis parameter
$M$	magnetic number
$n$	power-law index
$\tilde{n}^*$	motile density of micro-organisms
$\tilde{N}$	angular velocity
$Nr$	buoyancy ratio parameter
$Nn_x$	density number
$Nu$	Nusselt number
$\tilde{p}$	pressure
$Pr$	Prandtl number
$Pe$	bioconvection Peclet number
$Q$	mass stratification parameter
$Q_0$	heat generation coefficient
$q_r$	radiative heat flux
$q_0$	heat flux
$q_w$	surface heat flux
$q_m$	local mass flux
$Rd$	thermal radiation parameter
$Rb$	Rayleigh number
$Re_x$	Reynolds number
$S$	thermal stratification parameter
$Sh_x$	Sherwood number
$t$	time
$\tilde{T}$	fluid temperature inside the boundary layer
$\tilde{T}_\infty$	ambient temperature
$\tilde{T}_w$	temperature at the surface
$\tilde{U}_e$	free stream velocity
$\tilde{u}, \tilde{v}$	velocity components
$\tilde{v}_0$	reference velocity
$\mathbf{T}$	Cauchy stress tensor

---

$We$	Weissenberg number
$W_c$	maximum swimming speed of cell

**Greek symbols**

$\alpha$	thermal diffusivity
$\epsilon$	thermal conductivity parameter
$\kappa^*$	mean absorption coefficient
$\nu$	kinematic viscosity
$\sigma^*$	Stefan-Boltzmann constant
$\Gamma$	time constant
$\rho$	fluid density
$\sigma$	electric charge density
$\eta$	dimensionless distance
$\theta$	dimensionless temperature
$\mu_0$	zero shear rate
$\mu_\infty$	infinite shear rate
$\gamma$	generalized Biot number
$\gamma^*$	average volume of a micro-organism
$\gamma_1$	spin gradient viscosity
$\lambda$	mixed convection parameter
$\Omega$	micro-organism concentration difference parameter
$\delta$	velocity slip parameter
$\delta_1$	heat generation coefficient
$\Pi$	second invariant strain rate tensor

# Chapter 1

## Introduction

In all modern devices and machinery, fluids are the essential part of the design and manufacturing. The proper understanding and utilization of the fluid mechanics help to design various structures and devices in engineering and industry. The field of magnetohydrodynamics (MHD) plays a vital role in engineering and industrial applications like thermal protection, targeted drug delivery, pumps and power generation etc. The phenomenon of MHD has common interaction in nature and certain devices. For example magnetohydrodynamic flow occurs in earth interior, stars and sun. Many laboratory devices have been made to interact MHD directly such as fluid electromagnetic field, propulsion units and electrical discharges etc. The application of MHD has great significance in biomedical field such as magnetic resonance imaging (MRI), targeted drug delivery and electrocardiogram (ECG) etc. [1, 2].

Thermal radiations are conducted through the electromagnetic waves. The energy is transferred due to temperature difference between the two surfaces. In this process the energy is spread in the form of waves in all directions. The emission of these radiations depends on temperature surface, nature of surface and frequency of radiations. If the temperature difference is small then the linear thermal radiation is applicable, however if the difference of temperature is large then linear thermal radiation is not applicable. In recent years, many researchers focused

on the utilization of the magnetohydrodynamics along with the thermal radiation phenomenon to study the heat and mass transfer analysis due to its diversified applications.

Transfer of heat is one of the most challenging work in the field of engineering and industries. In ordinary fluids, the transfer of heat is not as efficient as in nanofluids. Base fluid containing nanometer size particles are called the nanofluids. In the last two decades, many researchers paid serious attention on the nanofluids. Nanofluids have ability to improve heat transfer as compared to the base fluids. Numerous experimental and theoretical studies were presented in this regard.

In this dissertation we have considered the linear thermal radiation along the magnetohydrodynamics to analyze the flow fields with different non-Newtonian fluids. Geometries like squeezed channel, linear stretching sheet and wedge shaped structures have been considered.

## 1.1 Literature Review

In engineering and industrial applications, non-Newtonian fluids being ubiquitous have been inspected extensively. Due to the limitation of the fluid models it is not possible to describe the fluid properties of the extensive class of non-Newtonian fluids by a single model. There are several non-Newtonian fluid models presented in the literature. The simplest fluid model in this regard is power-law fluid but this model has limitations because it cannot predict the flow properties in lower and upper Newtonian regions accurately. Moreover small change in the viscosity is not ignorable in certain phenomena such as polymer processing and lubrication problems etc. Generally non-Newtonian fluids have an intricate constitutive relationships. These fluids have nonlinear relation between stress and strain in rheology and between heat current and temperature gradient in thermodynamics. Due to flow diversity, a single mathematical model cannot incorporate all the rheological fluid properties.

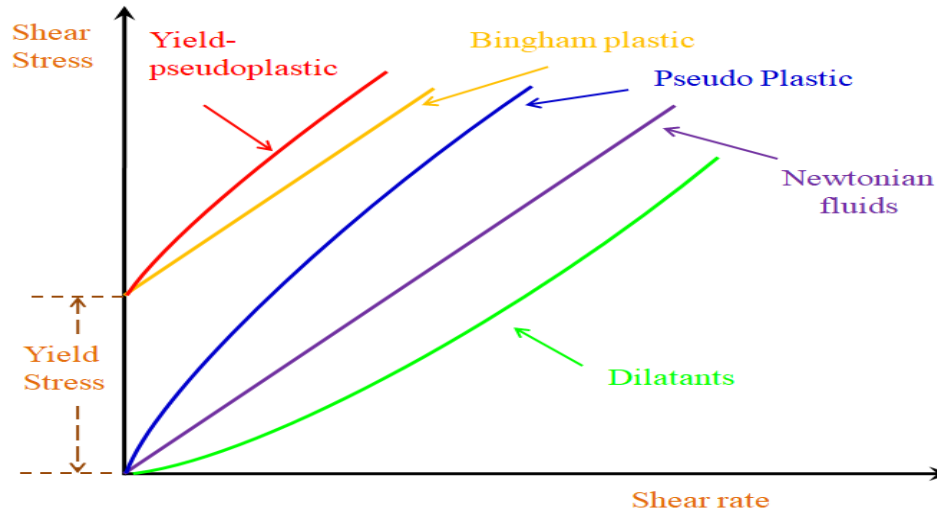


**Fig. 1.1:** Types of time dependent fluid behaviour.

A variety of fluid models addressing different fluid features, are available in the literature. A few of them are discussed here.

### 1.1.1 Tangent Hyperbolic Fluids

One of the non-Newtonian fluids is tangent hyperbolic fluid which has capability to describe the shear thinning phenomenon. Few of the examples may include blood, paints, ketchup, lava, and whipped cream etc. The advantages of this model over the other models are due to its simplicity, computational ease and physical robustness. Furthermore, kinetic theory of liquids is used to derive its constitutive relation rather than the empirical relation. Laboratory experiments show that shear thinning behaviour can be described very precisely by this model and description of the blood is a very good example of this model [3–8]. By considering the Biot number effect, Gaffar *et al.* [3] scrutinized the heat transfer in tangent hyperbolic fluid from a sphere and reported that the fluid motion, temperature, surface drag coefficient and heat transfer rate were escalated for the growing values of the Biot number. With partial slip and free convection effects in a vertical porous sheet, Prasad *et al.* [4] reported that the slip velocity is enhanced but the Nusselt number is declined as the slip parameter is enhanced. Kumar *et al.* [5] investigated the tangent hyperbolic fluid along with fluid suspended particles past

a stretching surface. A concluding remark was that an enhancement in the melting parameter results a decline in the thermal boundary layer thickness. Ibrahim [6] investigated the magnetohydrodynamic tangent hyperbolic fluid with nanoparticles past a stretching sheet. He considered the convective and second order slip boundary conditions. A key observation was that the surface drag coefficient was reduced as the value of the Weissenberg number is enhanced. Stagnation point flow of tangent hyperbolic fluid, impinging on a stretching cylinder with nanoparticles was analyzed by Salahuddin *et al.* [7]. Their concluding remark was that both Nusselt and Sherwood numbers are escalated as the velocity ratio parameter is intensified. In nonlinear stretching sheet, numerical investigation of MHD tangent hyperbolic nanofluid with viscous dissipation effect and convective conditions was observed by Hussain *et al.* [8]. They reported that the fluid motion decreases more prominently for magnetic number as compared to the nonlinearity parameter. Hayat *et al.* [9] analyzed the MHD tangent hyperbolic nanofluid past a stretching sheet of variable thickness and reported that the rate of heat transfer was enhanced as the power-law index is increased. By considering a permeable cylinder, Nagendramma *et al.* [10] deliberated the double stratified magnetohydrodynamic tangent hyperbolic fluid flow with nanoparticles and reported that the dimensionless concentration field is appreciated as the Weissenberg number is amplified but depreciated for an increment in the Lewis number.

### 1.1.2 Carreau Fluids

The power-law Carreau fluid is another non-Newtonian fluid which can characterize the low and high shear rates. The Carreau fluid behaves like generalized Newtonian fluid at low shear rate and as a power-law fluid at high shear rate. Squeezed Carreau fluid flow of a solid sphere was investigated numerically and verified experimentally by Ud-din *et al.* [11]. A key finding was that if the distance between wall and sphere is small then the radial velocity either diverges or it reaches the greatest value and then decreases rapidly to zero as the sphere comes to rest for a non-zero distance from the wall. Carreau fluid past a convectively



heated stretching sheet was ascertained by Hayat *et al.* [12] and noticed that the fluid motion was declined as the suction parameter is hiked. Khan *et al.* [13] analyzed that the energy profile was amplified as the radiation parameter is enhanced in 3D Carreau fluid flow. In a melting surface of variable thickness and with non Fourier model, Ramadevi *et al.* [14] presented the analysis of the magnetohydrodynamics Carreau fluid and observed that the thermal profile was enhanced for the rising values of the power-law index. Khan *et al.* [15] scrutinized the entropy generation in Carreau nanofluid flow and noticed an increment in entropy as the Brinkman number is hiked.

### 1.1.3 Micropolar Fluids

Micropolar fluids are characterized as the fluids having micro structures. Analysis of the micropolar fluids has been an active field of interest for many researchers. Eringen [16, 17] highlighted and developed the applications of micropolar theory due to which many researchers paid attention towards the micropolar fluids. Soundalgekar and Takhar [18] studied the micropolar fluid and found that the growing values of the coupling constant causes an increase in the micro-rotation distribution. The effect of thermal radiation on non-moving plates was discussed by Perdikis and Raptis [19]. Ishak [20] studied the micropolar fluid with thermal radiation effect. A major finding was that the heat transfer was reduced due to the thermal radiation factor. With transverse magnetic field and suction effects, Murthy *et al.* [21] examined the steady flow of micropolar fluid in a rectangular channel. One of the observations was that the volumetric flow rate of micropolar fluids is less than that of viscous fluids. In a stretching sheet, Eldabe and Ouaf [22] ascertained the hydromagnetic micropolar fluid flow with Ohmic and viscous dissipation effects. They used the Chebyshev finite difference method and noticed that the thermal profile was reduced as the Prandtl number gets higher. The effect of melting and thermal radiation on MHD micropolar fluid past a shrinking sheet was ascertained by Das *et al.* [23]. One of the main finding of this research was that an acclivity in the melting and thermal radiation parameters causes a reduction in

the drag coefficient whereas a reverse effect was observed for magnetic number and shrinking parameters. Bilal *et al.* [24] reported the magneto micropolar nanofluid using the variable thermal diffusivity, Hall and ion-slip effects. A key observation of this research was that an increment in the thermal radiation reduces the fluid motion. By considering the viscous effects, Hsiao [25] obtained the solution of the magnetohydrodynamic micropolar nanofluid flow past a stretching sheet and reported that the Nusselt number was enhanced for an acclivity in each of the Prandtl and Eckert numbers.

#### 1.1.4 Magnetohydrodynamics

Swedish electrical engineer and plasma physicist Alfvén [26] was the first to introduce the magnetohydrodynamics fluid flow. He won the Nobel prize in Physics on his work of MHD in 1970. He described the class of magnetohydrodynamics waves, which are now known as “Alfvén waves”. The magnetohydrodynamic flow has a cardinal and practical significance in engineering and industrial applications especially in fluid dynamics, metallurgical science, aerodynamics, metal working processes, micro-electro mechanical systems (MEMS), magnetic drug target and many engineering disciplines such as biomedical engineering, heat exchangers and ceramic engineering etc [27]. The objective of the induction of MHD is to modify the flow fields in a favourable direction. In convection processes, such as metal casting, control reactor in nuclear reactors and material manufacturing fields application of the MHD plays a significant role. With the temperature jump and velocity slip, Zheng *et al.* [28] analyzed the magnetohydrodynamic flow past a porous sheet. The main observation of this research was that the temperature profile was observed to decline as the porosity parameter enhanced. Bhattacharyya [29] ascertained the stagnation point MHD Casson fluid flow with thermal radiation effect and reported that an acclivity in Casson parameter reduces the wall skin friction. Chauhan and Agrawal [30] studied the MHD flow in a channel. The considered channel was bounded by a shrinking sheet and a porous bed and concluded that the magnetic number and suction parameter control the cooling rate.

Fathizadeh *et al.* [31] reported the numerical solution of magnetohydrodynamic viscous flow by modified homotopy perturbation method. Abbasbanday *et al.* [32] considered the Oldroyd-B fluid with magnetic effects and reported the solution of Falkner-Skan flow equation. They observed that the velocity components have reverse effects in relaxation and retardation time parameters. With mixed convection, Das *et al.* [33] observed the magnetohydrodynamic flow with viscous and Ohmic effects. One of the concluding remark of this study was that the fluid velocity and thermal profile are enhanced as the thermal buoyancy force is increased. Khalili *et al.* [34] ascertained the unsteady pseudoplastic nanofluid past a stretching wall. The main conclusion of this research work was that the surface drag coefficient is lower in dilatants as compared to pseudoplastic fluids. Hussain [35] explored the finite element solution of the magnetohydrodynamics nanofluid with chemical reaction while flowing through a porous medium. He found that the fluid motion is declined with an increment in the magnetic parameter. The improved results for the global wellposedness for Hall-MHD equations were determined by Kwak and Lkhagvasuren [36]. Rahbari *et al.* [37] discussed the analytical solution of the MHD Maxwell fluid between parallel plates and concluded that the velocity patterns were marginally increased as the Deborah number is hiked. Kumar *et al.* [38] explored the magnetohydrodynamic radiative Casson fluid flow with mixed convection and cross diffusion effects past a vertical plate. It was concluded that an acclivity in each of the buoyancy force and the mixed convection parameters enriches the fluid motion.

### 1.1.5 Nanofluids

The requirement of the heat transfer in small-sized and efficient electronic devices is continuously increasing day by day. The cooling process is one of the hard challenges faced in the industries related to automotive and electronic devices. In this regard, plentiful theoretical and experimental research based works have been presented by engineers and researchers to intensify the heat transfer phenomenon. The recent developments in the nanoscale technology and materials are emerged

as an embryonic field of science for the recent researchers. It is experimentally verified that heat transport phenomenon is essential for the supremacy of multiscale constructions. Mixture of some nanometer sized particles and some base fluids are called as nanofluids, have attained rattling attention due to their remarkable thermal transport features. On comparing the thermophysical properties of the nanofluids with base fluids like mineral oils, water and ethylene glycol nanofluids have the propensity to improve the thermal transport features of the fluid. Nanoparticles have very useful characteristic of passing through the microchannels and capillaries without creating any blockage in the flow.

Choi [39] experimentally verified that the thermophysical aspects of the fluids can be meliorated by the addition of the nanoparticles. Garoosi *et al.* [40] ascertained the transfer of heat in a heat exchanger filled with nanofluids with natural convection phenomenon. It was concluded that by decreasing the size of the nanoparticles, the Nusselt number is enhanced. Raju *et al.* [41] reported the unsteady free convection MHD flow with heat absorption in an exponentially stretching sheet and found its numerical solution. A major finding of this work was that the Sherwood number was diminished as the Schmidt number is intensified. Behaviour of MHD Casson fluid flow with slip boundary was conducted by Kamran *et al.* [42]. A key observation of this work was that the slip parameter reduces the motion of the fluid. Effective Prandtl number model was considered by Rashidi and Abbas [43] and conducted the entropy generation analysis on nanofluid with slip effects. They reported that an increment in slip parameter reduces the entropy. Soid *et al.* [44] scrutinized the continuously moving needle in a nanofluid and remarked that there were dual solutions only if free stream and the motion of the needle are in opposite direction. Fakour *et al.* [45] analyzed the nanofluid thin film flow past an unsteady elastic sheet by the least squares method. It was observed that among different types of nanofluids, water-alumina nanofluid has a better rate of heat transfer. Entropy analysis of MHD squeezing nanofluid flow with non-Fourier flux model was ascertained by Akmal *et al.* [46]. It was reported that the thermal profile was declined as relaxation time is hiked. By considering

the nonlinear radiation and activation energy effects, Darcy-Forchheimer Maxwell nanofluid was observed by Sajid *et al.* [47] and reported that the Nusselt number was upsurged as the activation energy is hiked. By using Lattice Boltzmann method, Mohebbi *et al.* [48] studied the nanofluids in an extended channel surface with forced convection and analyzed that the  $CuO$ -water nanofluid performed better than  $Al_2O_3$ -water and  $TiO_2$ -water. Rashidi *et al.* [49] reviewed the generalized magnetic field effects in Burger's nanofluid flow and reported that the fluid motion was declined for Burger's model due to the extra viscoelastic effects. Feng and Kleinstreuer [50] considered the parallel disks system and discussed the nanofluid convective heat transfer. Their main concluding observation was that a higher nanoparticles volume fraction, large inlet Reynolds number, reduced disk spacing and the smaller nanoparticle diameter, augments the Nusselt number. Over an isothermal flat plate, Reddy *et al.* [51] recently investigated the entropy generation in unsteady MHD couple stress fluid. They reported that the entropy generation was upsurged with an increment in the Grashof parameters but declined as the couple stress or the magnetic number is increased. Enhanced electroosmotic flow in a nano-channel was analyzed by Bhattacharyya and Pala [52]. The concluding result of that study was that an enhancement in the span ratio between the slip and no-slip regions causes an augmentation in the average electroosmotic flow.

### 1.1.6 Stagnation Point

For the solid bodies floating, the stagnation point flow delineates the fluid motion in front of the blunt-nosed body. The idea of the stagnation point flow was introduced by Hiemenz [53] in 1911. By finding the eigenvalues, stability analysis were performed by Awaludin *et al.* [54]. The main observation was that an initial decay in the disturbance was only due to the smallest possible eigenvalue which leads towards the stability in the flow. Merkin and Pop [55] investigated the stagnation point flow past a shrinking sheet driven by Arrhenius kinetics and reported the concentration and temperature in terms of the critical parameters. Stability analysis of stagnation point flow of MHD nanofluid with suction and melting was

performed by Pop *et al.* [56]. Their stability analysis showed that only upper branch solution was stable. Agbaje *et al.* [57] reported the numerical solution of the magnetohydrodynamic stagnation point flow with spectral perturbation method. Bhatti *et al.* [58] inspected the stagnation point flow under the influence of MHD effect in a permeable shrinking sheet. For this purpose Chebyshev spectral collocation and successive linearization method was used and concluded that this method is more robust and converges more rapidly to the exact results.

### 1.1.7 Thermal Radiation

In heat transfer, thermal radiation phenomenon plays a vital role and the research community has paid serious attention. There is an essential impact of the thermal radiation phenomenon on the fluid motion and temperature in the area of dynamics and industrial progression at high temperature. If the temperature at the surface and the ambient temperature are different then the phenomenon of thermal radiation becomes more important. In linear thermal radiation, the temperature difference is assumed to be sufficiently small however, nonlinear thermal radiation is valid for all the differences. In this phenomenon, the energy spreads from a vivid surface to the absorption point in the whole region in the form of the electromagnetic waves [59–65].

### 1.1.8 Microcantilever Sensor Surface

Recently many authors focused serious attention on the sensor surface due to its importance in the biochemical reactions. Microcantilever is one of the examples of sensor which can be used to detect the DNA hybridization, the detection of proteins, hazardous agents etc. Khaled and Vafei [66] presented the squeezed hydromagnetic flow over a sensor surface. They concluded that the Nusselt number was enhanced as the free stream velocity is increased. Khan *et al.* [67] observed the behaviour of the Carreau fluid flow in the squeezed channel by varying thermal conductivity over a sensor surface. In this research work, it was noticed that the

surface drag was upsurged as the power-law index is amplified. Effect of shapes of nanoparticles on magnetohydrodynamic squeezed flow past a porous sensor was reported by Kandasamy *et al.* [68]. It was observed that the sharp shape nanoparticles enhance more heat in the squeezed nanofluid flow. Salahuddin *et al.* [69] studied the squeezed flow of Carreau Yasuda fluid past a sensor surface with MHD effects and reported that an enhancement in the Weissenberg number causes the slowness in the fluid. Hussain *et al.* [70] presented the pseudoplastic fluid flow past a sensor surface with MHD effects. A concluding remark was that the fluid motion was declined for accelerating values of squeezed flow index.

### 1.1.9 Gyrotactic Micro-Organism

Phenomenon due to the upward swimming of the micro-organisms is called bioconvection. Upward motion of these micro-organisms tends to concentrate in the upper portion of the fluid which becomes unstable due to heavy density stratification. Motile micro-organisms are self-propelled and by swimming in a specific direction in the base fluid, these micro-organism increase the density of the base fluid in response to some stimulant. Microorganisms may be oxytaxis, gyrotaxis or gravitaxis organisms. Unlike the motile micro-organisms, the nanoparticles are not self-propelled, and their motion is driven by Brownian motion and thermophoresis occurring in the nanofluid. Thus, the motion of the motile micro-organisms is independent of the motion of nanoparticles. The addition of the gyrotactic micro-organisms in the nanofluid is to enhance the stability of the suspended particles. Kuznetsov [71–73] was the first who presented the idea of the nanofluid bioconvection and also investigated the impact of the gyrotactic micro-organism on the nanofluids. Kuznetsov [72] observed that in a horizontal layer of nanofluid containing gyrotactic micro-organisms, the nanoparticles may either elevate or depress critical Rayleigh numbers, whereas the micro-organisms have a consistently destabilizing effect. By considering oxytactic motile micro-organism, bioconvection in nanofluid saturated in a porous media. He he also identified that the nanofluid stability is dictated by nanoparticles distribution, density stratification induced

by the vertical temperature gradient and also the density stratification induced by up-swimming of oxytactic micro-organisms [73]. This study has further shown that the presence of oxytactic micro-organisms decreases the nanofluid suspension stability and eliminates oscillatory instability rather than non-oscillatory instability. Xu and Pop [74] studied the mixed convection flow of a nanofluid containing gyrotactic micro-organisms in a horizontal channel and concluded that the motile density is decreased as the Schmidt number is increased for the positive Reynolds number. Raju and Sandeep [75] studied the bioconvection in MHD non-Newtonian fluid flow with cross diffusion past a rotating plate and a rotating cone and found that the rotating cone has significantly better heat and mass transfer. The motion of the gyrotactic micro-organism is microscopic (convection) and the bioconvection process is a mega scale phenomenon. Raju *et al.* [76] studied the radiative Casson fluid flow past a gyrotactic micro-organisms filled wedge and reported that the motile density profile was diminished in both suction and injection cases. Ramya and Doh [77] ascertained the hydrodynamic effect of the absorbing/emitting radiation on the micropolar liquid containing the gyrostatic micro-organisms and investigated that the motile micro-organisms density was enhanced as the bioconvection Lewis number is increased for both moving and fixed plate case.

Recently, the studies related to fluid flowing over wedge shaped bodies have got an extreme synchronic interest due to its large applications in industries and engineering. In 1931, Falkner and Skan [78] initiated this idea and presented the Falkner–Skan equation. For second grade fluid, Rajagopal *et al.* [79] reported the solution of the Falkner–Skan equation with the help of perturbation technique. Lin and Lin [80] conducted the similarity solution of heat transfer past a wedge with forced convection. By utilizing differential transform method, Kuo *et al.* [81] solved the Falkner-Skan wedge flow equation. Chamkha *et al.* [82] considered the non-isothermal wedge and studied the forced convection with MHD effect. The main finding of that study was that the surface drag coefficient was increased for the amplified wall mass parameter. Micropolar fluid flow past a wedge and a flat plate was investigated by Ishak *et al.* [83] and found its similarity solution



with the main conclusion that there are multiple solutions when boundary and the free stream move in opposite direction. With velocity slip effects, Gangana-palli *et al.* [84] deliberated the unsteady Casson fluid flow past a wedge and noticed that the Casson parameter has an increasing effect on fluid motion and temperature field. The above mentioned literature survey reflects legion studies regarding non-Newtonian fluids.

The squeezing flow in a channel in the presence of sensor surface has useful applications in the biomedical and engineering fields. Many studies were presented to analyze transfer of heat with different effects. However there are still many phenomena which can be studied with this geometry. We have studied the Carreau fluid flow with magnetic effect, thermal radiation phenomena and temperature dependent thermal conductivity. The enhancement of heat and mass transfer has significant importance in industrial and engineering applications. The insertion of the nanoparticles in the base fluids, the rate of heat and mass transfer has been improved significantly. The non-Newtonian nanofluid flow past a stretching sheet and in nose shape object has a number of applications. We have considered the tangent hyperbolic nanofluid past a linear stretching sheet and a wedge, and micropolar nanofluid with gyrotactic micro-organisms in vertical sheet. Along with nanofluid, thermal radiation and MHD effects, we have considered the Joule heating, viscous dissipation, internal heating gyrotactic micro-organisms and different boundary conditions for different geometries. Similarity transformations have been utilized to transform the PDEs into ODEs. The governing ODEs have been solved via shooting method along with Runge-Kutta of order four. Numerical results have been computed and analyzed graphically for the pertinent parameters. Results of the present study have been compared with the previously published results as a limiting case.

## 1.2 The Structure of the Thesis

This dissertation is further organised as follows;

In **Chapter 2**, boundary layer theory, some basic laws, some fluid models like Carreau fluid, tangent hyperbolic fluid, micropolar fluid, nanofluids, magneto-hydrodynamics and micro-cantilever sensor has been discussed. After this, the shooting technique which is used in all subsequent chapters is explained in detail.

**Chapter 3** is comprised of the analysis of the squeezed Carreau fluid flow passing through a horizontal sensor with magnetohydrodynamics effect. The temperature dependent thermal conductivity and linear thermal radiation has also been incorporated in the energy equation. The problem is solved with the utilization of shooting technique. For the validation of the code, computed results have been compared with the already reported results. The skin friction coefficient and the Nusselt number are computed and discussed in detail. These investigated results have been published in “Journal of Nanofluids”, Vol. 8, pp.1 – 11, (2019), DOI.org/10.1166/jon.2019.1621.

In **Chapter 4**, we analyze the magnetohydrodynamic tangent hyperbolic fluid past a stretching sheet. The temperature dependent thermal conductivity, viscous dissipation, linear thermal radiation, Ohmic and internal heating effects have also been incorporated in the energy equation. Simulations have been performed for the slip and convective boundary conditions. Problem is solved with the help of shooting technique. An authentication of the computed results is obtained through benchmark with the previously reported cases. These findings have been published in “Journal of the Brazilian Society of Mechanical Sciences and Engineering”, vol. 41(4), 2019, DOI.org/10.1007/s40430-019-1688-9.

Attention of **Chapter 5** is to inspect tangent hyperbolic fluid with nanoparticles past a wedge shape geometry. In addition the convective heating mode, magnetohydrodynamics and linear thermal radiation effect have also been incorporated.

The system of equations is solved with the aid of shooting technique. The skin friction, Nusselt and Sherwood numbers are computed and discussed. The computed results are compared with previously reported results. The results of this study have been published in “Physics Letters A”, vol. 383(11), pp. 1187 – 1198, (2019), DOI.org/10.1016/j.physleta.2019.01.003

Magnetohydrodynamic stratified micropolar bioconvective fluid containing nanoparticles and gyrotactic micro-organisms has been scrutinized in **Chapter 6**. The phenomenon of Joule heating and thermal radiation has also been incorporated. After utilizing similarity transformations, the resulting ODEs are solved by utilizing shooting method. The results are confirmed by comparing with already reported results in literature. The surface drag, Nusselt, Sherwood and density numbers are computed and discussed. The aforesaid work has been published in “AIP Advances”, vol. 9, 025208, (2019), DOI.org/10.1063/1.5085742.

**Chapter 7** comprises of conclusions of the thesis and some future directions which can be followed by extending these presented problems with some different effects and models.

# Chapter 2

## Preliminaries

### 2.1 Boundary Layer Phenomenon

#### 2.1.1 Drag [85]

“When a fluid flows around the outside of a body, it produces a force that tends to drag the body in the direction of the flow. The drag acting on a moving object such as a ship or an aeroplane must be overcome by the propulsion system. Drag takes two forms, skin friction drag and form drag.”

#### 2.1.2 Skin Friction [85]

“Skin friction drag is due to the viscous shearing that takes place between the surface and the layer of fluid immediately above it. This occurs on surfaces of objects that are long in the direction of flow compared to their height. Such bodies are called streamlined. When a fluid flows over a solid surface, the layer next to the surface may become attached to it (it wets the surface). This is called the no slip condition. The layers of fluid above the surface are moving so there must be shearing taking place between the layers of the fluid. The shear stress acting between the wall and the first moving layer next to it is called the wall shear

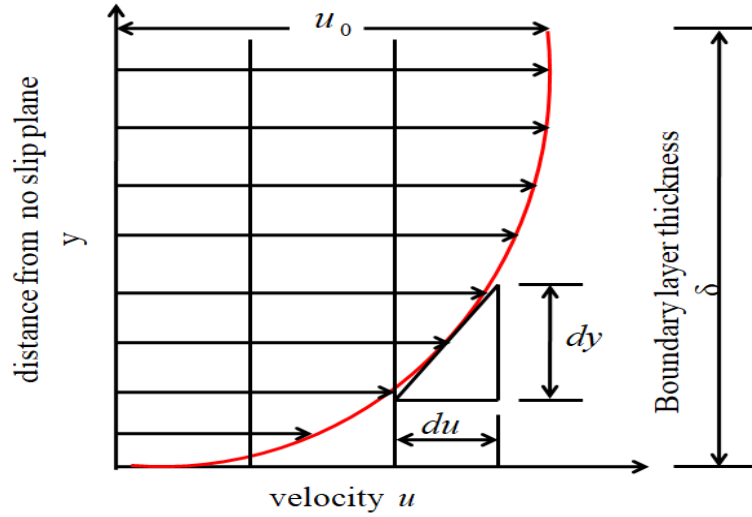


**Fig. 2.1:** Boundary layer thickness over a flat surface.

stress and denoted by  $\tau_w$ . The result is that the velocity of the fluid  $u$  increases with height  $y$ . The boundary layer thickness is taken as the distance required for the velocity to reach 99% of  $u_0$ . This layer is called the boundary layer and  $\delta$  is the boundary layer thickness. By free stream velocity  $u_0$  we mean the stream outside the influence of the boundary layer. Fig. 2.1 shows how the velocity  $u$  varies with height  $y$  for a typical boundary layer.”

## 2.2 Fundamental Laws

### 2.2.1 Mass Conservation [86]

“For any fluid, conservation of mass is expressed by the scalar equation

$$\frac{\partial \rho}{\partial t} + \nabla \cdot (\rho \mathbf{V}) = 0, \quad (2.1)$$

where  $\rho$  is density of the fluid and  $\mathbf{V}$  is the velocity field. Hence, a velocity profile represents an admissible (real) flow, if and only if it satisfies the continuity

equation. For incompressible fluids, Eq. (2.1) reduces to

$$\nabla \cdot \mathbf{V} = 0.” \quad (2.2)$$

### 2.2.2 Momentum Equation(Law of Conservation of Linear Momentum) [86]

“Law of conservation of linear momentum states that the total momentum of an isolated system remains same. It is derived from Newton’s second law of motion. For any fluid, the momentum equation is

$$\frac{\partial}{\partial t}(\rho \mathbf{V}) + \nabla \cdot [(\rho \mathbf{V})\mathbf{V}] - \nabla \cdot \mathbf{T} - \rho \mathbf{g} = 0, \quad (2.3)$$

Since  $\mathbf{T} = -p\mathbf{I} + \tau$  and applying incompressibility condition, the momentum equation takes the form

$$\rho \left( \frac{\partial \mathbf{V}}{\partial t} + \mathbf{V} \cdot \nabla \mathbf{V} \right) = -\nabla p + \nabla \cdot \tau + \rho \mathbf{g}, \quad (2.4)$$

where,  $\rho$  is density of the fluid,  $\mathbf{V}$  is the velocity field  $\mathbf{g}$  is the body force,  $p$  the pressure,  $\tau$  the shear stress tensor.

### 2.2.3 Energy Equation (Energy Conservation Law) [86]

“The law of conservation of energy (or the first law of thermodynamics) states that the time rate of change of the total energy is equal to the sum of the rate of work done by applied forces and the change of heat content per unit time.

In the general case, the first law of thermodynamics can be expressed in conservation form as

$$\rho \left[ \frac{\partial U}{\partial t} + (\mathbf{V} \cdot \nabla)U \right] = [\tau : \nabla \mathbf{V} + \rho \nabla \cdot \mathbf{V}] + \nabla \cdot (k \nabla T) \pm \hat{H}r. \quad (2.5)$$

Here  $U$  is the internal energy per unit mass, and  $\hat{H}r$  is the heat of reaction. By invoking the definition of the internal energy,  $dU = C_v dT$ , Eq. (2.5) becomes,

$$\rho C_v \left[ \frac{\partial T}{\partial t} + (\mathbf{V} \cdot \nabla)T \right] = [\tau : \nabla \mathbf{V} + \rho \nabla \cdot \mathbf{V}] + \nabla \cdot (k \nabla T) \pm \hat{H}r. \quad (2.6)$$

For heat conduction in solids, i.e., when  $\mathbf{V} = 0$ ,  $\nabla \cdot \mathbf{V} = 0$ , and  $C_v = C$ , the resulting equation is

$$\rho C \left[ \frac{\partial T}{\partial t} + (\mathbf{V} \cdot \nabla)T \right] = \nabla \cdot (k \nabla T) \pm \hat{H}r. \quad (2.7)$$

For phase change, the latent heat rate per unit volume must be added as a source term to the energy equation.”

## 2.3 Non-Newtonian Fluids [87]

“A non-Newtonian fluid is one whose flow curve is nonlinear or does not pass through the origin, i.e., where the apparent viscosity, shear stress divided by shear rate, is not constant at a given temperature and pressure but is dependent on flow conditions such as flow geometry, shear rate, etc., and sometimes even on the kinematic history of the fluid element under consideration. The most common type of time-independent non-Newtonian fluid behavior observed is pseudoplasticity or shear-thinning which is characterized by an apparent viscosity that decreases with increasing shear rate. Many mathematical expressions of varying complexity and form have been proposed in the literature to model shear-thinning characteristics and some of them are straightforward attempts at curve fitting, giving empirical relationships for the shear stress or apparent viscosity while others are theoretically based on statistical mechanics, as an extension of the application of the kinetic theory to the liquid state or the theory of rate processes, etc. Viscoplastic fluid behavior is characterized by the existence of a yield stress which has to be exceeded before the fluid deforms or flows and such a material deforms elastically or flows en masse like a rigid body when the externally applied stress is smaller than the

yield stress.”

Some of the non-Newtonian fluids are discussed here.

### 2.3.1 Tangent Hyperbolic Fluids [3–8]

“The non-Newtonian fluids have been examined extensively due to their large applications in industries and engineering. These fluids have nonlinear relation between stress and strain in rheology. These shear effects play a significant role in the analysis of the heat transfer of the non-Newtonian fluids. A tangent hyperbolic fluid is one of the non-Newtonian fluids which is capable of describing the shear thinning phenomenon. This rheological model has certain advantages over the other non-Newtonian fluids formulations including simplicity, ease of computation and physical robustness. Furthermore, it is deduced from kinetic theory of liquids rather than the empirical relation. From laboratory experiments, it is found that this model predicts shear thinning phenomenon very precisely. Additionally, this model described the blood flow very accurately.

The constitutive equation for the tangent hyperbolic fluid is given by

$$\tau = [\mu_\infty + (\mu_0 + \mu_\infty) \tanh(\Gamma\dot{\omega})^n] \dot{\omega},$$

where  $n$  is the power-law index,  $\Gamma$  is the time constant,  $\tau$  is the extra stress tensor,  $\mu_0$  and  $\mu_\infty$  represent zero and infinite shear rate viscosities respectively and  $\dot{\omega}$  is defined as

$$\dot{\omega} = \sqrt{\frac{1}{2} \sum_i \sum_j \dot{\omega}_{ij} \dot{\omega}_{ji}} = \sqrt{\frac{1}{2} \mathbf{\Pi}},$$

where  $\mathbf{\Pi} = \frac{1}{2} \text{tr} ((\text{grad } \mathbf{V}) + (\text{grad } \mathbf{V})^T)^2$ .

It is not possible to discuss the problem for the infinite shear rate viscosity therefore considering the assumption  $\mu_\infty = 0$ . As we are focusing on the shear thinning behaviour therefore for  $\Gamma\dot{\omega} < 1$ .



Under these assumptions the extra stress tensor  $\tau$  is reduced to

$$\begin{aligned}\tau &= \mu_0 \left[ (\Gamma \dot{\omega})^n \right] \dot{\omega} = \mu_0 \left[ (1 + \Gamma \dot{\omega} - 1)^n \right] \dot{\omega}, \\ &= \mu_0 \left[ 1 + n (\Gamma \dot{\omega} - 1) \right] \dot{\omega}.\end{aligned}$$

Lava, ketchup, whipped cream, blood and paints etc are the common examples of tangent hyperbolic fluid.”

### 2.3.2 Carreau Fluids [13–15]

“For the chemical engineering industry, the most important property of fluids is the non-Newtonian viscosity. The generalized Newtonian fluids are those in which the viscosity changes with the shear rate i.e. the viscosity of the fluid shows a dependence on the shear rate. The change in the viscosity by two or three orders of magnitude is feasible for some fluids and this cannot be ignored when the lubrication problems and polymer processing is considered. Therefore, one of the basic empirically obtained modifications of the Newtons law of viscosity is to allow the viscosity to change with the shear rate. The simplest generalized Newtonian fluid is the power-law constitutive relation. The power-law viscosity model has the limitation that it cannot adequately predict the viscosity for very small or very large shear rates. In view of such limitation of the power-law model, especially for very low and very high shear rates, we consider another viscosity model from the class of generalized Newtonian fluids, namely, Carreau rheological model. This model overcomes the limitations of the power-law model and appears to be gaining wider acceptance in chemical engineering and technological processes. The Carreau fluid model can well characterize the rheology of various polymeric solutions. At low shear rate Carreau fluid behaves as a Newtonian fluid and at high shear rate as a power-law fluid. For the Carreau fluid model, the Cauchy stress tensor  $\mathbf{T}$  is

$$\mathbf{T} = -p\mathbf{I} + \varsigma \mathbf{A}_1, \quad (2.8)$$

with

$$\varsigma = \mu_\infty + (\mu_0 - \mu_\infty)[1 + (\Gamma\dot{\omega})^2]^{\frac{n-1}{2}},$$

where  $\mu_0$  is the zero-shear-rate viscosity,  $\mu_\infty$  the infinite-shear-rate viscosity,  $\Gamma$  a material time constant and  $n$  expresses the power-law index. The shear rate  $\dot{\omega}$  is expressed as

$$\dot{\omega} = \sqrt{\frac{1}{2} \sum_i \sum_j \dot{\omega}_{ij} \dot{\omega}_{ji}} = \sqrt{\frac{1}{2} \mathbf{\Pi}} = \sqrt{\frac{1}{2} \text{tr } \mathbf{A}_1^2}.$$

Here  $\mathbf{\Pi}$  is the second invariant strain rate tensor and

$$\dot{\omega} = \sqrt{2 \text{tr } \mathbf{A}_1^2},$$

where

$$\mathbf{A}_1 = (\text{grad } \mathbf{V}) + (\text{grad } \mathbf{V})^T.$$

In most practical cases,  $\mu_0 \gg \mu_\infty$ . Therefore  $\mu_\infty$  is taken to be zero and consequently, Eq. (2.3.2) takes the following form

$$\mathbf{T} = -p\mathbf{I} + \mu_0[1 + (\Gamma\dot{\omega})^2]^{\frac{n-1}{2}} \mathbf{A}_1.$$

The Carreau-model with fluid index in the range  $0 < n < 1$  are commonly referred as shear thinning or pseudoplastic fluids and Carreau fluids with fluid index in the range  $n > 1$  are commonly referred as shear thickening or dilatant fluids.”

## 2.4 Micropolar Fluids [16]

“The theory of microfluids introduced by Eringen deals with a class of fluids which exhibit certain microscopic effects arising from the local structure and micro-motions of the fluid elements. These fluids can support stress moments and body

moments and are influenced by the spin inertia. The theory of microfluids are, however, too complicated even in the case of constitutively linear theory and the underlying mathematical problem is not easily amenable to the solution of non-trivial problems in this field.

A subclass of these fluids is the micropolar fluids which exhibit the micro-rotational effects and micro-rotational inertia. This class of fluids possesses certain simplicity and elegance in their mathematical formulation which should appeal to mathematicians. The micropolar fluids can support couple stress and body couples only. Physically they may represent adequately the fluids consisting of dipole elements. Certain anisotropic fluids, e.g. liquid crystals which are made up of dumbbell molecules, are of this type. In fact, animal blood happens to fall into this category. Other polymeric fluids and fluids containing minute amount additives may be represented by the mathematical model underlying micropolar fluids.”

## 2.5 Nanofluids [88]

“Cooling is one of the most important technical challenges facing numerous diverse industries including microelectronics, transportation, manufacturing, and metrology. Developments driving the increased thermal loads that require advances in cooling include faster speeds (in the multi-GHz range) and smaller features (to  $< 100$ )nm for microelectronic devices, higher power output engines, and brighter optical devices. The conventional method to increase cooling rates is to use extended surfaces such as fins and microchannels; however, current designs have already stretched this approach to its limits. Therefore, there is an urgent need for new and innovative coolants to achieve ultrahigh-performance cooling. Taking a different tack from extended surface approaches, the novel concept of nanofluids, i.e., heat transfer fluids containing suspensions of nanoparticles, has been developed to meet such cooling challenges.

Nanofluids are a new class of solid-liquid composite materials consisting of solid

nanoparticles, with sizes typically on the order of 1 – 100 nm, suspended in a heat transfer liquid. In recent years nanofluids have attracted great interest owing to their greatly enhanced thermal properties. For example, a small amount (less than 1% volume fraction) of copper nanoparticles or carbon nanotubes dispersed in ethylene glycol or oil can increase their inherently poor thermal conductivity by 40% and 150%, respectively. Conventional particle-liquid suspensions require high concentrations ( $> 10\%$ ) of particles to achieve such enhancement; they are, however, plagued by rheological and stability problems that preclude their widespread use.

In some cases, nanofluids have been demonstrated to conduct heat an order of magnitude better than predicted by conventional theories. Other exciting results in this rapidly evolving field include a surprisingly strong temperature dependence of the thermal conductivity and a threefold higher critical heat flux than that of base fluids. These anomalously enhanced thermal properties are not merely of academic interest, but make nanofluids promising for nanotechnology based cooling applications including ultrahigh thermal conductivity coolants, lubricants, hydraulic fluids, and metal-cutting fluids. Nanofluids offer several benefits: for example, higher cooling rates, decreased pumping-power needs, smaller and lighter cooling systems, reduced inventory of heat transfer fluids, reduced friction coefficient, and improved wear resistance. Furthermore, nanofluids, initially designed for engineering applications such as the development of new coolants and the miniaturization of heat exchangers, are being developed for medical applications including cancer therapy. We believe that this interdisciplinary nanofluid research presents a great opportunity to explore new frontiers in wet nanotechnology.”

After the introduction of the nanofluids by Choi [39], various nanofluid models were presented to study enhancement in the thermophysical properties, however, in 2006, two phase model was presented by Buongiorno model [89]. In the present study, we have considered the Buongiorno model [89] to study the thermophysical properties of different considered fluids.

### 2.5.1 Buongiorno Model [89]

“Contrary to the milli and microsized particle slurries explored in the past, nanoparticles are relatively close in size to the molecules of the base fluid, and thus can realize very stable suspensions with little gravitational settling over long periods of time. Materials commonly used for nanoparticles include oxides such as alumina, silica, titania and copper oxide, and metals such as copper and gold. Carbon nanotubes and diamond nanoparticles have also been used to realize nanofluids. Popular base fluids include water and organic fluids such as ethanol and ethylene glycol. The volumetric fraction of the nanoparticles, is usually below 5%. The following nanofluid behavior were observed consistently by different researchers at different organizations and with different nanofluids:

1. Abnormal thermal conductivity increase relative to the base fluid.
2. Abnormal viscosity increase relative to the base fluid.
3. Abnormal single-phase convective heat-transfer coefficient increase relative to the base fluid.

Despite several attempts, a satisfactory explanation for the abnormal increase of the thermal conductivity and viscosity in nanofluids is yet to be found, as emphasized by Eastman et al. [88] in their recent comprehensive review of the nanofluid literature.

Several authors have attempted to develop convective transport models for nanofluids. The models proposed so far are of the following two types:

1. **Homogeneous flow models:** The conventional transport equations for pure fluids are directly extended to the nanofluids. This means that all traditional heat transfer correlations could be used also for a nanofluid, provided that the nanofluid thermophysical properties were used in the calculations. Therefore, heat transfer enhancement is assumed to come only from

the higher thermal conductivity. This approach was initially adopted by Choi [39].

2. **Dispersion models:** This approach is based on the assumption that the convective heat transfer enhancement in nanofluids comes from two factors,
  - i. the higher thermal conductivity,
  - ii. the dispersion of the nanoparticles.

The homogeneous flow models are in conflict with the experimental observation. As far as the dispersion models are concerned, Buongiorno proved that the heat transfer enhancement from nanoparticle dispersion is completely negligible in nanofluids. The nanoparticle absolute velocity can be viewed as the sum of the base fluid velocity and a relative (slip) velocity. Buongiorno considered seven slip mechanisms that can produce a relative velocity between the nanoparticles and the base fluid. These slip mechanisms are inertia, Brownian diffusion, Magnus effect thermophoresis, diffusiophoresis, fluid drainage and gravity. Buongiorno concluded that, of these seven, only Brownian diffusion and thermophoresis are important slip mechanisms in nanofluids. Buongiorno considered the nanofluid as a two-component mixture (base fluid+nanoparticles) with the following assumptions:

1. incompressible flow,
2. no chemical reactions,
3. negligible external forces
4. dilute mixture (volumetric fraction of the nanoparticles  $\ll 1$ ),
5. negligible viscous dissipation,
6. negligible radiative heat transfer,
7. nanoparticles and base fluid locally in thermal equilibrium.

Buongiorno developed nanofluid model that can be characterized as a two-phase fluid (nanoparticles+base fluid), four-equation (2 mass+1 momentum+1 energy), nonhomogeneous (nanoparticle/fluid slip velocity allowed) equilibrium (nanoparticle/fluid temperature differences not allowed) model.”

## 2.6 Megnetohydrodynamics (MHD) [90]

“In MHD, the plasma is considered as an electrically conducting fluid. Governing equations are equations of fluid dynamics and Maxwell equations. A self-consistent set of MHD equations connects the plasma mass density  $\rho$  the plasma velocity  $\mathbf{V}$ , the thermodynamic (also called gas or kinetic) pressure  $P$  and the magnetic field  $\mathbf{B}$ . In strict derivation of MHD, one should neglect the motion of electrons and consider only heavy ions.

The momentum equation in the presence of magnetic field as a body force can be described as

$$\rho \left[ \frac{d\mathbf{V}}{dt} + (\mathbf{V} \cdot \nabla) \mathbf{V} \right] = -\nabla p + \mathbf{J} \times \mathbf{B}, \quad (2.9)$$

The vector  $\mathbf{J}$  is the electric current density which can be expressed through the magnetic field  $\mathbf{B}$ .

To derive the equation for the magnetic field using Maxwells equations, consider Ohm’s law

$$\mathbf{J} = \sigma \mathbf{E}', \quad (2.10)$$

where  $\sigma$  is electrical conductivity (the physical quantity inverse to the resistivity) and  $\mathbf{E}'$  is the electric field experienced by the plasma (fluid) element in its rest frame. When the plasma is moving (with respect to the external magnetic field) at the velocity  $\mathbf{V}$ , applying the Lorentz transformation we obtain

$$\mathbf{E}' = \mathbf{E} + \mathbf{V} \times \mathbf{B}. \quad (2.11)$$

Now, Eq. (2.10) can be rewritten as

$$\frac{1}{\sigma} \mathbf{J} = \mathbf{E} + \mathbf{V} \times \mathbf{B}. \quad (2.12)$$

In case of perfect conductivity,  $\sigma \rightarrow \infty$ , we have

$$\mathbf{E} = -\mathbf{V} \times \mathbf{B}. \quad (2.13)$$

Calculating the curl of the electric field  $\mathbf{E}$  and using in the Maxwell's equation,

$$\nabla \times \mathbf{E} = -\frac{\partial \mathbf{B}}{\partial t}. \quad (2.14)$$

we can exclude the electric field and obtain

$$\frac{\partial \mathbf{B}}{\partial t} = \nabla \times (\mathbf{V} \times \mathbf{B}). \quad (2.15)$$

This is the called the induction equation. In particular, this equation describes the phenomenon of magnetic dynamo.

To close the set of MHD equations, we have to express the current density  $\mathbf{j}$  through the magnetic field  $\mathbf{B}$ . Consider the other Maxwells equation,

$$\nabla \times \mathbf{B} - \frac{1}{c^2} \frac{\partial \mathbf{E}}{\partial t} = \mu_0 \mathbf{J}. \quad (2.16)$$

From Ohms law, we had  $\mathbf{E} = -\mathbf{V} \times \mathbf{B}$ . Consequently, we can estimate the electric field as  $E \sim V_0 B$ , where  $V_0$  is a characteristic speed of the process. consider the ratio of the two terms in Eq.(2.16):

$$\nabla \times \mathbf{B} \quad \text{and} \quad \frac{1}{c^2} \frac{\partial \mathbf{E}}{\partial t}. \quad (2.17)$$

The first term is very much greater than the second term, and we can neglect the second term, therefore we can write

$$\mathbf{J} = \frac{1}{\mu_0} \nabla \times \mathbf{B}. \quad (2.18)$$



In addition, the magnetic field must satisfy the condition

$$\nabla \cdot \mathbf{B} = 0.$$

Thus the close set of MHD equations is

$$\begin{aligned} \rho \frac{d\mathbf{V}}{dt} &= -\nabla p - \frac{1}{\mu_0} \mathbf{B} \times (\nabla \times \mathbf{B}), \\ \frac{\partial \mathbf{B}}{\partial t} &= \nabla \times (\mathbf{V} \times \mathbf{B}). \end{aligned}$$

These equations are ideal, which means that all the dissipative processes (finite viscosity, electrical resistivity and thermal conductivity) were neglected.”

## 2.7 Gyrotactic Micro-Organism [71–77]

“Microorganism particles are widely used to create mechanical and commercial items like ethanol, biofuel produced using waste, fertilizers and so on. They are additionally utilized in water treatment plants. Hydrogen gas and biodiesel, promising renewable power source, are created by the micro-organisms. Bioconvection is the creation of various types of random liquid patterns at the microscopic level due to the spontaneous swimming of self-propelled micro-organisms which are available in the water and in the alternate fluids denser than water. The swimming of those micro-organisms is biased by the natural phenomena like searching for nutrient, oxygen for breath, optimizing light in take for photosynthesis. The addition of gyrotactic micro-organisms into nanofluids is likely to increase its stability as a suspension. It was further found that suspensions of gyrotactic micro-organisms could exhibit bioconvection, which is a macroscopic motion in the fluid induced by up swimming or the motion of motile micro-organisms. This is due to that the motile micro-organisms are usually heavier than water so that they can swim in the upward direction in response to stimuli such as gravity, light and chemical attractions. Based on cause of impellent, the motile micro-organisms can be classified into different types of micro-organisms including oxytactic or

chemotaxis, negative gravitaxis and gyrotactic micro-organisms. The stimulators of these micro-organisms are Oxygen concentration gradient, negative gravity and the displacement between the center of buoyancy and mass, respectively”

## 2.8 Microcantilever Sensor [91]

“A cantilever is a simplest mechanical structure, which is clamped at one end and free at the other end. MEMS cantilever sensor works based on the mechanical deformation of the structure, or in other words the deflection of membrane or beam structure. When the cantilever is loaded, its stressed elements deform and the MEMS cantilever will bend. As this deformation occurs, the structure changes shape, and points on the structure displace. The concept is that deflection occurs when a disturbance or loading applied to the cantilever is free end or along the MEMS cantilever surface. To serve as a sensor, cantilever has to be coated with a sensing layer, which should be specific, i.e. able to recognize target molecules in key-lock processes. Microcantilever sensors can be operated in air, vacuum or in a liquid. One of their major limitations is that the measurement of cantilever displacement typically involves elaborate off-chip setups with free-space optics. Microcantilevers can transduce a chemical signal into a mechanical motion with high sensitivity. Microcantilever is one of these elements which is capable to accurately diagnose different diseases or can sense many perilous agents. Microcantilever turns upon the requisite target area with assistance of receptor coating. The thin fluidic cells in which microcantilever is placed are of moderately greater level of exterior squashing in the existence of external turbulences. The microcantilever transport can be formulated like the transport through horizontal surfaces. Microcantilever sensors have much distinction among the class of technological sensors due to their prompt response, high sensitivity, low cost, accurate time sensing and exquisite characteristics. These sensors found various utilizations in chemical, industrial and biological processes.”

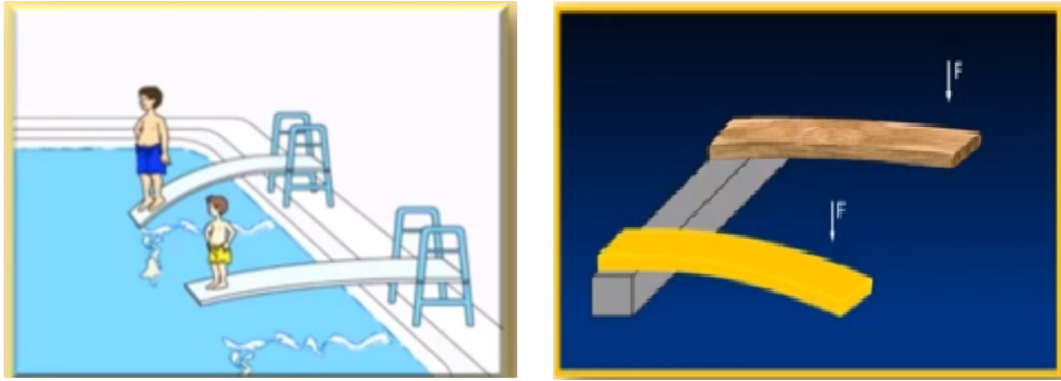


**Fig. 2.2:** Working of cantilever

Few applications of cantilever sensor are highlighted below

- Cancer detecting microchips
- Biochips
- Biosensor for coronary heart disease
- Monitoring missile storage and maintenance
- Humidity sensors
- Herbicide sensors
- Metal ion sensors etc.

## 2.9 Shooting Method [92]

“In this thesis, the formulated problems are solved by the shooting method with the Runge-Kutta of order four. The system of the governing partial differential equations (PDEs) is converted into ordinary differential equations (ODEs) by invoking similarity transformation. In order to solve the system of ODEs with the help of shooting method, the set of higher order ODEs are converted into a system of first order ODEs. To solve the system of first order ODEs with the help

of shooting method, their respective initial conditions are required. In shooting method the missing initial conditions are assumed and the accuracy is checked by comparing the calculated values with the known values of the dependent variable at the other terminal point. If there is a difference, the initial guess must be chosen again until the computed value and the known value at the other terminal point lies within the specified degree of accuracy. For the refinement of the initial guesses, the Newton's method is used. Some times shooting method diverges due to the singular Jacobian which is due to the sensitivity of the initial guesses in Newton's scheme. There is no strict rule for the selection of the successful initial guesses. For the explanation of the shooting method, a second order boundary value problem has been considered,

$$y''(x) = f(x, y, y'(x)) \quad (2.19)$$

subject to boundary conditions

$$y(0) = 0, \quad y(L) = A, \quad (2.20)$$

Now, by writing  $y = y_1$  and  $y'_1 = y_2$ , the Eq. (2.19) along with the boundary conditions (2.20) can be written as the following system of first order equations.

$$\left. \begin{aligned} y'_1 &= y_2, & y_1(0) &= 0, \\ y'_2 &= f(x, y_1, y_2), & y_1(L) &= A. \end{aligned} \right\} \quad (2.21)$$

Denote the missing initial condition  $y_2(0) = s$ , the system of the Eq. (2.20) becomes,

$$\left. \begin{aligned} y'_1 &= y_2, & y_1(0) &= 0, \\ y'_2 &= f(x, y_1, y_2), & y_2(0) &= s. \end{aligned} \right\} \quad (2.22)$$

Now the problem is to find  $s$  such that the solution of the Eq. (2.22) satisfies the boundary condition  $y(L) = A$ . In other words, if the solutions of the IVP Eq. (2.22) are denoted by  $y_1(x, s)$  and  $y_2(x, s)$  then one should search that value

of  $s$  which is an approximate root of the equation.

$$y_1(L, s) - A = \phi(s) = 0. \quad (2.23)$$

For Newton's method, the iteration formula for  $s$  is given by

$$s_{n+1} = s_n - \frac{\phi(s_n)}{d\phi(s_n)/ds},$$

or

$$s_{n+1} = s_n - \frac{y_1(L, s_n) - A}{dy_1(L, s_n)/ds}. \quad (2.24)$$

To find the derivative of  $y_1$  with respect to  $x$ , differentiating (2.22) with respect to  $s$ . For simplification, use the notations,

$$\frac{dy_1}{ds} = y_3, \quad \frac{dy_2}{ds} = y_4, \quad (2.25)$$

which results in the following IVP.

$$\left. \begin{aligned} y_3' &= y_4, & y_3(0) &= 0, \\ y_4' &= \frac{\partial f}{\partial y_1} y_3 + \frac{\partial f}{\partial y_2} y_4, & y_4(0) &= 1. \end{aligned} \right\} \quad (2.26)$$

For the solution of the IVP (2.26), the value of  $y_3$  at  $L$  can be computed which is the derivative of  $y_1$  with respect to  $s$  computed at  $L$ . Using this value of  $y_3(L, s)$  in Eq. (2.23), the value of  $s$  can be achieved. To solve the Eq. (2.23), the new value of  $s$  is used and the process is repeated until the value of  $s$  is within the degree of accuracy."

# Chapter 3

## MHD Driven Flow of Carreau Fluid over a Sensor Surface

The purpose of this study is to analyze the unsteady two dimensional MHD Carreau fluid flow passing through squeezed channel in the presence of a sensor surface. The temperature dependent thermal conductivity and phenomenon of thermal radiation have also been incorporated in the energy equation. In order to convert the PDEs of the modeled problem into system of ODEs, similarity transformations are used. The solution of resulting equations is achieved via well known shooting technique. The interesting aspects of sundry parameters on the different flow distributions are sketched and inspected in detail. The surface drag and the Nusselt number have been computed numerically. Furthermore, to claim the authentication of the code, the results of the published article in literature are compared with the present study with the conclusion of an excellent agreement.

### 3.1 Problem Formulation

Consider an incompressible unsteady two dimensional magnetically driven Carreau fluid across the squeezed channel. A microcantilever sensor of length  $l$  is placed inside the squeezed channel of height  $h(t)$ . The height of the channel is considered

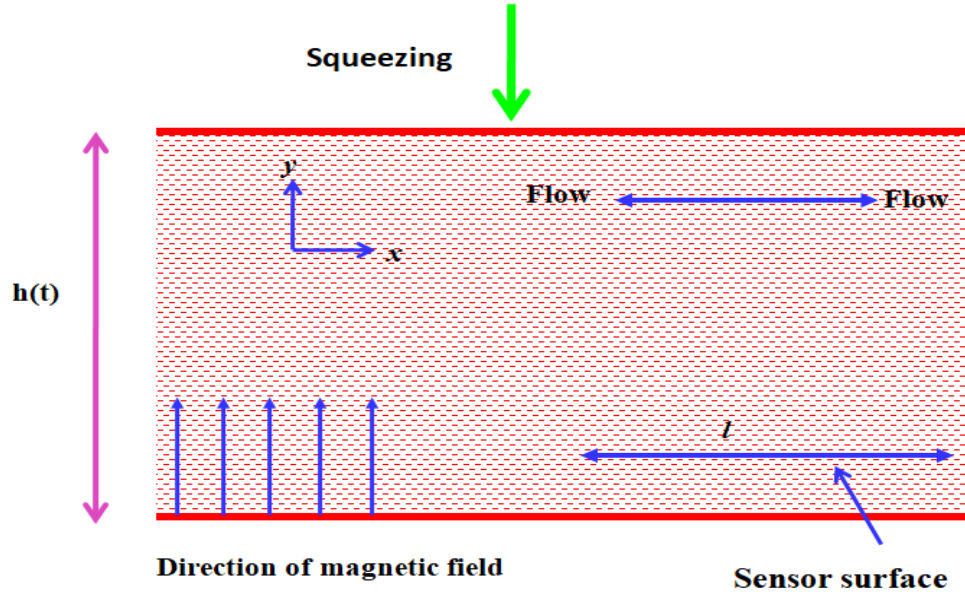


Fig. 3.1: Schematic illustration of the physical problem.

much greater than the boundary layer thickness. The lower plate is immovable whereas the upper plate is squeezed. The fluid is driven by an external free stream velocity  $\tilde{U}_e(x, t)$ . A uniform magnetic field of strength  $B_0$  is implemented perpendicular to the plates, as illustrated in Fig. 3.1.

With the present constraints, the governing equations take the following form [67]

$$\frac{\partial \tilde{u}}{\partial x} + \frac{\partial \tilde{v}}{\partial y} = 0, \quad (3.1)$$

$$\begin{aligned} \frac{\partial \tilde{u}}{\partial t} + \tilde{u} \frac{\partial \tilde{u}}{\partial x} + \tilde{v} \frac{\partial \tilde{u}}{\partial y} = & -\frac{1}{\rho} \frac{\partial \tilde{p}}{\partial x} + \nu \left[ \frac{3(n-1)}{2} \Gamma^2 \left( \frac{\partial \tilde{u}}{\partial y} \right)^2 \frac{\partial^2 \tilde{u}}{\partial y^2} + \frac{\partial^2 \tilde{u}}{\partial y^2} \right] \\ & - \frac{\sigma B_0^2}{\rho} \tilde{u}, \end{aligned} \quad (3.2)$$

$$\frac{\partial \tilde{U}_e}{\partial t} + \tilde{U}_e \frac{\partial \tilde{U}_e}{\partial x} = -\frac{1}{\rho} \left( \frac{\partial \tilde{p}}{\partial x} \right) - \frac{\sigma B_0^2}{\rho} \tilde{U}_e, \quad (3.3)$$

$$\frac{\partial \tilde{T}}{\partial t} + \tilde{u} \frac{\partial \tilde{T}}{\partial x} + \tilde{v} \frac{\partial \tilde{T}}{\partial y} = -\frac{1}{\rho C_p} \frac{\partial q_r}{\partial y} + \frac{\partial}{\partial y} \left( \alpha(\tilde{T}) \frac{\partial \tilde{T}}{\partial y} \right). \quad (3.4)$$

By using Eq. (3.3) in Eq. (3.2) to eliminate the pressure gradient, we have

$$\begin{aligned} \frac{\partial \tilde{u}}{\partial t} + \tilde{u} \frac{\partial \tilde{u}}{\partial x} + \tilde{v} \frac{\partial \tilde{v}}{\partial y} = \frac{\partial \tilde{U}_e}{\partial t} + \nu \frac{\partial^2 \tilde{u}}{\partial y^2} + \nu \frac{3(n-1)}{2} \Gamma^2 \left( \frac{\partial \tilde{u}}{\partial y} \right)^2 \left( \frac{\partial^2 \tilde{u}}{\partial y^2} \right) + \\ \tilde{U}_e \frac{\partial \tilde{U}_e}{\partial x} - \frac{\sigma B_0^2 (\tilde{u} - \tilde{U}_e)}{\rho}. \end{aligned} \quad (3.5)$$

The BCs [66–68] of the above modeled problem are,

$$\left. \begin{aligned} \tilde{u}(x, 0, t) = 0, \quad \tilde{v}(x, 0, t) = \tilde{v}_0(t), \quad -k \frac{\partial \tilde{T}(x, 0, t)}{\partial y} = q(x), \\ \tilde{u}(x, \infty, t) \rightarrow \tilde{U}_e(x, t), \quad \tilde{T}(x, \infty, t) \rightarrow \tilde{T}_\infty. \end{aligned} \right\} \quad (3.6)$$

Here  $q(x)$  represents the wall heat flux. The reference velocity  $\tilde{v}_0$  is considered at the sensor surface when the sensor surface is permeable. At disturbed boundary the reference velocity  $\tilde{v}_0$  is proportional to the normal velocity. The reference velocity  $\tilde{v}_0$  has an increasing behaviour if the pores of the surface are increased or when the distance between the surface and disturbed boundary is small.

In Eq. (3.4),  $q_r$  is the Rosseland radiative heat flux and is given by [59–65]

$$q_r = -\frac{4\sigma^*}{3\kappa^*} \frac{\partial \tilde{T}^4}{\partial y}. \quad (3.7)$$

Expanding  $\tilde{T}^4$  about  $\tilde{T}_\infty$  with the help of Taylor series [92] and ignoring the higher power terms we have

$$\tilde{T}^4 \approx 4\tilde{T}_\infty^3 \tilde{T} - 3\tilde{T}_\infty^4. \quad (3.8)$$

By using the following transformation [66–68], Eqs. (3.4) - (3.5) can be transformed into the ODEs.

$$\left. \begin{aligned} \tilde{U}_e = ax, \quad \psi = x\sqrt{a\nu}f(\eta), \quad \eta = y\sqrt{\frac{a}{\nu}}, \quad a = \frac{1}{s+bt}, \\ \tilde{v} = -f(\eta)\sqrt{a\nu}, \quad \tilde{u} = axf'(\eta), \quad \theta = \frac{\tilde{T} - \tilde{T}_\infty}{\frac{q_0x}{k}\sqrt{\frac{\nu}{a}}}, \end{aligned} \right\} \quad (3.9)$$

where  $q(x) = q_0x$  and  $\tilde{v}_0(t) = \tilde{v}\sqrt{a}$ . Here  $b$  is the index of the squeezed flow and is an arbitrary constant [69]. The parameters  $k$ ,  $a$ ,  $q_0$  and  $s$  represent the



thermal conductivity, the squeezing strength, heat flux and an arbitrary constant respectively. The channel's height follow the following relation:

$$\begin{aligned} h(t) &= \frac{h_0}{(s + bt)^{\frac{1}{b}}} && \text{for } b > 0, \\ h(t) &= h_0 e^{-st} && \text{for } b = 0, \end{aligned}$$

here  $h_0$  is the constant. As time reduces, the permeable velocity increases (when  $b > 0$ ).

The temperature dependent thermal conductivity  $\alpha$  is given by

$$\alpha(\theta) = k_\infty (1 + \epsilon\theta),$$

where  $\epsilon$  is a small parameter.

The Eq. (3.1) is satisfied identically and Eq. (3.5) yields

$$\begin{aligned} f''' \left( 1 + \frac{3(n-1)}{2} We^2 f'^2 \right) + \left( f + \frac{\eta}{2} b \right) f'' + b(f' - 1) - (f')^2 \\ + M^2 (1 - f') - 1 = 0, \end{aligned} \quad (3.10)$$

and temperature equation (3.4) becomes

$$\left( 1 + \epsilon\theta + \frac{4}{3} Rd \right) \theta'' + Pr \left[ \left( f + \frac{\eta}{2} b \right) \theta' - \left( f' + \frac{b}{2} \right) \theta \right] + \epsilon (\theta')^2 = 0. \quad (3.11)$$

The associated BCs of the above problem are

$$\left. \begin{aligned} f(\eta) &= -f_0, \quad f'(\eta) = 0, \quad \theta'(\eta) = -1, \quad \text{at } \eta = 0, \\ f' &\rightarrow 1, \quad \theta \rightarrow 0, \quad \text{as } \eta \rightarrow \infty. \end{aligned} \right\} \quad (3.12)$$

In above equations,  $M$ ,  $Rd$ ,  $f_0$ ,  $We$  and  $Pr$  represent the magnetic number, the thermal radiation parameter, the permeable velocity, the Weissenberg number and the Prandtl number respectively. These parameters are formulated as:

$$M^2 = \frac{\sigma B_0^2}{a\rho}, \quad Rd = \frac{4\sigma^* \tilde{T}_\infty^3}{k_\infty \kappa^*}, \quad f_0 = \sqrt{v}, \quad We^2 = \frac{a^3 x^2 \Gamma^2}{v}, \quad Pr = \frac{\nu}{\alpha}.$$

## 3.2 Quantities of Interest

### 3.2.1 The Surface Drag and Nusselt Number

The surface drag and the Nusselt number are given by

$$C_f = \frac{\tau_w}{ax\sqrt{\frac{a}{\nu}}},$$

$$Nu = \frac{xq_w}{k_\infty(\tilde{T} - \tilde{T}_\infty)}.$$

In dimensional form of the wall shear stress [67] and the wall heat flux [62] are given by

$$\tau_w = \left[ \frac{\partial \tilde{u}}{\partial y} + \Gamma^2 \frac{(n-1)}{2} \left( \frac{\partial \tilde{u}}{\partial y} \right)^3 \right]_{y=0},$$

$$q_w = -k_\infty \left[ \left( 1 + \frac{16\sigma^* \tilde{T}_\infty^3}{3k_\infty \kappa^*} \right) \frac{\partial \tilde{T}}{\partial y} \right]_{y=0}.$$

In the dimensionless form, the surface drag and Nusselt number are given by

$$\sqrt{Re_x} C_f = \left[ \left( 1 + \frac{(n-1)}{2} We^2 f''^2(\eta) \right) f''(\eta) \right]_{\eta=0},$$

$$Nu Re_x^{-1/2} = \left[ \frac{1}{\theta(\eta)} \left( 1 + \frac{4}{3} Rd \right) \right]_{\eta=0},$$

where  $Re_x = x\sqrt{\frac{a}{\nu}}$ .

## 3.3 Implementation of the Numerical Scheme

The shooting technique [92] is implemented to solve the formulated ODEs (3.10)-(3.11), along with the BCs (3.12). To apply the shooting technique we need a system of first order ODEs. For this, new variables,  $f = \zeta_1$ ,  $f' = \zeta_2$ ,  $f'' = \zeta_3$ ,  $\theta = \zeta_4$  and  $\theta' = \zeta_5$  have been introduced.

$$\left. \begin{aligned}
\zeta'_1 &= \zeta_2, \\
\zeta'_2 &= \zeta_3, \\
\zeta'_3 &= \frac{2}{2 + 3(n-1)We^2\zeta_3^2} \left[ \zeta_2^2 - \left(\zeta_1 + \frac{\eta}{2}b\right)\zeta_3 - b(\zeta_2 - 1) \right. \\
&\quad \left. + M^2(\zeta_2 - 1) - 1 \right], \\
\zeta'_4 &= \zeta_5, \\
\zeta'_5 &= \frac{3}{3 + 3\epsilon\zeta_4 + 4Rd} \left[ Pr \left(\zeta_2 + \frac{b}{2}\right)\zeta_4 - Pr \left(\zeta_1 + \frac{\eta}{2}b\right)\zeta_5 - \epsilon\zeta_5^2 \right],
\end{aligned} \right\} \quad (3.13)$$

subject to BCs

$$\left. \begin{aligned}
\zeta_1(\eta) = -f_0, \quad \zeta_2(\eta) = 0, \quad \zeta_5(\eta) = -1, \quad \text{at } \eta = 0, \\
\zeta_2(\eta) \rightarrow 1, \quad \zeta_4(\eta) \rightarrow 0, \quad \text{as } \eta \rightarrow \infty.
\end{aligned} \right\} \quad (3.14)$$

In order to find the solution the system of Eqs. (3.13) with the assistance of the shooting technique, five initial conditions are required. Therefore, we guess the two unknown initial conditions as  $\zeta_3(0) = s_1$  and  $\zeta_4(0) = s_2$  in such a way that two known BCs are approximately satisfied for  $\eta \rightarrow \infty$ . The Newton's method is applied to update  $s_1$  and  $s_2$  until the desired approximation is met. The process will continued till the following criteria is met.

$$\max\{|\zeta_2(\eta_{max}) - 1|, |\zeta_4(\eta_{max}) - 0|\} < 10^{-6},$$

The computations have been performed for various prominent parameters over the bounded domain  $[0, \eta_{max}]$  instead of  $[0, \infty)$ . For  $\eta > \eta_{max}$ , there are no significant changes in the results.

### 3.3.1 Validation of Code

For the reliability and validation of the code, we reproduce the values of the skin friction  $C_f Re_x^{1/2}$ , reported by Mair *et al.* [67]. The method used by Mair *et al.* was the shooting method. The present computations have good concord with the results in the above published articles.

$We$	$n$	[67]	Present Study
0.1	1.2	0.7234	0.7234
0.5	1.2	0.7320	0.7384
0.9	1.2	0.7394	0.7394
0.1	1.5	0.7238	0.7238
0.1	1.8	0.7241	0.7241
0.1	2.1	0.7244	0.7244

Table 3.1: Comparison of  $C_f Re_x^{1/2}$  values against different values  $We$  and  $n$ .

## 3.4 Results and Discussion

### 3.4.1 The Skin Friction Coefficient and Nusselt Number

Table 3.2 is displayed to portray the influence of emerging parameters on the surface drag and the Nusselt number. From this table it is noticed that the surface drag is declined for boosting values of squeezed flow index  $b$  while reverse trend is noticed for the Nusselt number. It is due to the fact that the squeezed flow index  $b$  and strength of squeezed flow parameter  $a$  have inverse relation. Therefore, by increasing the squeezed flow index, the skin friction is declined whereas the Nusselt number is increased. The same trend in Nusselt number is observed for the magnetic number  $M$ . Generally, an enhancement in the magnetic number  $M$  results an increment in the opposing force (Lorentz forces) which causes the slowness of the fluid and an increase in the heat transfer rate. An increasing behavior is noticed in the Nusselt number as each of the Prandtl number  $Pr$ , the thermal conductivity parameter  $\epsilon$  and the thermal radiation parameter  $Rd$  are heightened whereas the Weissenberg number  $We$  causes a decrement. Increasing the value of  $We$  means enhancing of the relaxing time therefore the Nusselt number is reduced whereas the surface drag coefficient is hiked. By increasing the power-law index  $n$ , the skin friction is upsurged while diminution is noticed in the Nusselt

number. An acclivity in the permeable velocity  $f_0$  means the suction takes place and more fluid is attached to the surface, therefore both the surface drag and the Nusselt number are reduced.

$b$	$\epsilon$	$We$	$Rd$	$Pr$	$M$	$f_0$	$n$	$C_f Re_x^{1/2}$	$Nu Re_x^{-1/2}$
0.1	0.1	0.1	1	1	1	1	1.2	1.091617	0.913560
								1.065764	0.955400
								1.039088	0.996675
	0.0							1.091617	0.950211
	0.1							1.091617	0.913560
	0.2							1.091617	0.879921
		0.2						1.093271	0.913246
		0.3						1.096001	0.912731
		0.4						1.099977	0.912023
			2.0					1.091617	1.399950
			3.0					1.091617	1.869384
			4.0					1.091617	2.330340
				1.2				1.091617	0.925584
				1.3				1.091617	0.929862
				1.4				1.091617	0.933146
					0.8			0.970622	0.890026
					1.0			1.091617	0.913560
					1.2			1.227376	0.937484
						1.2		1.016367	0.827023
						1.3		0.981051	0.786283
						1.4		0.947236	0.747229
							2.0	1.093819	0.913144
							3.0	1.096543	0.912629
							4.0	1.099236	0.912123

Table 3.2: Variation in the  $C_f Re_x^{1/2}$  and  $Nu Re_x^{-1/2}$  for different physical parameters.

In the subsequent subsections, the graphical results of this investigation have been presented in terms of flow distributions for the different prominent parameters.

For all the graphical presentations of axial velocity and temperature, we have considered,  $Pr = M = Rd = 1, \epsilon = We = b = 0.1, n = 1.2$ , and  $f_0 = -0.1$ .

### 3.4.2 Effect of Squeezed Flow Parameter $b$

To expose the behaviour of squeezed flow parameter  $b$  on flow fields Figs. 3.2(a)-(b) are delineated. The velocity distribution is diminished for  $0 \leq \eta \leq 1.15$  and increases for  $1.15 \leq \eta \leq 3$  approximately which is evident from the Fig. 3.2(a). By increasing the squeezing phenomena the kinetic energy of the fluid particles enhances. But there is an inverse relation between strength of squeeze flow and squeezed flow index  $b$  due to which the velocity is declined. To study the variations in the thermal profile due to the squeezed flow parameter  $b$ , Fig. 3.2(b) is chalked out. The temperature profile is declined as the squeezed flow parameter  $b$  is increased.

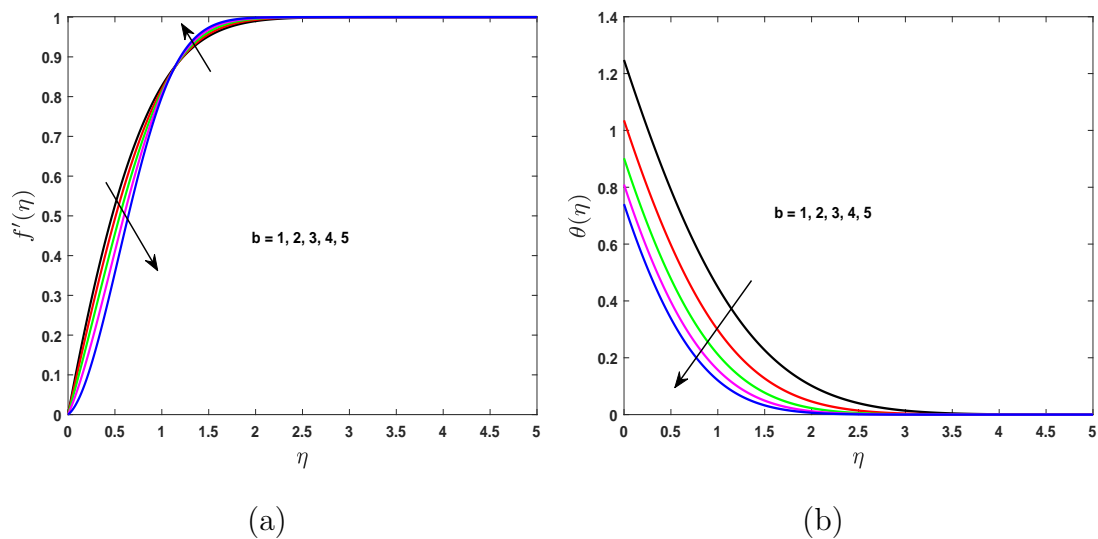


**Fig. 3.2:** Impact of  $b$  on (a) velocity and (b) temperature profile.

### 3.4.3 Effect of Magnetic Number $M$

Figs. 3.3(a)-(b) are displayed to analyze the impact of  $M$  on fluid motion and temperature field. Fig. 3.3(a) shows that with the small enhancement in  $M$  causes an increment in the velocity. Physically, by enhancing the value of  $M$ , more

opposing force is offered to the fluid motion but due to dominating squeezing phenomenon, the effect of the magnetic number  $M$  is reduced due to which  $f'(\eta)$  is augmented. Fig. 3.3(b) is displayed to investigate the magnetic effect on  $\theta(\eta)$ . There is a small decrement in the thermal distribution as the magnetic number  $M$  is increased.

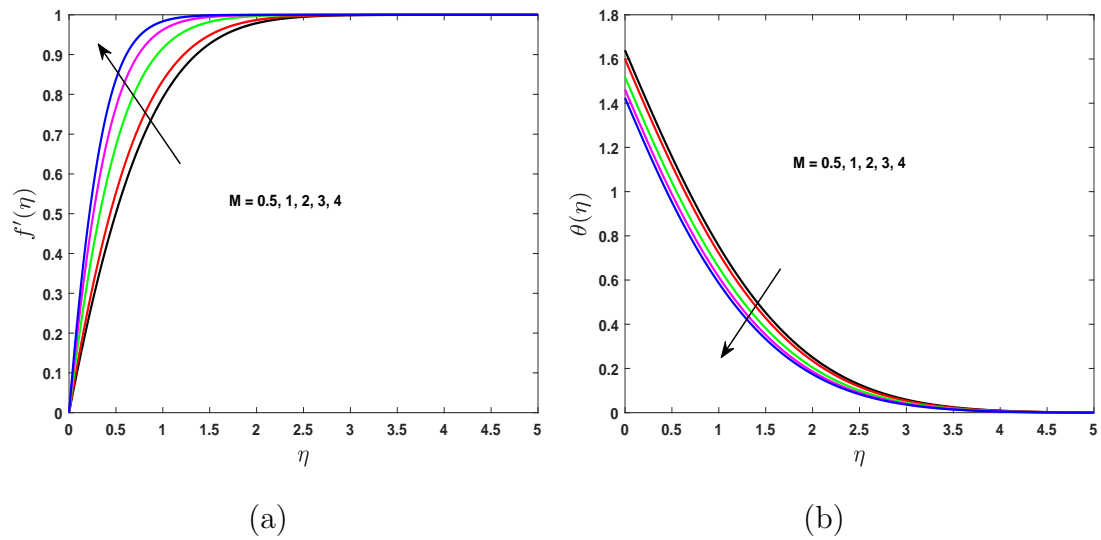
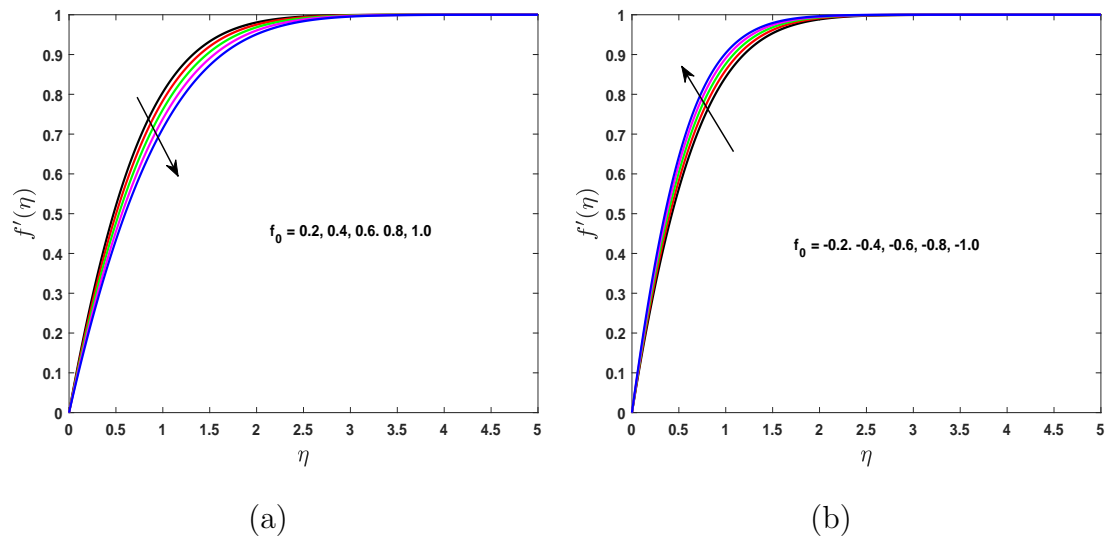
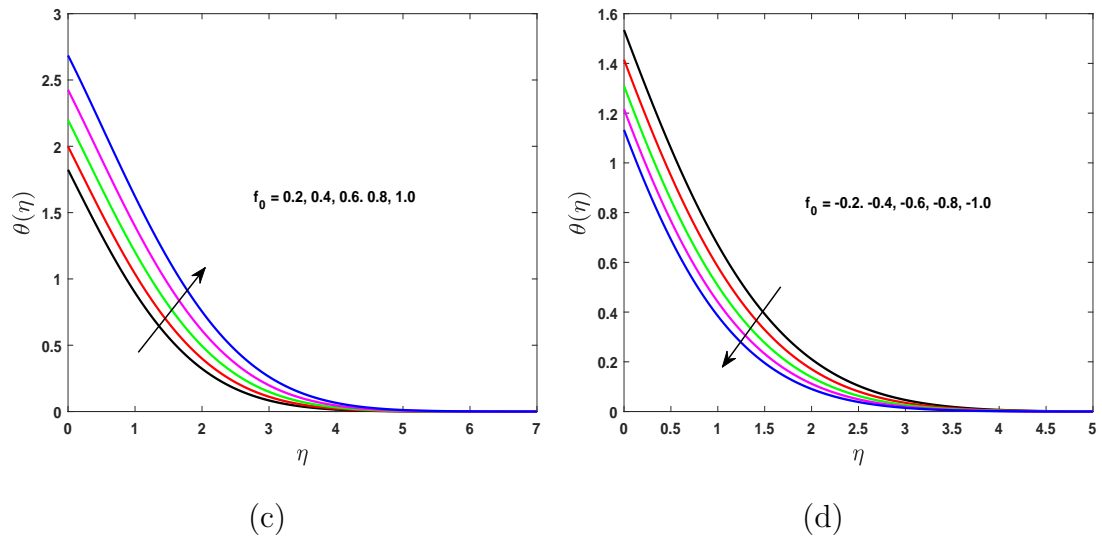


Fig. 3.3: Impact of  $M$  on (a) velocity and (b) temperature profile.

### 3.4.4 Effect of Suction/Injection Parameter $f_0$

Figs. 3.4(a)-(b) are delineated to analyzed the impact of permeable velocity parameter  $f_0$  on velocity distribution. It is perceived that the fluid motion is decreased





**Fig. 3.4:** Impact of  $f_0$  on velocity and temperature profile.

for suction i.e.  $f_0 > 0$  and increased for injection i.e.  $f_0 < 0$ . Physically, when suction takes place more fluid is attached to the sensor surface and hence the velocity decreases. While moving away from the sensor surface opposite effect is observed. Figs. 3.4(c)-(d) are presented to analyze the impact of  $f_0$  on energy field, which shows that the energy profile is hiked for suction i.e.  $f_0 > 0$  and diminished for injection i.e.  $f_0 < 0$ .

### 3.4.5 Effect of Power-Law Index $n$

To visualize the variation in the flow fields caused by the changes in power-law index  $n$ , Figs. 3.5(a)-(b) are drawn. From Fig. 3.5(a) it is clear that the fluid motion slows down whereas the related boundary layer thickness is enhanced which reflects that the power-law index prevents the fluid motion. Fig. 3.5(b) represents that for the acclivity in the value of  $n$  results an enhancement in the thermal profile. Increasing the value of the power-law index  $n$  means there is an increase in the viscosity of the fluid. The increment in the viscosity of the fluid causes the slowness of the fluid due to which both temperature profile and thermal boundary layer thickness is hiked.



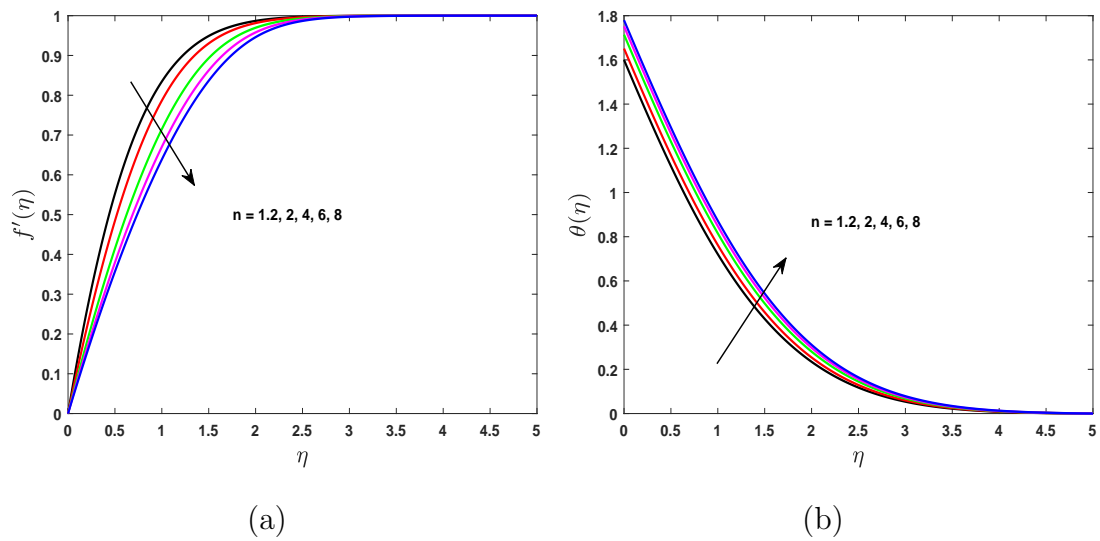


Fig. 3.5: Impact of  $n$  on (a) velocity and (b) temperature profile.

### 3.4.6 Effect of Weissenberg Number $We$

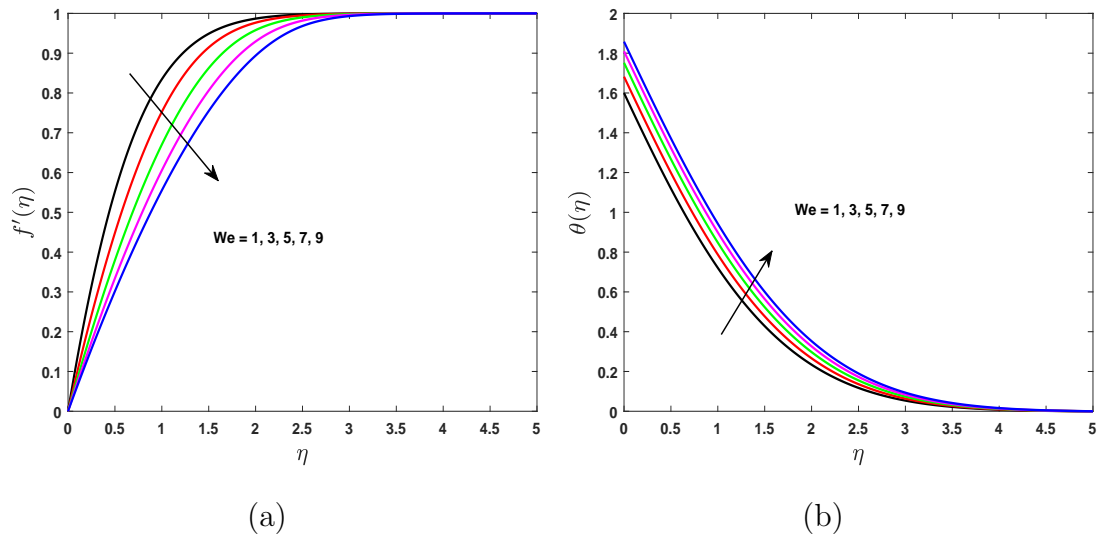
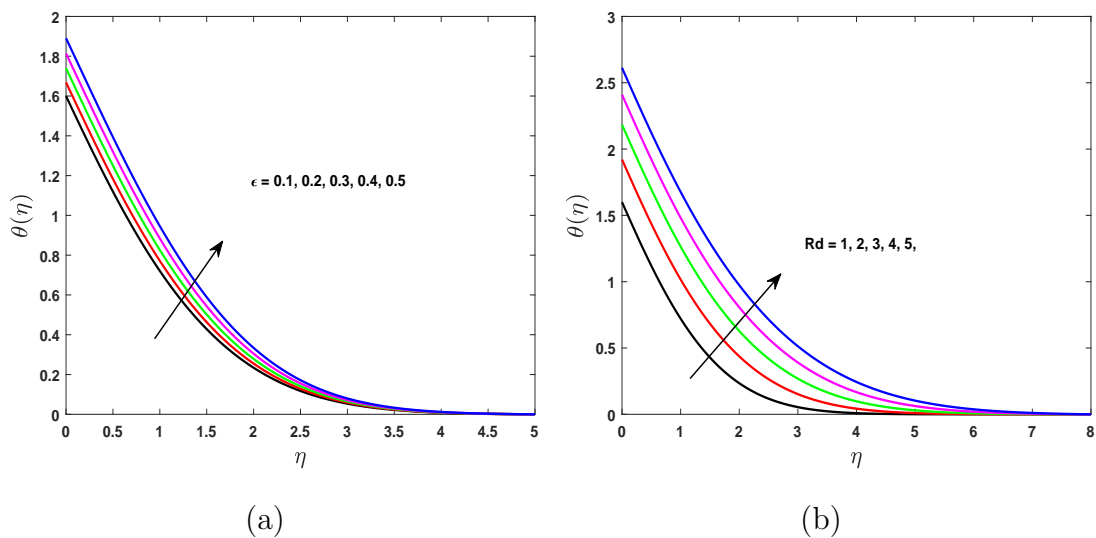


Fig. 3.6: Impact of  $We$  on (a) velocity and (b) temperature profile.

The Fig. 3.6(a) represents the changes in the velocity profile due to the Weissenberg number  $We$ . The curves of this graph shows that  $f'(\eta)$  reduces as the  $We$  is gradually mounted. Larger value of the  $We$  means an increment in relaxation time and hence the velocity is decreased. Fig. 3.6(b) indicates that the temperature profile is augmented for the intensifying values of the  $We$ .

### 3.4.7 Effect of Thermal Conductivity Parameter $\epsilon$ and Thermal Radiation Parameter $Rd$

An augmentation is observed in the energy profile due to increment in the thermal conductivity parameter  $\epsilon$  as presented in Fig. 3.7(a). The dimensionless thermal field is increased as the radiation parameter  $Rd$  is escalated as shown in Fig. 3.7(b). Physically, it strengthens the fact that more heat is generated due to the radiation process for which the radiation parameter is increased.



**Fig. 3.7:** Impact of (a)  $\epsilon$  and (b)  $Rd$  on temperature profile.

## 3.5 Conclusions

In this chapter, the squeezed Carreau fluid flow with magnetic effect past a sensor surface has been analyzed. The thermal conductivity is assumed to be variable and thermal radiation effect has also been incorporated in the energy equation.

In the absence of the magnetic field the skin friction coefficient is same as of [67], however the rate of heat transfer is higher as the Prandtl number and thermal conductivity parameter is enhanced. Some of the key findings are:

- The velocity profile is declined for increment in the Weissenberg number  $We$  and the power-law index  $n$  while reverse behavior is observed for magnetic number  $M$ .
- The energy profile is reduced as the squeezed flow parameter  $b$  is heightened while the Weissenberg number  $We$  and the power-law index  $n$  has opposite effect.
- The velocity profile is diminished and the energy profile is enhanced for suction ( $f_0 > 0$ ) whereas reverse trend is observed for injection ( $f_0 < 0$ ).
- The Nusselt number is declined for an enhancement in each of the thermal conductivity parameter  $\epsilon$ , the Weissenberg number  $We$  and permeable velocity  $f_0$ .
- The skin friction is declined as each of the permeable velocity  $f_0$  and the squeezed flow parameter  $b$  is increased.

## Chapter 4

# MHD Tangent Hyperbolic Nanofluid Flow with Slip and Convective Conditions

The forthright objective of this study is to scrutinize the magnetohydrodynamic tangent hyperbolic fluid in the presence of nanoparticles past a stretching sheet. Regarding the nanofluid, the Buongiorno model has been used to study the flow field and heat transfer. For the simulations of heat and mass transport phenomena slip and convective boundary conditions have been considered. Variable thermal conductivity, Joule heating, linear thermal radiation and viscous dissipation effects have also been incorporated in the energy equation. No nanoparticles flux condition has also been employed, which indicates that the nanoparticles fraction are passively controlled. This condition makes the model more practical for certain engineering applications [6, 74, 93]. The governing set of PDEs are rendered into nonlinear ODEs by means of similarity transformation. Shooting method is utilized to obtain the solution of the resulting ODEs. Furthermore, an authentication of the computed results is obtained through benchmark with the published results in the literature. Effect of prominent parameters on different flow fields has been analyzed graphically and discussed in detail.

### 4.0.1 Problem Formulation

An incompressible, 2D magnetohydrodynamic tangent hyperbolic fluid with nanoparticles past a stretching surface has been considered for analysis. The stretching sheet is positioned along  $x$  – axis having stretching velocity  $\tilde{u} = ax$  and  $y$  – axis is normal to the stretching sheet. The flow is confined in  $y > 0$  region. Convective heating mode has also been considered and heat transfer coefficient is represented by  $h_f$ . In a direction perpendicular to the stretching surface a magnetic field  $B_0$  is implemented towards positive  $y$  – axis as displayed in Fig. 4.1. Additionally, Joule heating, no nanoparticles flux condition and viscous dissipation effects have also been considered. Being within the above constraints, the basic equations for the above modeled problem are as follows:

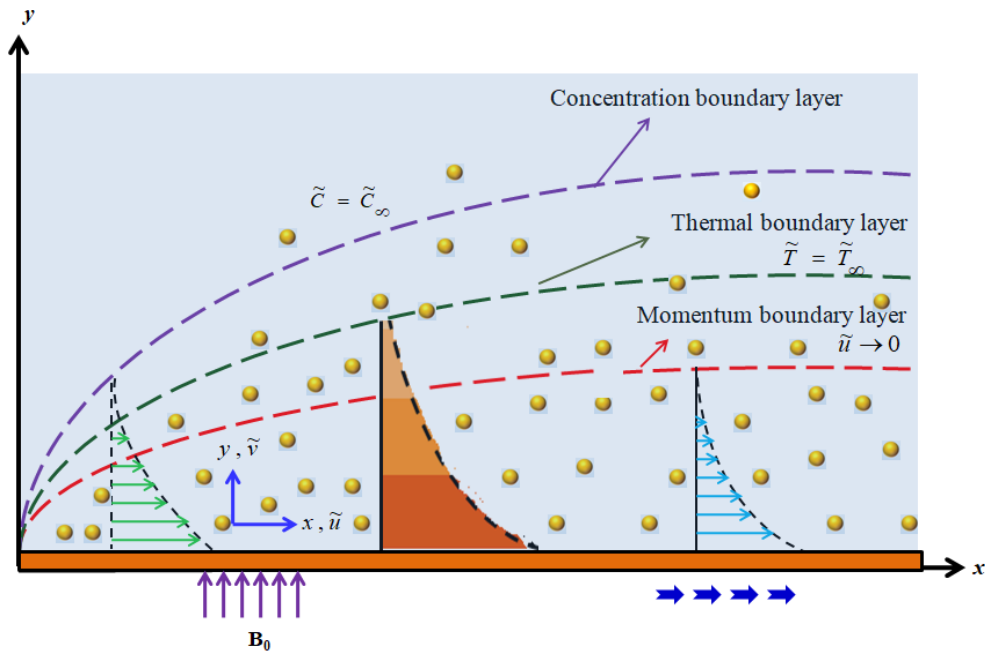


Fig. 4.1: Flow configuration.

$$\frac{\partial \tilde{u}}{\partial x} + \frac{\partial \tilde{v}}{\partial y} = 0, \quad (4.1)$$

$$\tilde{u} \frac{\partial \tilde{u}}{\partial x} + \tilde{v} \frac{\partial \tilde{u}}{\partial y} = \nu \left[ (1-n) + \sqrt{2n}\Gamma \left( \frac{\partial \tilde{u}}{\partial y} \right) \right] \frac{\partial^2 \tilde{u}}{\partial y^2} - \frac{\sigma B_0^2}{\rho} \tilde{u}, \quad (4.2)$$

$$\begin{aligned} \tilde{u} \frac{\partial \tilde{T}}{\partial x} + \tilde{v} \frac{\partial \tilde{T}}{\partial y} = \frac{\partial}{\partial y} \left( \alpha(\tilde{T}) \frac{\partial \tilde{T}}{\partial y} \right) + \frac{\nu}{C_p} (1-n) \left( \frac{\partial \tilde{u}}{\partial y} \right)^2 + \frac{\nu n \Gamma}{\sqrt{2} C_p} \frac{\partial \tilde{u}}{\partial y} \left( \frac{\partial \tilde{u}}{\partial y} \right)^2 \\ - \frac{1}{\rho C_p} \frac{\partial q_r}{\partial y} + \frac{\sigma B_0^2}{\rho C_p} \tilde{u}^2 + \frac{(\rho C_p)_p}{(\rho C_p)_f} \left[ D_B \frac{\partial \tilde{C}}{\partial y} \frac{\partial \tilde{T}}{\partial y} + \frac{D_T}{\tilde{T}_\infty} \left( \frac{\partial \tilde{T}}{\partial y} \right)^2 \right], \end{aligned} \quad (4.3)$$

$$\tilde{u} \frac{\partial \tilde{C}}{\partial x} + \tilde{v} \frac{\partial \tilde{C}}{\partial y} = D_B \frac{\partial^2 \tilde{C}}{\partial y^2} + \frac{D_T}{\tilde{T}_\infty} \frac{\partial^2 \tilde{T}}{\partial y^2}. \quad (4.4)$$

The above formulated problem has BCs as follows:

$$\left. \begin{aligned} \tilde{u} = ax + L \frac{\partial \tilde{u}}{\partial y}, \quad \tilde{v} = 0, \quad -k \frac{\partial \tilde{T}}{\partial y} = h_f (\tilde{T}_f - \tilde{T}), \\ D_B \frac{\partial \tilde{C}}{\partial y} + \frac{D_T}{\tilde{T}_\infty} \left( \frac{\partial \tilde{T}}{\partial y} \right) = 0, \\ \tilde{u} \rightarrow \tilde{U}_\infty = 0, \quad \tilde{v} \rightarrow 0, \quad \tilde{T} \rightarrow \tilde{T}_\infty, \quad \tilde{C} \rightarrow \tilde{C}_\infty \quad \text{as } y \rightarrow \infty. \end{aligned} \right\} \text{ at } y = 0, \quad (4.5)$$

Here,  $\sigma$  represents the electrical conductivity,  $n$  the power-law index,  $\rho_f, \rho_p, (C_p)_p$  and  $(C_p)_f$  represents the density of nanofluid, nanoparticles, the specific heat of the nanoparticles and fluid respectively. Thermal diffusion and the Brownian diffusion parameters are denoted by  $D_T$  and  $D_B$  respectively.

In (4.3),  $q_r$  is the Rosseland radiative heat flux as defined in (3.7) of chapter 3 and the temperature dependent thermal conductivity  $\alpha(\tilde{T})$  is given by the expression

$$\alpha(\tilde{T}) = k_\infty \left( 1 + \epsilon \frac{\tilde{T} - \tilde{T}_\infty}{\Delta \tilde{T}} \right).$$

To make the modeled equations dimensionless, the following transformations [6] have been introduced.

$$\eta = y \sqrt{\frac{a}{\nu}}, \quad \psi = x \sqrt{a\nu} f(\eta), \quad \theta(\eta) = \frac{\tilde{T} - \tilde{T}_\infty}{\tilde{T}_f - \tilde{T}_\infty}, \quad \phi(\eta) = \frac{\tilde{C} - \tilde{C}_\infty}{\tilde{C}_\infty}. \quad (4.6)$$

As a result, (4.1) is satisfied identically and equations (4.2)-(4.4) yield the following ODEs:

$$(1 - n + nWe f'') f''' + f f'' - f'^2 - M f' = 0, \quad (4.7)$$

$$\begin{aligned} \left(1 + \epsilon\theta + \frac{4}{3}Rd\right)\theta'' + Prf\theta' + \epsilon\theta'^2 + (1-n)PrEc f''^2 + \frac{nPrEcWe}{2}f''^3 \\ + MPrEc f'^2 + PrNb\theta'\phi' + PrNt\theta'^2 = 0, \end{aligned} \quad (4.8)$$

$$\phi'' + PrLe f\phi' + \frac{Nt}{Nb}\theta'' = 0. \quad (4.9)$$

In dimensionless form the BCs are

$$\left. \begin{aligned} f(\eta) = 0, \quad f'(\eta) = 1 + \delta f'', \\ \theta'(\eta) = Bi(\theta(\eta) - 1), \quad Nb\phi'(\eta) + Nt\theta'(\eta) = 0, \\ f'(\eta) \rightarrow 0, \quad \theta(\eta) \rightarrow 0, \quad \phi(\eta) \rightarrow 0, \quad \text{as } \eta \rightarrow \infty. \end{aligned} \right\} \text{ at } \eta = 0, \quad (4.10)$$

In the above equations,  $Pr$  denotes the Prandtl number,  $We$  the Weissenberg number,  $M$  the magnetic number,  $Nb$  the Brownian motion parameter,  $Le$  the Lewis number,  $Bi$  the Biot number,  $Ec$  the Eckert number,  $Nt$  the thermophoresis parameter,  $Re_x$  the local Reynolds number,  $Rd$  the thermal radiation parameter and  $\delta$  the velocity slip parameter.

These parameters are formulated as:

$$\begin{aligned} Pr = \frac{\nu}{\alpha}, \quad We = \frac{\sqrt{2}a^{\frac{3}{2}}x\Gamma}{\sqrt{\nu}}, \quad M = \frac{\sigma B_0^2}{a\rho}, \quad Nb = \frac{(\rho C_p)_p D_B \tilde{C}_\infty}{(\rho C_p)_f \nu}, \quad Le = \frac{\alpha}{D_B}, \quad Bi = \\ \frac{h_f}{k} \sqrt{\frac{\nu}{a}}, \quad Ec = \frac{a^2 x^2}{(C_p)_f (\tilde{T}_f - \tilde{T}_\infty)}, \quad Nt = \frac{(\rho C_p)_p D_T (\tilde{T}_f - \tilde{T}_\infty)}{(\rho C_p)_f \nu \tilde{T}_\infty}, \quad Re_x = \frac{ax^2}{\nu}, \quad Rd = \frac{4\sigma^* \tilde{T}_\infty^3}{k_\infty \kappa^*}, \\ \delta = A \sqrt{\frac{a}{\nu}}, \end{aligned}$$

where  $A$  is a constant.

## 4.1 Quantities of Interest

In industrial and engineering perspective, the quantities of foremost interest are the skin friction coefficient and Nusselt number.

In the present section both skin friction coefficient and the Nusselt number have been formulated in both the dimensional and the non dimensional form as follows:

### 4.1.1 The Skin Friction Coefficient

The surface drag or the skin friction is an imperative feature of the boundary layer and is given by

$$C_f = \frac{\tau_w}{\rho_f \tilde{u}_w^2}.$$

For the present study the shear stress at wall  $\tau_w$  is given by

$$\tau_w = \mu \left[ (1-n) \frac{\partial \tilde{u}}{\partial y} + \frac{n\Gamma}{\sqrt{2}} \left( \frac{\partial \tilde{u}}{\partial y} \right)^2 \right]_{y=0}.$$

In the dimensionless form

$$C_f \sqrt{Re_x} = (1-n) f''(0) + \frac{n}{2} We f''^2(0). \quad (4.11)$$

### 4.1.2 The Nusselt Number

The Nusselt number is given by

$$Nu = \frac{xq_w}{k_\infty(\tilde{T}_f - \tilde{T}_\infty)}.$$

For the current modeled problem the heat flux  $q_w$  at the surface is given by

$$q_w = -k_\infty \left[ \left( 1 + \frac{16\sigma^* \tilde{T}_\infty}{3k_\infty \kappa^*} \right) \frac{\partial \tilde{T}}{\partial y} \right]_{y=0}.$$

In the dimensionless form the Nusselt number for the modeled problem is given by

$$Nu_x Re_x^{-1/2} = - \left( 1 + \frac{4}{3} Rd \right) \theta'(0), \quad (4.12)$$

where  $Re_x = \frac{ax^2}{\nu}$ .



## 4.2 Implementation of the Numerical Scheme

The shooting technique [92] is utilized to solve the ODEs (4.7)-(4.9), subject to the BCs (4.10). To convert (4.7)-(4.9) into a system of first order ODEs, we introduce new variables,  $\zeta_1 = f$ ,  $\zeta_2 = f'$ ,  $\zeta_3 = f''$ ,  $\zeta_4 = \theta$ ,  $\zeta_5 = \theta'$ ,  $\zeta_6 = \phi$  and  $\zeta_7 = \phi'$ . Equations (4.7)-(4.9) have been converted into the system of seven first order ODEs:

$$\left. \begin{aligned} \zeta_1' &= \zeta_2, \\ \zeta_2' &= \zeta_3, \\ \zeta_3' &= \frac{1}{1-n+nWe\zeta_3} \left[ \zeta_2^2 - \zeta_1\zeta_3 + M\zeta_2 \right], \\ \zeta_4' &= \zeta_5, \\ \zeta_5' &= -\frac{3}{3+3\epsilon\zeta_4+4Rd} \left[ Pr\zeta_1\zeta_5 + \epsilon\zeta_5^2 + (1-n)PrEc\zeta_3^2 \right. \\ &\quad \left. + \frac{n}{2}PrEcWe\zeta_3^3 + PrMEc\zeta_2^2 + PrNb\zeta_5\zeta_7 + PrNt\zeta_5^2 \right], \\ \zeta_6' &= \zeta_7, \\ \zeta_7' &= -PrLe\zeta_1\zeta_7 - \left( \frac{Nt}{Nb} \right) y_5'. \end{aligned} \right\} \quad (4.13)$$

The associated BCs takes the form as follows:

$$\left. \begin{aligned} \zeta_1(\eta) &= 0, & \zeta_2(\eta) &= 1 + \delta\zeta_3(\eta), \\ \zeta_5(\eta) &= Bi(\zeta_4(\eta) - 1), & \zeta_7(\eta) &= -\frac{Nt}{Nb}\zeta_5(\eta), \\ \zeta_2 &\rightarrow 0, & \zeta_4 &\rightarrow 0, & \zeta_6 &\rightarrow 0, \text{ as } \eta \rightarrow \infty. \end{aligned} \right\} \text{ at } \eta = 0, \quad (4.14)$$

For the solution of the above formulated problem (4.13) with the help of shooting method, we have to choose some suitable guesses  $\zeta_3(0) = s_1$ ,  $\zeta_4(0) = s_2$ , and  $\zeta_6(0) = s_3$ . Newton's iterative scheme is applied to improve the accuracy of these initial guesses  $s_1$ ,  $s_2$  and  $s_3$  until the following desired approximation is achieved.

$$\max\{|\zeta_2(\eta_{max}) - 0|, |\zeta_4(\eta_{max}) - 0|, |\zeta_6(\eta_{max}) - 0|\} < 10^{-6}.$$

### 4.2.1 Validation of Code

For the reliability and validation of the code, we reproduce the numerical results of the skin friction reported by Ibrahim [6] and Fathizadeh *et al.* [31]. Our computations have an excellent agreement with the results already published in the literature and can be seen in Table 4.1.

$M$	[6]	[31]	Present Result
0	1.0000	1.0000	1.00001
0.25	1.1180	—	1.11803
1	1.4142	1.41421	1.41421
5	2.4495	2.44948	2.44949
10	3.3166	3.31662	3.31662
50	7.1414	7.14142	7.14142
100	10.0499	10.0499	10.0499
500	22.3830	22.3830	22.3830

Table 4.1: Comparison of the presently computed values of  $C_f Re_x^{1/2}$ .

## 4.3 Results and Discussion

### 4.3.1 The skin friction coefficient

Table 4.2 is displayed to analyze the effect of the prominent parameters like magnetic number  $M$ , Weissenberg number  $We$ , power-law index  $n$  and slip parameter  $\delta$  on  $C_f Re_x^{1/2}$ . It is noticed that intensifying the magnetic number  $M$  causes an increment in the skin friction coefficient whereas an enhancement in the Weissenberg number  $We$ , the power-law index  $n$  and the slip parameter  $\delta$  reduces the skin friction.

$We$	$n$	$M$	$\delta$	$-C_f Re_x^{1/2}$
0.1	0.1	0.2	1	0.425166
0.2				0.424368
0.3				0.423567
0.1	0.2			0.386956
	0.3			0.347262
	0.4			0.305835
	0.1	0.3		0.437683
		0.4		0.449105
		0.5		0.459587
		0.2	2	0.277203
			3	0.207546
			4	0.166523

Table 4.2: Variation in the  $C_f Re_x^{1/2}$  due to different values  $M, We, n$  and  $\delta$  when  $Bi = Pr = 2, Ec = 0.2, Le = 5, Nb = Nt = 0.5, Rd = 0.8, \epsilon = 0.1$ .

### 4.3.2 The Nusselt Number

$Nt$	$n$	$We$	$Bi$	$Rd$	$\epsilon$	$Nu_x Re_x^{-1/2}$
0.1	0.2	0.1	2	1	0.1	0.600319
0.2						0.596317
0.3						0.582176
0.1	0.3					0.590424
	0.4					0.566985
	0.5					0.539507
	0.2	0.2				0.609856
		0.3				0.609055
		0.4				0.608247
		0.1	3			0.638866
			4			0.653922
			5			0.663282
			2	2		0.771764
				3		0.926169
				4		1.079978
				1	0.2	0.596530
					0.3	0.583098
					0.4	0.570309

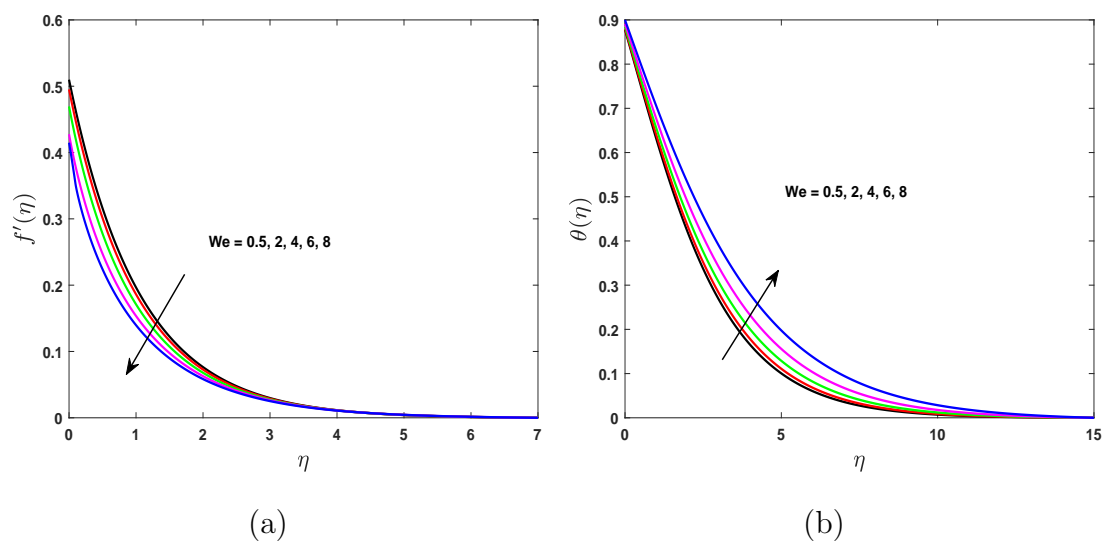
Table 4.3: Variation in the  $Nu_x Re_x^{-1/2}$  due to different values of  $Nt, We, Bi, Rd, n$ , and  $\epsilon$  when  $M = Ec = 0.2, Le = 5, Pr = 2, Nb = 0.5, \delta = 1$ .

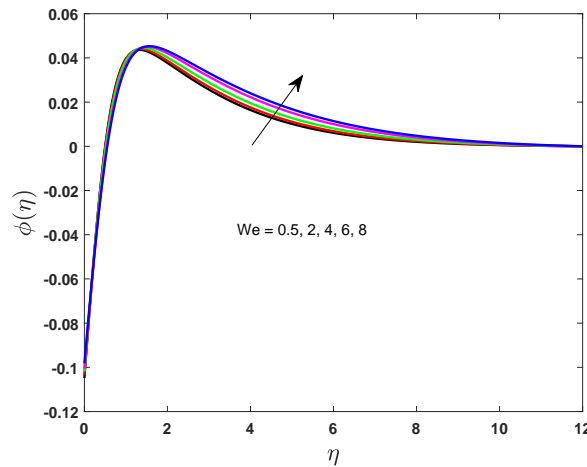
Table 4.3 is presented to analyze the impact of assorted dimensionless parameters on  $Nu_x Re_x^{-\frac{1}{2}}$ . It is observed that an acclivity in each of the thermal conductivity parameter  $\epsilon$ , the thermophoresis parameter  $Nt$ , the power-law index  $n$  and the Weissenberg number  $We$ , the Nusselt number is declined whereas reverse trend is observed for the thermal radiation parameter  $Rd$  and the Biot number  $Bi$ .

To execute the numerical simulations, parameters are assigned fixed value as  $Pr = 2$ ,  $M = Ec = n = 0.2$ ,  $Bi = 2$ ,  $\epsilon = 0.1$ ,  $Nt = Nb = 0.5$ ,  $We = \delta = 1$ ,  $Le = 5$ ,  $Rd = 0.8$ . For the whole study of this Chapter, these values remain constant except the varying parameter which is presented in the respective figure.

### 4.3.3 Effect of Weissenberg Number $We$

To expose the changes in the fluid motion, energy and concentration fields due to variation in the Weissenberg number  $We$ , Figs. 4.2(a)-(c) are delineated. The Fig. 4.2(a) represents the variation in the velocity profile due to enhancing Weissenberg number  $We$ . The curves of this graph shows that the velocity profile is declined. Physically, greater value of  $We$  means an increases in the relaxation time (it is the time that fluid takes to come back to it previous state) which causes the fluid motion to reduce whereas energy and concentration fields are enhanced as sketched in Figs. 4.2(b)-(c).





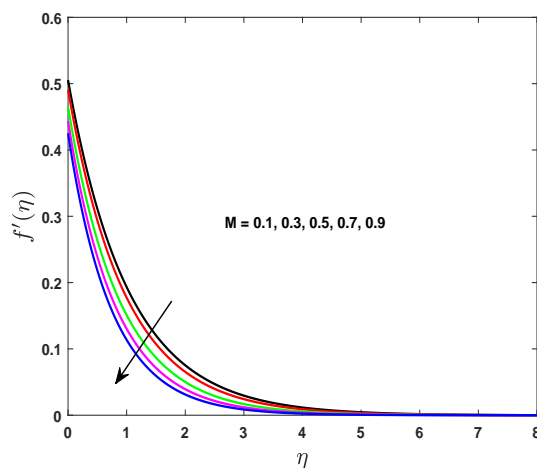
(c)

Fig. 4.2: Impact of  $We$  on (a) velocity, (b) temperature and (c) concentration profile.

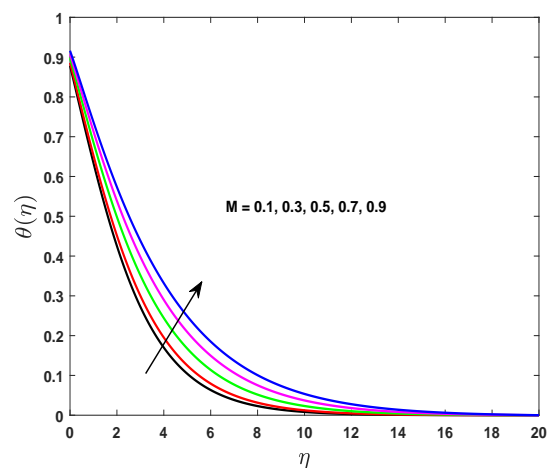
### 4.3.4 Effect of Magnetic Number $M$

Figs. 4.3(a)-(c) portray the impact of the magnetic number  $M$  on dimensionless flow fields. Higher value of the magnetic parameter results an enhancement in the opposing force (Lorentz force), due to this reason a depreciation in the dimensionless velocity profile is observed and is presented in Fig. 4.3(a).

An increment in the magnitude of the opposing force also leads the dimensionless temperature profile to enhance. This phenomenon is evident from the Fig. 4.3(b).



(a)



(b)

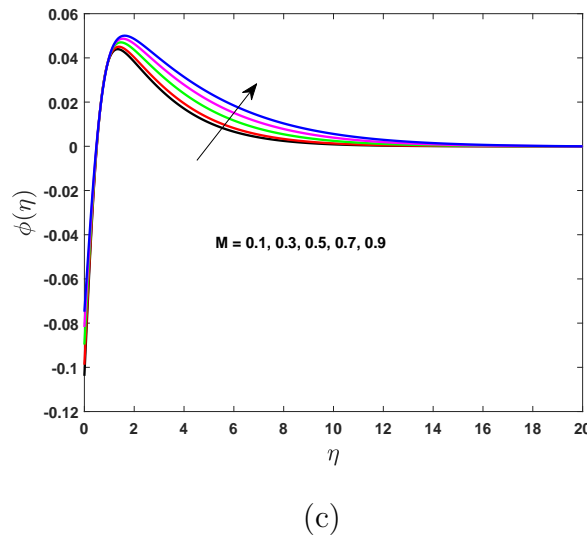


**Fig. 4.3:** Impact of  $M$  on (a) velocity, (b) temperature and (c) concentration profile.

It also verifies the general behavior of the magnetic effect. The energy field rises because the drag force is hiked up with the gradually mounting magnetic number values, as a result the resistance increases. Fig. 4.3(c) represents the impact of  $M$  on the concentration distribution. It is clear that the concentration profile is hiked as the magnetic number  $M$  is augmented.

### 4.3.5 Effect of Power-Law Index $n$

Figs. 4.4(a)-(c) are disseminated to study the impact of power-law index  $n$  on the dimensionless velocity, energy and concentration profiles. Fig. 4.4(a) is presented to view the effect of power-law index  $n$  on velocity profile. The dimensionless velocity is declined as power-law index  $n$  is intensified. Fig. 4.4(b) and Fig. 4.4(c) present the variations in the dimensionless temperature and the concentration profiles due to intensifying  $n$ . An enhancement in the value of  $n$  means an increment in the viscosity of the fluid. Due to this reason the fluid motion is declined whereas the temperature and the concentration fields are enhanced.

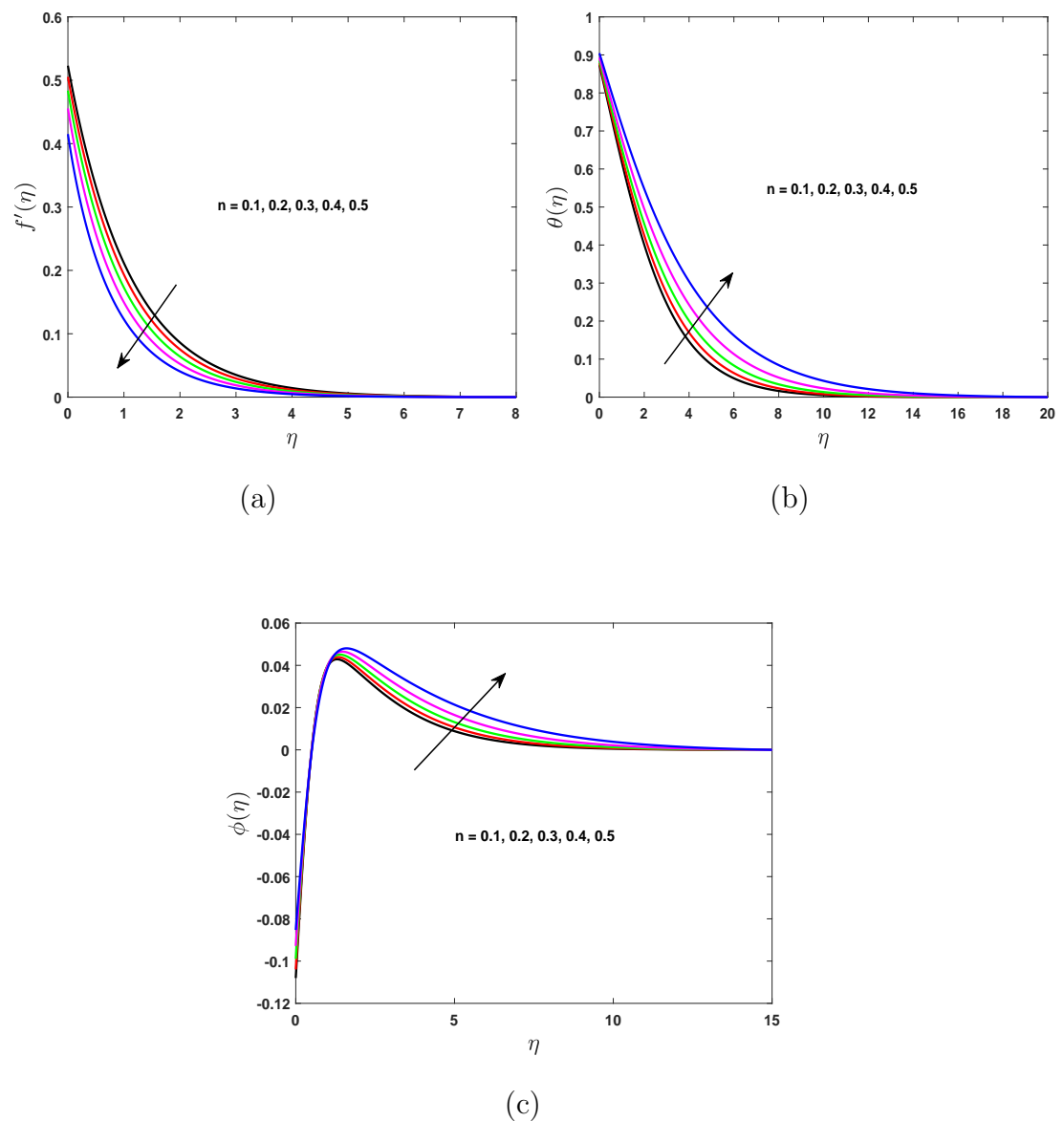


**Fig. 4.4:** Impact of  $n$  on (a) velocity, (b) temperature and (c) concentration profile.

### 4.3.6 Effect of Slip Parameter $\delta$

To observe the behaviour of the dimensionless velocity, temperature and concentration profile due to variation in the slip parameter, Figs. 4.5(a)-(c) are presented. Fig. 4.5(a) is presented to view the variation due to the slip parameter  $\delta$  on fluid motion. The fluid motion slows down for the growing values of  $\delta$ . Figs. 4.5(b)-(c) are illustrated to study the influence of  $\delta$  on energy and concentration field. Both

the energy and the concentration profiles are escalated for gradually mounting values of  $\delta$ .

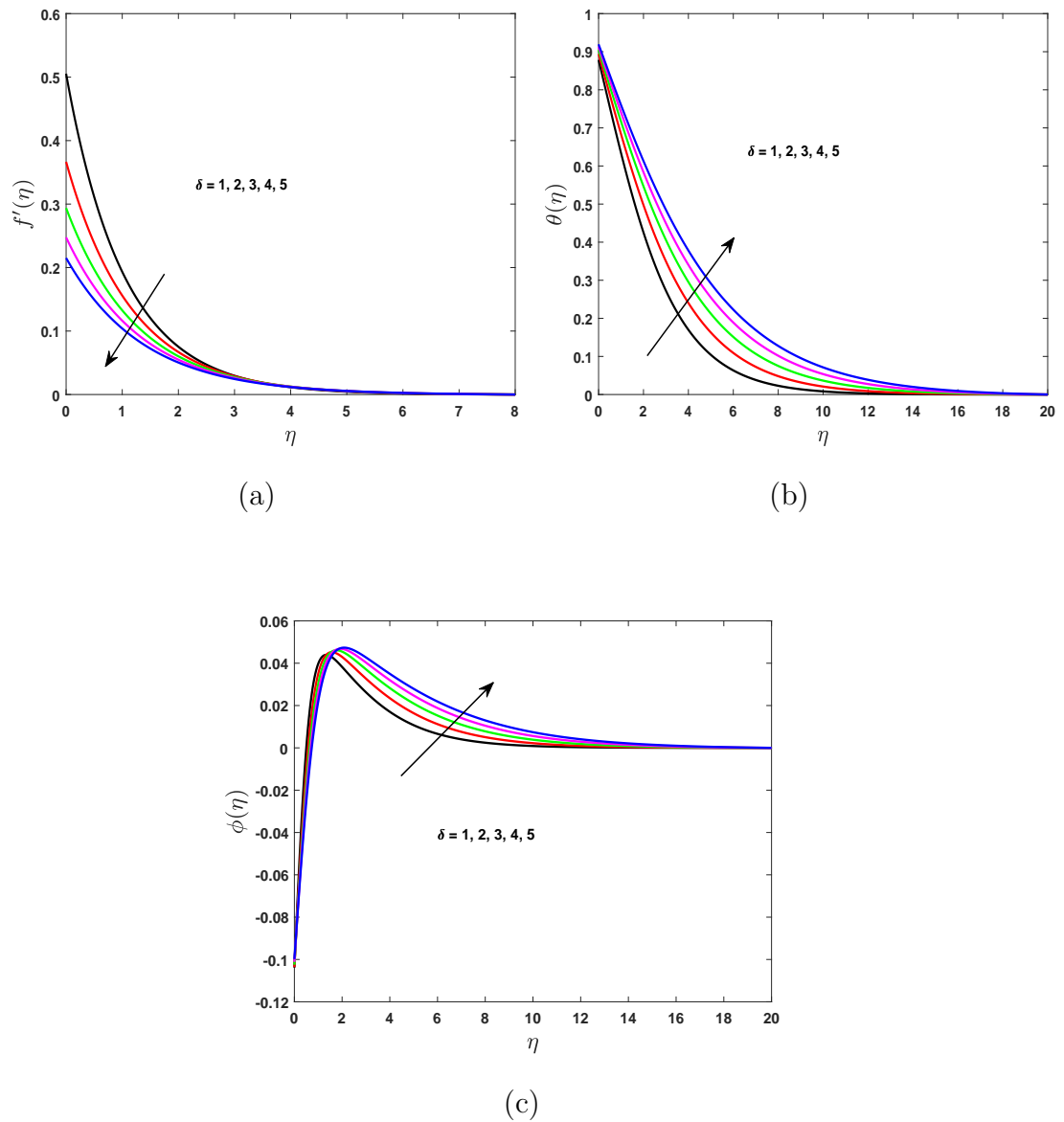


**Fig. 4.5:** Impact of  $\delta$  on (a) velocity, (b) temperature and (c) concentration profile.

### 4.3.7 Effect of Biot Number $Bi$

The effect of the Biot number  $Bi$  on energy and concentration profile are delineated in Figs. 4.6(a)-(b). Both the dimensionless profiles are enhanced for the growing values of  $Bi$ . Physically, convection through the surface is greater than



the conduction of heat inside the body due to which the temperature and the concentration profiles are enhanced.

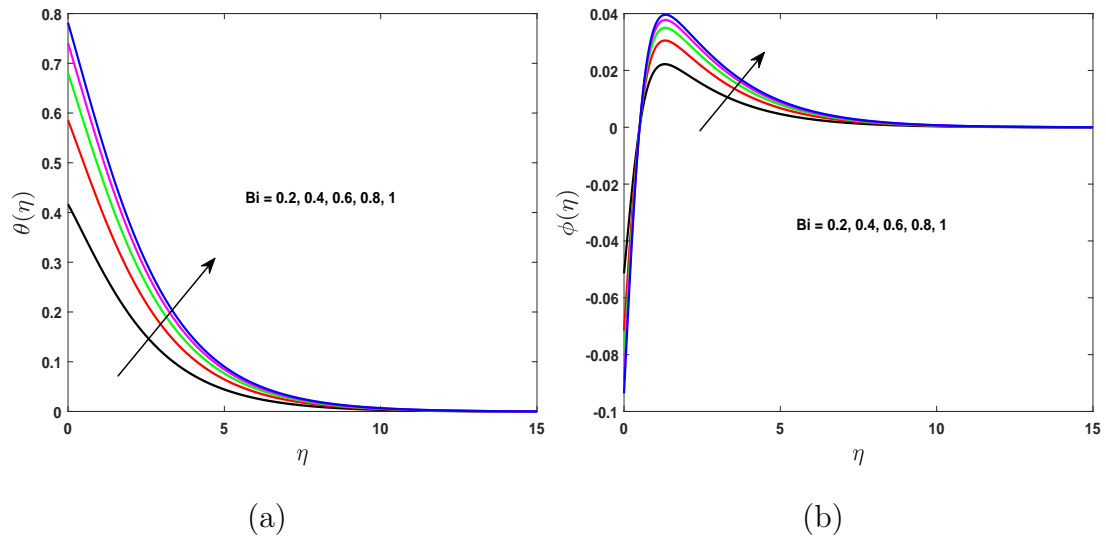


Fig. 4.6: Impact of  $Bi$  on (a) temperature and (b) concentration profile.

### 4.3.8 Effect of Prandtl Number $Pr$

Figs. 4.7(a)-(b) are chalked out to analyze the effect of the Prandtl number  $Pr$  on the dimensionless energy and the concentration profiles. Fig. 4.7(a) reflects the variation in the energy profile due to increment in  $Pr$ . From that figure it is evident that an enhancement in  $Pr$  causes a decrement in the energy profile.

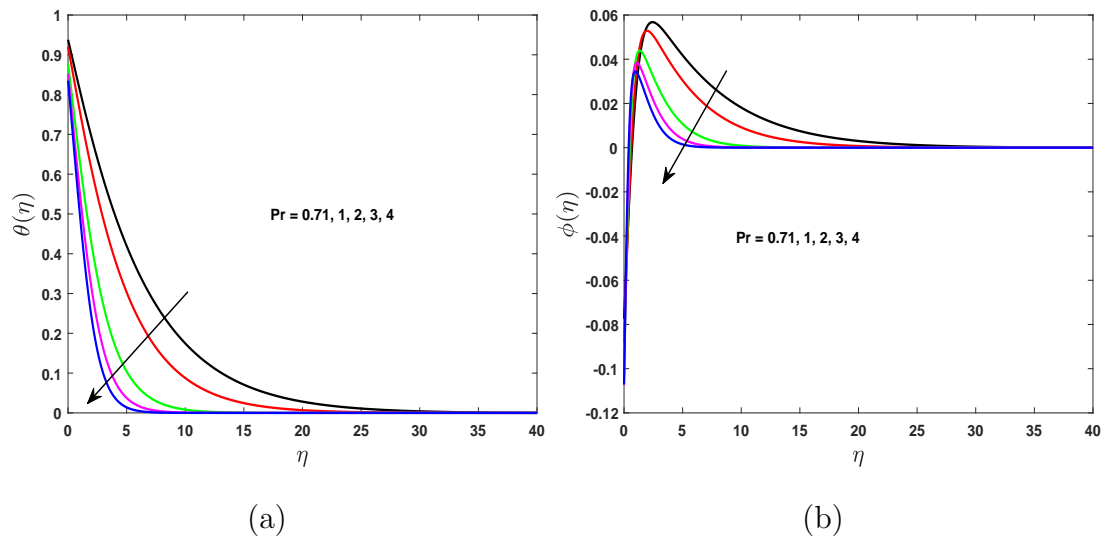
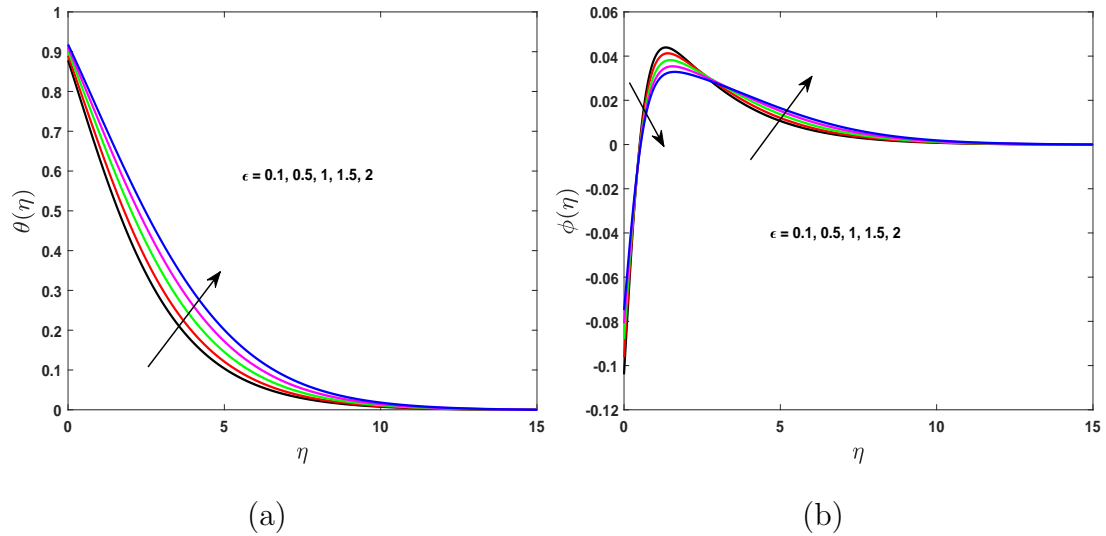


Fig. 4.7: Impact of  $Pr$  on (a) temperature and (b) concentration profile.

Physically, the thermal conductivity declines as the  $Pr$  is enhanced, due to this reason the thermal and the concentration profiles are declined. This phenomena is evident from Figs. 4.7(a)-(b).

### 4.3.9 Effect of Thermal Conductivity Parameter $\epsilon$



**Fig. 4.8:** Impact of  $\epsilon$  on (a) temperature and (b) concentration profile.

In Figs. 4.8(a)-(b) the temperature and the concentration fields against increasing values of thermal conductivity parameter  $\epsilon$  are drawn. Fig. 4.8(a) indicates that an acclivity in  $\epsilon$  results an acclivity in the thermal profile whereas the concentration profile is declined nearer to the surface and enhanced away from the surface. This phenomenon is evident from the Fig. 4.8(b).

### 4.3.10 Effect of Thermal Radiation Parameter $Rd$

Figs. 4.9(a)-(b) are divulged to study the impact of the thermal radiation  $Rd$  on the energy and the concentration profiles. The dimensionless temperature field is upsurged as the radiation parameter  $Rd$  is hiked as shown in Fig. 4.9(a). Physically, it strengthens the fact that more heat is generated in the radiation process for which the radiation parameter is increased. Fig. 4.9(b) is chalked out

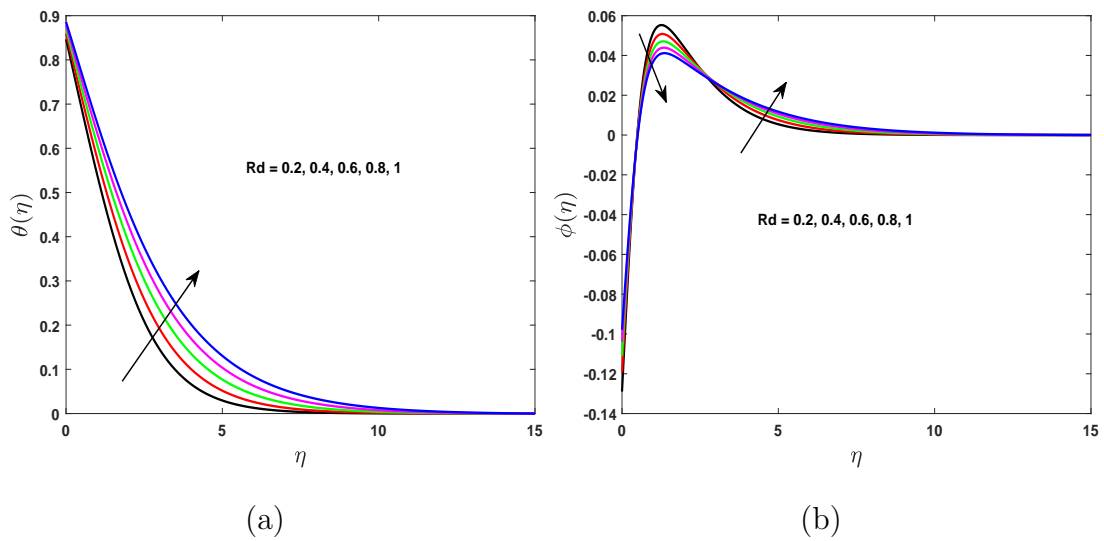


**Fig. 4.9:** Impact of  $Rd$  on (a) temperature and (b) concentration profile.

to highlight the influence of  $Rd$  on concentration field. The concentration profile is enhanced while moving away from the surface.

#### 4.3.11 Effect of Eckert Number $Ec$

The effect of viscous dissipation is presented by Eckert number  $Ec$ . It is a number that represents the relation between the kinetic energy and the change in enthalpy. Fig. 4.10(a) is outlined to visualize the effect of  $Ec$  on energy profile. An increment

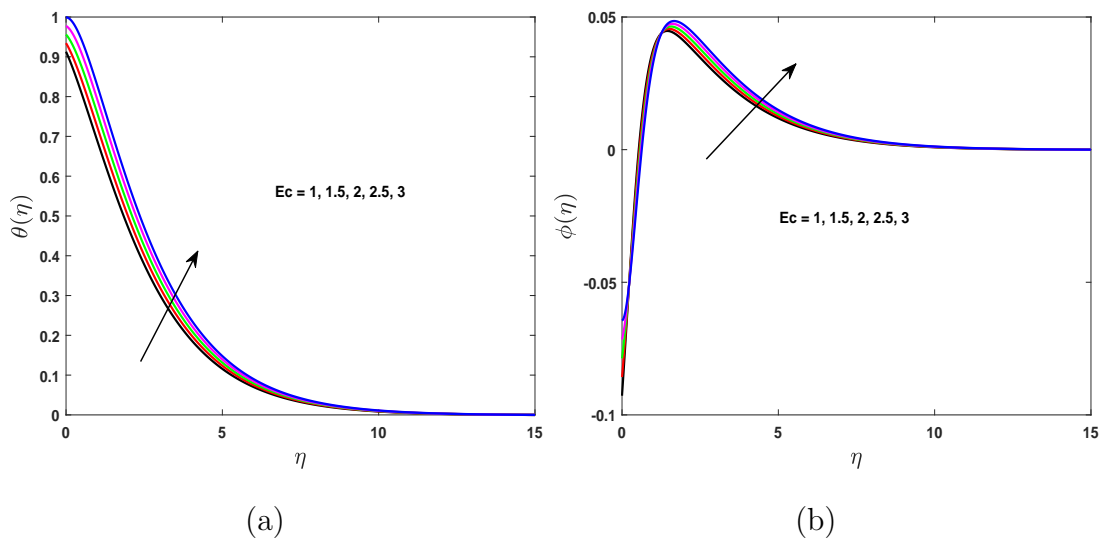


**Fig. 4.10:** Impact of  $Ec$  on (a) temperature and (b) concentration profile.

in  $Ec$  causes an acclivity in the thermal profile. Physically, as the dissipation is increased, the thermal conductivity improves which helps to increase the temperature profile. Fig. 4.10(b) shows the concentration distributions for the boosting values of  $Ec$ . The concentration field is upsurged for gradually boosting of  $Ec$ .

#### 4.3.12 Effect of Thermophoresis Parameter $Nt$

In the boundary layer region the thermophoretic effect on flow fields is significant. These effects are captured in Figs. 4.11(a)-(b). Graph of these figures shows that for gradually increasing  $Nt$ , both thermal and concentration profiles are upsurged. Physically, in thermophoresis the particles apply force on the other particles due to which particles from the hotter region move towards the colder region. Larger values of  $Nt$  means more application of the force on the other particles and as a result more fluid moves from the higher temperature region to the less hotter region. Due to this fact increment in the thermal and the nanoparticles concentration is noticed.

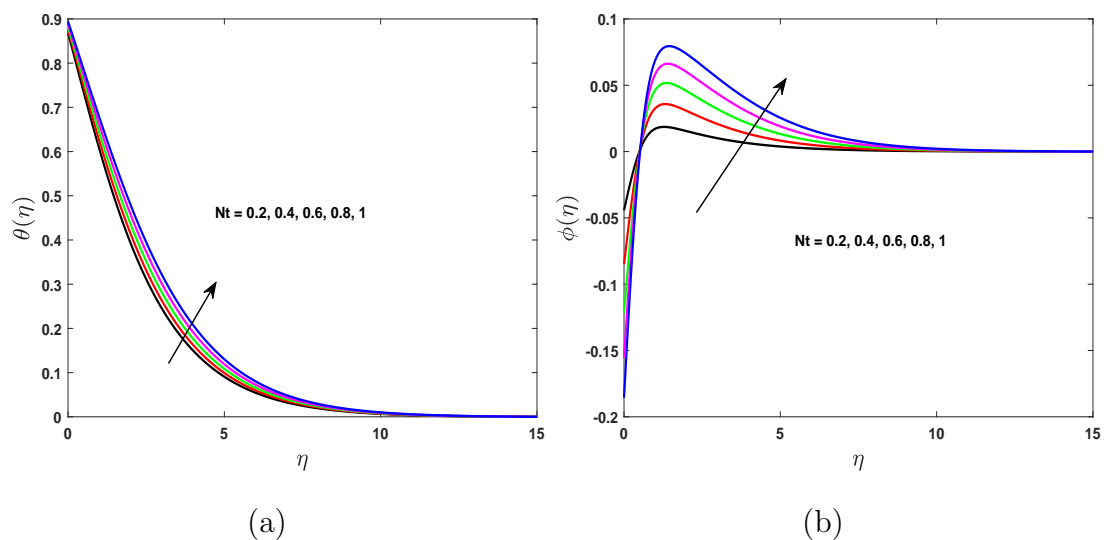


**Fig. 4.11:** Impact of  $Nt$  on (a) temperature and (b) concentration profile.

It is noticeable that in all concentration profiles, the behaviours are opposite after some value of  $\eta$ . As no particle can leave the surface, the concentration at the lower

surface is higher as compare to the concentration at the upper surface, therefore after some value of  $\eta$  the behavior is opposite [6, 94, 95].

## 4.4 Conclusions

In this chapter, MHD radiative tangent hyperbolic nanofluid with convective and slip conditions has been analyzed. The key features are enumerated below:

- The velocity profile is declined for the large value of the velocity slip parameter  $\delta$ .
- The temperature distribution is enhanced for the growing values of each of the velocity slip parameter  $\delta$  and the Biot number  $Bi$ .
- The concentration field is enhanced as the velocity slip parameter  $\delta$ , the Biot number  $Bi$  and the Eckert number  $Ec$  is hiked.

## Chapter 5

# Heat and Mass Transfer Analysis of Time-Dependent Tangent Hyperbolic Nanofluid Flow Past a Wedge

The candid intension of this work is to inspect the time dependent magnetohydrodynamic tangent hyperbolic nanofluid. The nanofluid flow has been assumed to be directed by a wedge on its way. In addition the convective heating mode and thermal radiation phenomenon have also been inspected. The formulated PDEs are converted into the nonlinear ODEs by utilizing similarity transformation. Shooting technique is implemented to solve the ODEs for the two cases; the flow over a static wedge and the stretching wedge. The effect of intricate parameters on different flow fields has been analyzed graphically and discussed in detail.

### 5.1 Problem Formulation

The stagnation point flow of time dependent magnetohydrodynamic tangent hyperbolic fluid past a stretching wedge has been scrutinized in the presence of

nanoparticles. The wedge is stretched with stretching velocity  $\tilde{U}_w(x, t) = \frac{bx^m}{1-ct}$  with  $b$  as a stretching rate and  $\tilde{U}_e(x, t) = \frac{ax^m}{1-ct}$  is the free stream velocity, where  $a$ ,  $m$  and  $c$  are constants with  $0 \leq m \leq 1$ . The wedge angle is taken as  $\chi = \pi\beta$  where  $\beta = \frac{2m}{1+m}$ , known as the Hartree pressure gradient. The wedge is positioned along  $x$  - axis and  $y$  - axis is normal to the wedge. The horizontal and the vertical components of the velocity have been denoted by  $\tilde{u}$  and  $\tilde{v}$ . The initial reference temperature and concentration have been considered as  $\tilde{T}_0$  and  $\tilde{C}_0$  respectively.  $\tilde{T}_w$  and  $\tilde{T}_\infty$  denote the temperature of the fluid and ambient temperature respectively and fluid temperature has been considered as  $\tilde{T}_w(x, t) = \tilde{T}_\infty + \frac{\tilde{T}_0 \tilde{U}_w x}{\nu(1-ct)^{1/2}}$ . The ambient concentration  $\tilde{C}_\infty$  is lower than the surface concentration which is consider as  $\tilde{C}_w(x, t) = \tilde{C}_\infty + \frac{\tilde{C}_0 \tilde{U}_w x}{\nu(1-ct)^{1/2}}$ . Convective heating mode has been considered with coefficient of heat transfer as  $h_f$ . A time dependent magnetic field  $B(t) = \frac{B_0}{(1-ct)^{1/2}}$ , normal to the surface is applied as illustrated in the Fig. 5.1. Being within the above constraints, the basic equations for the above problem are [75]:

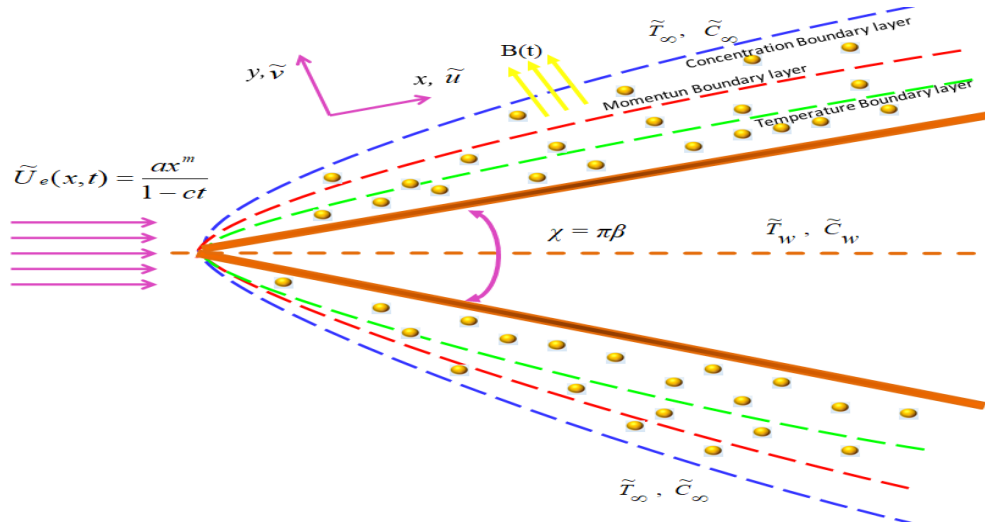


**Fig. 5.1:** Geometrical illustration of the problem.

$$\frac{\partial \tilde{u}}{\partial x} + \frac{\partial \tilde{v}}{\partial y} = 0, \quad (5.1)$$

$$\begin{aligned} \frac{\partial \tilde{u}}{\partial t} + \tilde{u} \frac{\partial \tilde{u}}{\partial x} + \tilde{v} \frac{\partial \tilde{u}}{\partial y} &= \frac{\partial \tilde{U}_e}{\partial t} + \tilde{U}_e \frac{\partial \tilde{U}_e}{\partial x} + \nu \left( 1 - n + \sqrt{2n}\Gamma \frac{\partial \tilde{u}}{\partial y} \right) \frac{\partial^2 \tilde{u}}{\partial y^2} \\ &\quad - \frac{\sigma B_0^2}{\rho} (\tilde{u} - \tilde{U}_e), \end{aligned} \quad (5.2)$$

$$\begin{aligned} \frac{\partial \tilde{T}}{\partial t} + \tilde{u} \frac{\partial \tilde{T}}{\partial x} + \tilde{v} \frac{\partial \tilde{T}}{\partial y} = \alpha \frac{\partial^2 \tilde{T}}{\partial y^2} - \frac{1}{(\rho C_p)} \frac{\partial q_r}{\partial y} \\ + \frac{(\rho C_p)_p}{(\rho C_p)_f} \left[ D_B \frac{\partial \tilde{C}}{\partial y} \frac{\partial \tilde{T}}{\partial y} + \frac{D_T}{\tilde{T}_\infty} \left( \frac{\partial \tilde{T}}{\partial y} \right)^2 \right]. \end{aligned} \quad (5.3)$$

$$\frac{\partial \tilde{C}}{\partial t} + \tilde{u} \frac{\partial \tilde{C}}{\partial x} + \tilde{v} \frac{\partial \tilde{C}}{\partial y} = \frac{D_T}{\tilde{T}_\infty} \frac{\partial^2 \tilde{T}}{\partial y^2} + D_B \frac{\partial^2 \tilde{C}}{\partial y^2}, \quad (5.4)$$

The implemented BCs in the free stream and at the stretching wedge are:

$$\left. \begin{aligned} \tilde{u} = \tilde{U}_w = \lambda \tilde{U}_e, \quad \tilde{v} = 0, \quad -k \frac{\partial \tilde{T}}{\partial y} = h_f (\tilde{T}_w - \tilde{T}), \quad \tilde{C} = \tilde{C}_w \text{ at } y = 0, \\ \tilde{u} \rightarrow \tilde{U}_e, \quad \tilde{T} \rightarrow \tilde{T}_\infty, \quad \tilde{C} \rightarrow \tilde{C}_\infty \text{ as } y \rightarrow \infty. \end{aligned} \right\} \quad (5.5)$$

In the above equations  $\alpha$  is the thermal diffusivity,  $\sigma$  represents the constant electrical conductivity.  $\rho_f$ ,  $\rho_p$ ,  $(C_p)_f$  and  $(C_p)_p$  represents the density of fluid, density of nanoparticles, specific heat of the fluid and nanoparticles respectively.  $n$  denotes the power-law index. Furthermore,  $D_T$  and  $D_B$  are the thermal and the Brownian diffusion parameters respectively.

In Eq. (5.3),  $q_r$  is the Rosseland radiative heat flux as defined in (3.7) of chapter 3. To make the modeled equations dimensionless, the following transformations [76] have been introduced.

$$\left. \begin{aligned} \eta = y \sqrt{\frac{(m+1)\tilde{U}_e}{2\nu x}}, \quad \psi = \sqrt{\frac{2\nu x \tilde{U}_e}{m+1}} f(\eta), \\ \theta(\eta) = \frac{\tilde{T} - \tilde{T}_\infty}{\tilde{T}_w - \tilde{T}_\infty}, \quad \phi(\eta) = \frac{\tilde{C} - \tilde{C}_\infty}{\tilde{C}_w - \tilde{C}_\infty}. \end{aligned} \right\} \quad (5.6)$$

As a result, (5.1) is satisfied identically and Eqs. (5.2)-(5.4) yield the following ODEs:

$$\begin{aligned} (1 - n + nWe f'') f''' - (2 - \beta) A \left( \frac{\eta}{2} f'' + f' - 1 \right) - \beta (f'^2 - 1) + f f'' \\ - M(2 - \beta)(f' - 1) = 0, \end{aligned} \quad (5.7)$$

$$\begin{aligned} \left( 1 + \frac{4}{3} Rd \right) \theta'' + Pr \left[ (f\theta' - 2f'\theta) - \frac{A}{2} (2 - \beta) (\eta\theta' + 3\theta) \right. \\ \left. + Nb\theta'\phi' + Nt\theta'^2 \right] = 0, \end{aligned} \quad (5.8)$$



$$\phi'' + PrLe \left[ (f\phi' - 2f'\phi) - \frac{A}{2} (2 - \beta) (\eta\phi' + 3\phi) \right] + \frac{Nt}{Nb} \theta'' = 0. \quad (5.9)$$

The associated BCs are

$$\left. \begin{aligned} f(\eta) = 0, \quad f'(\eta) = \lambda, \quad \phi(\eta) = 1, \\ \theta'(\eta) = -\gamma (2 - \beta)^{1/2} (1 - \theta), \\ f'(\eta) \rightarrow 1, \quad \theta(\eta) \rightarrow 0, \quad \phi(\eta) \rightarrow 0 \text{ as } \eta \rightarrow \infty. \end{aligned} \right\} \text{ at } \eta = 0 \quad (5.10)$$

In the above equations,  $Nb$  denotes the Brownian motion parameter,  $Pr$  Prandtl number,  $We$  Weissenberg number,  $M$  magnetic number,  $Le$  Lewis number,  $Ec$  Eckert number,  $Nt$  thermophoresis parameter,  $\gamma$  generalized Biot number,  $A$  unsteadiness parameter,  $Re_x$  the local Reynolds number,  $\lambda$  velocity ratio parameter and  $Rd$  thermal radiation parameter. These parameters are formulated as:

$$\begin{aligned} Nb &= \frac{(\rho C_p)_p D_B (\tilde{C}_w - \tilde{C}_\infty)}{\nu (\rho C_p)_f}, \quad Pr = \frac{\nu}{\alpha}, \quad We = \sqrt{\frac{\Gamma^2 (m+1) \tilde{U}_e^3}{\nu x}}, \quad M = \frac{\sigma B_0^2}{a \rho x^{m-1}}, \quad Le = \frac{\alpha}{D_B}, \\ Ec &= \frac{\tilde{U}_w^2}{(C_p)_f (\tilde{T}_w - \tilde{T}_\infty)}, \quad Nt = \frac{(\rho C_p)_p D_T (\tilde{T}_w - \tilde{T}_\infty)}{(\rho C_p)_f \nu \tilde{T}_\infty}, \quad \gamma = \frac{h_f}{k} x Re_x^{-1/2}, \quad A = \frac{c}{a x^{m-1}}, \quad Re_x = \frac{x \tilde{U}_e}{\nu}, \\ \lambda &= \frac{\tilde{U}_w}{\tilde{U}_e}, \quad Rd = \frac{4\sigma^* \tilde{T}_\infty^3}{k \kappa^*}. \end{aligned}$$

## 5.2 Quantities of Interest

From engineering and industrial point of view the surface drag, the Nusselt number and the Sherwood number are the quantities of foremost interests. In the present section these quantities have been formulated in both the dimensional and the non dimensional form as follows:

### 5.2.1 The Skin Friction Coefficient

The surface drag or the skin friction is an imperative feature of the boundary layer and is defined as

$$C_f = \frac{\tau_w}{\rho_f \tilde{U}_w^2}.$$

The wall shear stress  $\tau_w$ , for the present model it is given by

$$\tau_w = \mu \left[ (1-n) \frac{\partial \tilde{u}}{\partial y} + \frac{n\Gamma}{\sqrt{2}} \left( \frac{\partial \tilde{u}}{\partial y} \right)^2 \right]_{y=0}.$$

In dimensionless form

$$C_f Re_x^{1/2} \sqrt{\frac{2}{m+1}} = (1-n) f''(0) + \frac{n}{2} We (f''(0))^2. \quad (5.11)$$

### 5.2.2 The Nusselt Number

The Nusselt number is given by

$$Nu = \frac{xq_w}{k(\tilde{T}_w - \tilde{T}_\infty)}.$$

In above equation,  $q_w$  is the wall heat flux at the surface and for the present model it is given by

$$q_w = -k \left[ \left( 1 + \frac{16\sigma^* \tilde{T}_\infty}{3k\kappa^*} \right) \frac{\partial \tilde{T}}{\partial y} \right]_{y=0}.$$

In the dimensionless form

$$Nu_x Re_x^{-1/2} \sqrt{\frac{2}{m+1}} = - \left( 1 + \frac{4}{3} Rd \right) \theta'(0). \quad (5.12)$$

### 5.2.3 The Sherwood Number

The Sherwood number is given by

$$Sh = \frac{xq_m}{D_B(\tilde{C}_w - \tilde{C}_\infty)}.$$

In above equation,  $D_B$  is the Brownina diffusion parameter and  $q_m$  is the mass flux at the surface.

For the current problem it is given by

$$q_m = -D_B \left( \frac{\partial \tilde{C}}{\partial y} \right)_{y=0}.$$

In non-dimensional form

$$Sh_x Re_x^{-1/2} \sqrt{\frac{2}{m+1}} = -\phi'(0). \tag{5.13}$$

where  $Re_x = \frac{xU_e}{\nu}$ .

### 5.3 Implementation of the Numerical Scheme

The system of ODEs (5.7)-(5.9) subject to the BCs (5.10) is solved by utilizing the shooting technique [92]. For the implementation of the shooting technique, we need a system of first order ODEs. For this purpose we bring in new variables,  $\zeta_1 = f, \zeta_2 = f', \zeta_3 = f'', \zeta_4 = \theta, \zeta_5 = \theta', \zeta_6 = \phi$ , and  $\zeta_7 = \phi'$  to have the following set of seven first order ODEs:

$$\left. \begin{aligned} \zeta_1' &= \zeta_2, \\ \zeta_2' &= \zeta_3, \\ \zeta_3' &= \frac{(2-\beta)(M(\zeta_2-1) + A(\frac{\eta}{2}\zeta_3 + \zeta_2 - 1)) + \beta(\zeta_2^2 - 1) - \zeta_1\zeta_3}{(1-n+nWe\zeta_3)}, \\ \zeta_4' &= \zeta_5, \\ \zeta_5' &= \frac{-3Pr \left[ \zeta_1\zeta_5 - 2\zeta_2\zeta_4 - \frac{A}{2}(2-\beta)(\eta\zeta_5 + 3\zeta_4) + Nb\zeta_5\zeta_7 + Nt\zeta_5^2 \right]}{(3+4Rd)}, \\ \zeta_6' &= \zeta_7, \\ \zeta_7' &= PrLe \left[ \frac{A}{2}(2-\beta)(\eta\zeta_7 + 3\zeta_6) - (\zeta_1\zeta_7 - 2\zeta_2\zeta_6) \right] - \frac{Nt}{Nb}\zeta_5'. \end{aligned} \right\} \tag{5.14}$$

The associated boundary conditions are

$$\left. \begin{aligned} \zeta_1(\eta) = 0, \quad \zeta_2(\eta) = \lambda, \\ \zeta_5(\eta) = -\gamma(2-\beta)^{1/2}(1-\zeta_4(\eta)), \quad \zeta_6(\eta) = 1, \\ \zeta_2(\infty) \rightarrow 1, \quad \zeta_4(\infty) \rightarrow 0, \quad \zeta_6(\infty) \rightarrow 0, \quad \text{as } \eta \rightarrow \infty. \end{aligned} \right\} \text{at } \eta = 0, \tag{5.15}$$

To solve the above modeled problem with the assistance of the shooting method, seven initial conditions are required. Therefore, we guess the three missing conditions as  $\zeta_3(0) = s_1$ ,  $\zeta_4(0) = s_2$  and  $\zeta_7(0) = s_3$ . The suitable guesses for  $s_1$ ,  $s_2$  and  $s_3$  are chosen in such a way that three known boundary conditions are approximately satisfied for  $\eta \rightarrow \infty$ . Classical Newton method is utilized to improve the estimates  $s_1$ ,  $s_2$  and  $s_3$  until the following benchmark is achieved.

$$\max\{|\zeta_2(\eta_{max}) - 1|, |\zeta_4(\eta_{max}) - 0|, |\zeta_6(\eta_{max}) - 0|\} < 10^{-6}.$$

The computations for the various emerging physical parameters have been performed over an appropriate bounded domain  $[0, \eta_{max}]$  instead of  $[0, \infty)$ . It is noticed that for growing values of  $\eta_{max}$ , no significant variations are observed in the results.

### 5.3.1 Validation of Code

To check the reliability and validation of our MATLAB code, the values of  $-f''(0)$ , reported by Rajagopal *et al.* [79], Kuo [81] and Ishak *et al.* [83] have been reproduced. The present computations have good concord with the results in the above published articles.

$\beta$	[79]	[81]	[83]	Present study
0.0	-	0.469600	0.4696	0.469600
0.1	0.587035	0.587080	0.5870	0.587035
0.3	0.774755	0.774724	0.7748	0.774757
0.5	0.927680	0.927905	0.9277	0.927681
1	1.232585	1.238589	1.2326	1.232588

Table 5.1: Comparison of the presently computed values of  $-f''(0)$ .

## 5.4 Results and Discussion

To view insight the modelled problem, the skin friction coefficient, the Nusselt number and Sherwood number have been computed numerically and discussed for the various pertinent parameters in the subsequent section.

### 5.4.1 The Skin Friction Coefficient

Table. 5.2 is presented to investigate the behaviour of the surface drag or the skin friction coefficient  $Re_x^{-1/2}C_f\sqrt{\frac{2}{m+1}}$  for the gradually boosting  $n, \beta, A, We, M$  and  $\lambda$ . It is noticed that the surface drag is hiked as each of the magnetic number  $M$ , the Weissenberg number  $We$ , the unsteadiness parameter  $A$  and the Hartree pressure gradient  $\beta$  is enhanced whereas diminution is noticed for accelerating values of the power-law index  $n$  and the velocity ratio parameter  $\lambda$ .

$A$	$n$	$We$	$M$	$\beta$	$\lambda$	$C_f Re_x^{1/2} \sqrt{\frac{2}{m+1}}$
0.2	0.2	1	1	0.1	0.3	1.061838
0.3						1.090551
0.4						1.118823
0.2	0.1					1.096961
	0.3					1.026628
	0.5					0.956041
	0.2	2				1.104233
		3				1.141895
		4				1.176062
		1	0.5			0.841418
			1			1.061838
			1.5			1.247852
			1	0.2		1.070039
				0.4		1.086280
				0.6		1.102315
				0.1	0.2	1.210344
					0.4	0.912185
					0.6	0.610086

Table 5.2: Variation in the  $C_f Re_x^{1/2} \sqrt{\frac{2}{m+1}}$  various physical parameters when  $Le = Rd = Pr = 1, Nt = Nb = 0.3, \gamma = 0.1$ .

### 5.4.2 The Nusselt Number

Table 5.3 is displayed to investigate the behaviour of the Nusselt number  $-Re_x^{-1/2}Nu_x\sqrt{\frac{2}{m+1}}$  for the various assorted parameters. The escalating values of the thermal radiation parameter  $Rd$ , the generalized Biot number  $\gamma$ , the unsteadiness parameter  $A$ , the Prandtl number  $Pr$  and the velocity ratio parameter  $\lambda$  cause an increment in the Nusselt number whereas reverse trends are observed for the Hartree pressure gradient  $\beta$ , the Brownian motion parameter  $Nb$  and the thermophoresis parameter  $Nt$ .

$Pr$	$Rd$	$Nb$	$Nt$	$A$	$\beta$	$\gamma$	$\lambda$	$-Re_x^{-1/2}Nu_x\sqrt{\frac{2}{m+1}}$
1	1	0.3	0.3	0.2	0.1	0.1	0.3	0.278023
	2							0.286521
	3							0.290062
1	2							0.425215
	3							0.567332
	4							0.705384
	1	0.2						0.278792
		0.4						0.277240
		0.6						0.275638
		0.3	0.2					0.278088
			0.4					0.277957
			0.6					0.277825
			0.3	0.2				0.278023
				0.3				0.279952
				0.4				0.281656
				0.2	0.2			0.271426
					0.4			0.264613
					0.6			0.257563
					0.1	0.2		0.489194
						0.4		0.787618
						0.6		0.987721
						0.1	0.2	0.276726
							0.4	0.279214
							0.6	0.281332

Table 5.3: Variation in the  $-Re_x^{-1/2}Nu_x\sqrt{\frac{2}{m+1}}$ , various physical parameters when  $M = We = Le = 1, n = 0.2$ .

### 5.4.3 The Sherwood Number

To study the behaviour of Sherwood number  $-Re_x^{-1/2} Sh_x \sqrt{\frac{2}{m+1}}$ , due to the variation in different physical parameters, Table 5.4 is presented. From this table it is studied that the Sherwood number is enhanced as the unsteadiness parameter  $A$ , the Brownian motion parameter  $Nb$ , the Lewis number  $Le$ , the velocity ratio parameter  $\lambda$  and the Prandtl number  $Pr$  is augmented whereas it is depressed for the rising values of the Hartree pressure gradient  $\beta$ , the thermophoresis parameter  $Nt$ , the generalized Biot number  $\gamma$ .

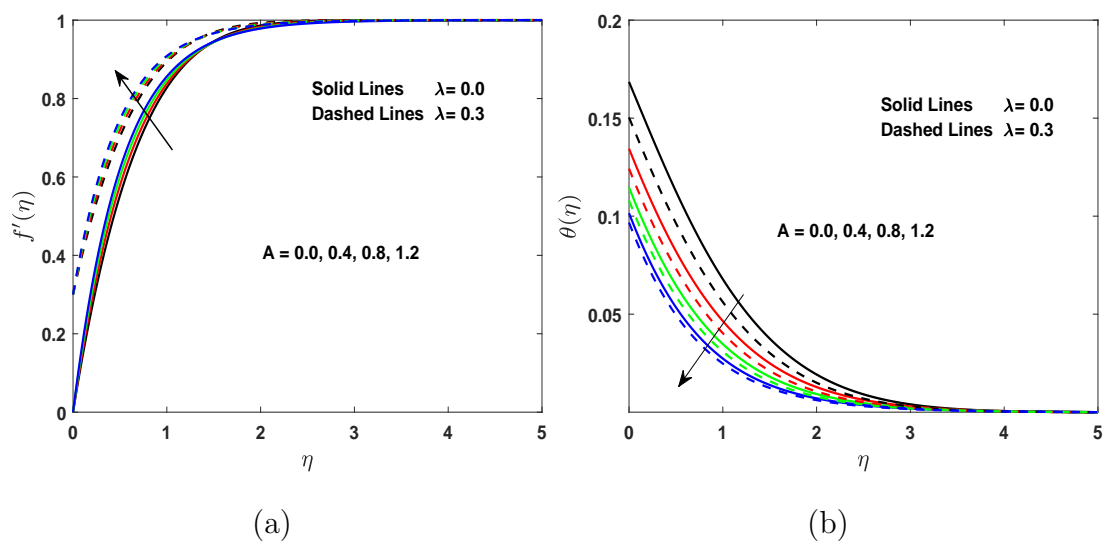
$A$	$\beta$	$Le$	$Nt$	$Nb$	$Pr$	$\gamma$	$\lambda$	$-Re_x^{-1/2} Sh_x \sqrt{\frac{2}{m+1}}$
0.2	0.1	1	0.3	0.3	1	0.1	0.3	1.335687
	0.4							1.486632
	0.6							1.627066
0.2	0.2							1.329820
	0.4							1.318054
	0.6							1.306267
	0.1	2						1.847553
		3						2.229797
		4						2.547403
		1	0.2					1.348248
			0.4					1.323185
			0.6					1.298355
			0.3	0.2				1.314956
				0.4				1.346062
				0.6				1.356455
				0.3	2			1.840089
					3			2.220323
					4			2.538080
					1	0.2		1.307248
						0.4		1.267524
						0.6		1.241197
						0.1	0.2	1.279852
							0.4	1.390015
							0.6	1.494381

Table 5.4: Variation in the  $-Re_x^{-1/2} Sh_x \sqrt{\frac{2}{m+1}}$  for various physical parameters when  $M = We = Rd = 1, n = 0.2$ .

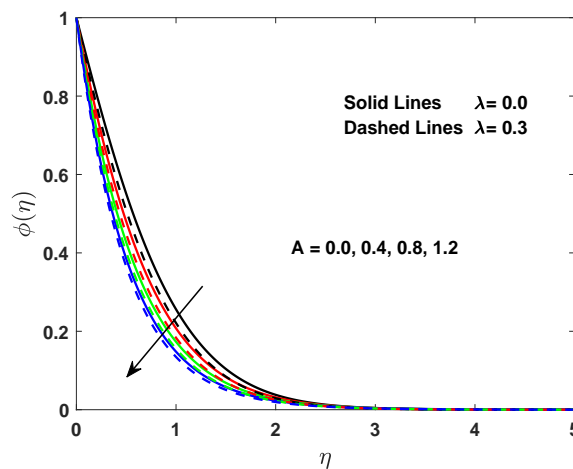
In the subsequent subsections, graphical results of this investigation have been presented in terms of flow distributions for the different prominent parameters. In order to execute the numerical simulations, all parameters are assigned fixed values as  $A = n = 0.2$ ,  $Nt = Nb = 0.3$ ,  $M = We = Rd = Le = Pr = 1$ ,  $\gamma = 0.1$ , and  $\beta = 0.1$ . For the whole investigation in this Chapter, the values of these parameters are kept constant except the varying parameter which is presented in the respective figure. All the graphical results are disseminated for the flow over a static wedge ( $\lambda = 0.0$ ) and stretching wedge ( $\lambda = 0.3$ ).

#### 5.4.4 Effect of Unsteadiness Parameter $A$

To expose the effect of the unsteadiness parameter  $A$  on fluid motion, temperature and concentration profiles, Figs. 5.2(a)-(c) are sketched. Fig. 5.2(a) depicts that the higher values of the unsteadiness parameter show an accelerating behaviour in the nanofluid velocity in both static and stretching wedge. In both cases the fluid motion and related boundary layer is higher in case of stretching wedge ( $\lambda = 0.3$ ). Fig. 5.2(b) reflects that the increase in unsteadiness parameter  $A$ , decreases the energy field. Physically, an enhancement in the unsteadiness parameter causes the stretching surface to lose its heat, due to which the temperature of the nanofluid is declined. Fig. 5.2(c) depicts the impact of  $A$  on the concentration field. A declivity is noticed in the concentration field for the escalating values of  $A$ .





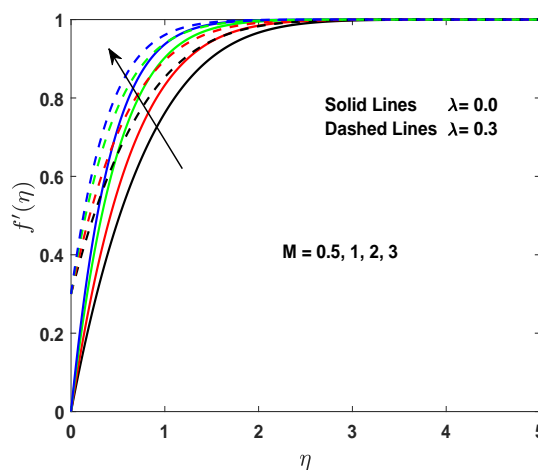


(c)

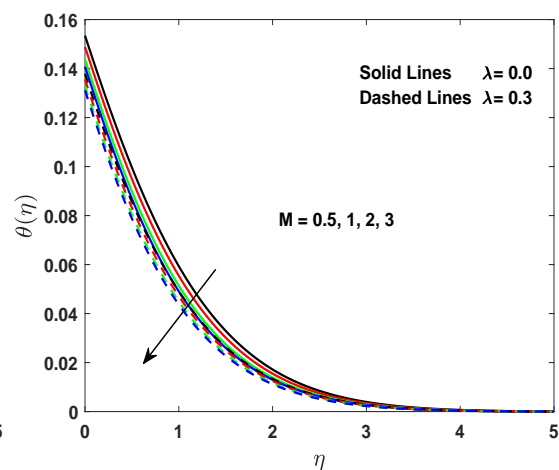
Fig. 5.2: Impact of  $A$  on (a) velocity, (b) temperature and (c) concentration profile.

### 5.4.5 Effect of Magnetic Parameter $M$

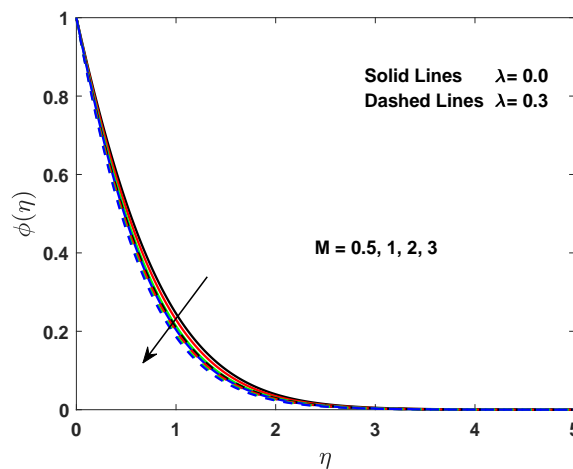
Figs. 5.3(a)-(c) are chalked out to observe the flow distributions effected by the magnetic number  $M$ . Fig. 5.3(a) shows that the fluid motion at any point is hiked due to an increment in the magnetic number. It is due to the less domination of the decelerating force. Figs. 5.3(b)-(c) are presented to investigate the effect of  $M$  on energy and concentration profiles. In both static and stretching wedge, decreasing trends are noticed in energy and nanoparticles concentration distributions.



(a)



(b)

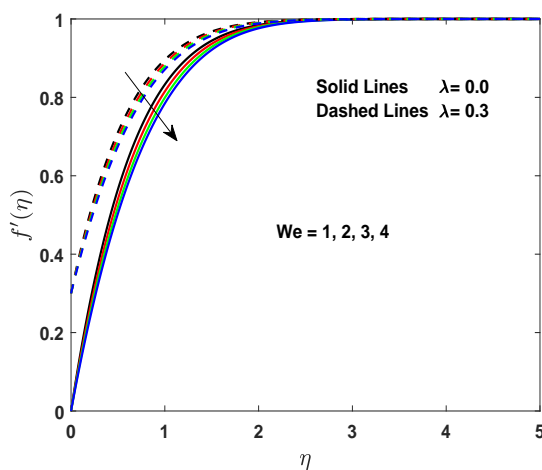


(c)

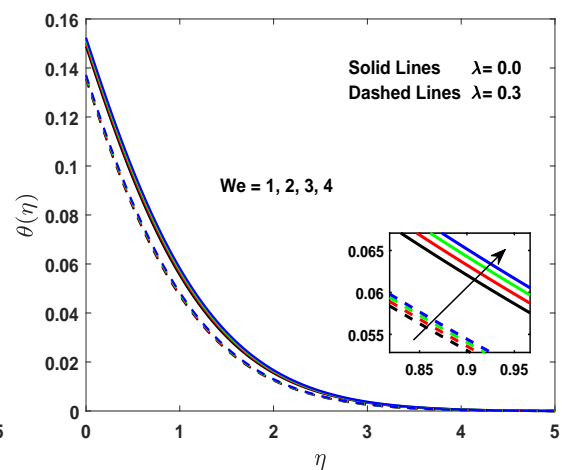
Fig. 5.3: Impact of  $M$  on (a) velocity, (b) temperature and (c) concentration profile.

### 5.4.6 Effect of Weissenberg Number $We$

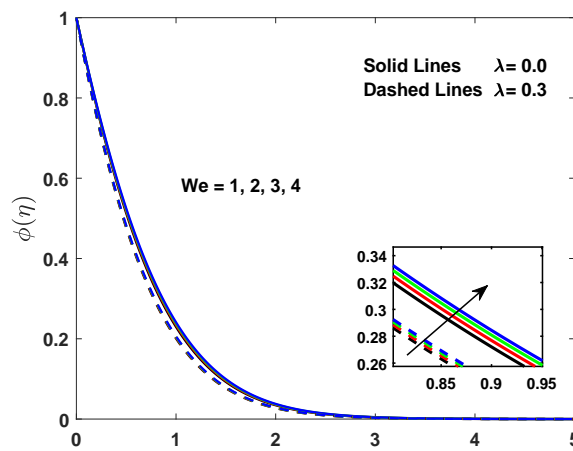
Figs. 5.4(a)-(c) are delineated to examine the effect of the Weissenberg number  $We$  on the fluid motion, thermal and concentration distributions. Fig. 5.4(a) reveals that the fluid velocity is reduced whereas momentum boundary layer thickness is intensified as values of  $We$  are increased. Fig. 5.4(b) is displayed to clear that the temperature of the nanofluid is appreciated for the gradually boosting values of  $We$ . Increasing  $We$  means a rise in the relaxation time, which results an increment



(a)



(b)



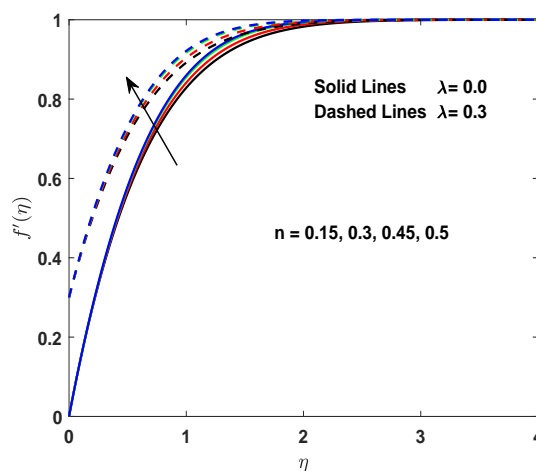
(c)

Fig. 5.4: Impact of  $We$  on (a) velocity, (b) temperature and (c) concentration profile.

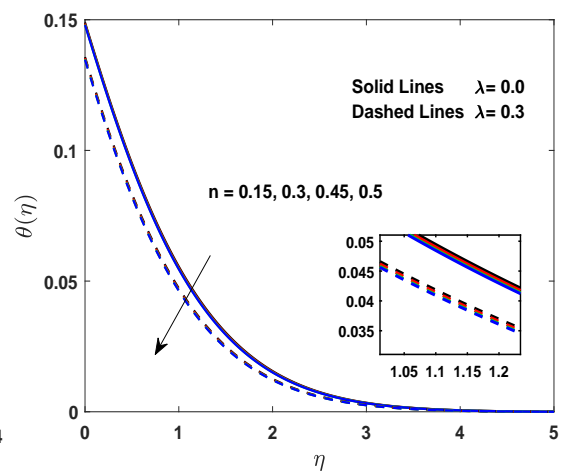
in the temperature. Fig. 5.4(c) is delineated to study the behaviour of  $We$  on concentration of nanoparticles. An augmentation in  $We$  produces an increment in the concentration field.

### 5.4.7 Effect of Power-Law Index $n$

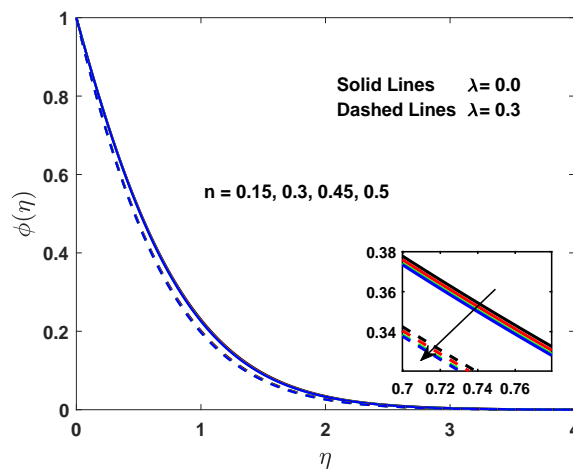
Figs. 5.5(a)-(c) are captured to disclose the outcome of the flow fields due to the power-law index  $n$ . The dimensionless velocity profile is heightened for the uprising values of  $n$  while the energy and the concentration fields are diminished. It is due



(a)



(b)

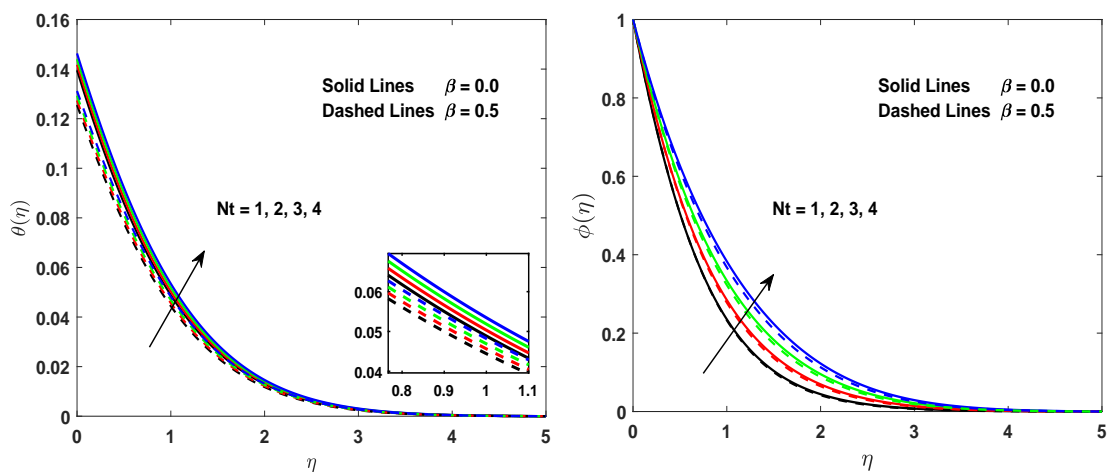


(c)

**Fig. 5.5:** Impact of  $n$  on (a) velocity, (b) temperature and (c) concentration profile.

to the reason that the wedge is convectively heated, therefore the fluid will lose more heat and hence the thermal and the concentration fields are declined.

### 5.4.8 Effect of Thermophoresis Parameter $Nt$



(a)

(b)

**Fig. 5.6:** Impact of  $Nt$  on (a) temperature and (b) concentration profile.

In the boundary layer region, the thermophoresis parameter  $Nt$  has a substantial impact on thermal and concentration profiles. Figs. 5.6(a)-(b) are chalked

out to present the effect of the thermophoresis parameter on energy and concentration profiles respectively. As demonstrated in these figures, both thermal and concentration fields are hiked for the enhancing values of  $Nt$ . Physically, in thermophoresis the particles apply a force on the other particles due to which the particles move towards the lower temperature region. Therefore, an increment in  $Nt$  means more application of the force on the other particles due to which more fluid moves from the hotter region to the colder region. Due to this reason the thermal profile and the nanoparticles concentration is intensified.

#### 5.4.9 Effect of Brownian Motion Parameter $Nb$

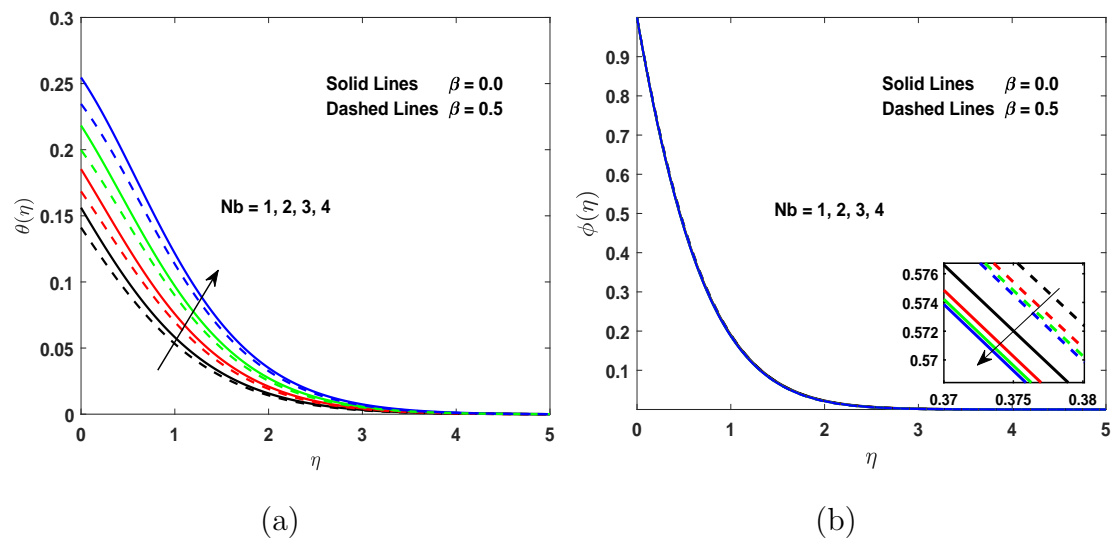


**Fig. 5.7:** Impact of  $Nb$  on (a) temperature and (b) concentration profile.

The variations in the flow fields due to the Brownian motion parameter  $Nb$ , can be visualized in Figs. 5.7(a)-(b). Fig. 5.7(a) clearly reflects that the temperature is amplified as  $Nb$  is enhanced. An increment in the Brownian motion results an increment in the motion of the small particles inside the flow region. This enhanced chaotic movement intensifies the velocity of the particles, which causes the increment in the kinetic energy, due to which the temperature is increased. However, a depreciation in the concentration field is observed, which is evident from the figure 5.7(b).

### 5.4.10 Effect of Thermal Radiation Parameter $Rd$

Figs. 5.8(a)-(b) are delineated to visualize the impact of the thermal radiation parameter  $Rd$  on the thermal and concentration fields. The temperature field is upsurged for the growing values of  $Rd$  as shown in Fig. 5.8(a). The curves in this figure reflect that a boost in  $Rd$  enhances the energy profile. Physically, it strengthens the fact that more heat is generated due to the radiation process for which the radiation parameter is increased. Fig. 5.8(b) represents a decreasing behaviour in the concentration profile as  $Rd$  is intensified.

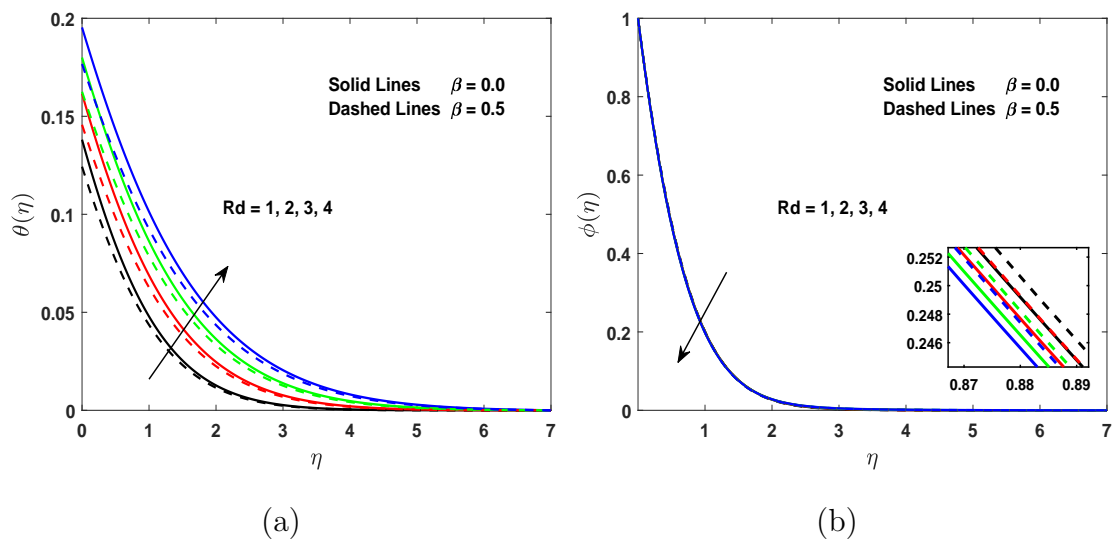


**Fig. 5.8:** Impact of  $Rd$  on (a) temperature and (b) concentration profile.

### 5.4.11 Effect of Generalized Biot Number $\gamma$

Figs. 5.9(a)-(b) are divulged to study the generalized Biot number's effect on temperature and concentration profiles. Generalized Biot number is the ratio between conductive heat transfer resistance inside the object to the convective heat transfer resistance at the surface. Smaller values of the Biot number  $\gamma (< 1)$  means that heat transfer due to convection is dominating as compare to the conduction and heat will transfer from the sheet to the fluid. As convection is dominating therefore more molecules will move from hotter region to colder region due to which both temperature and concentration profiles are escalated.

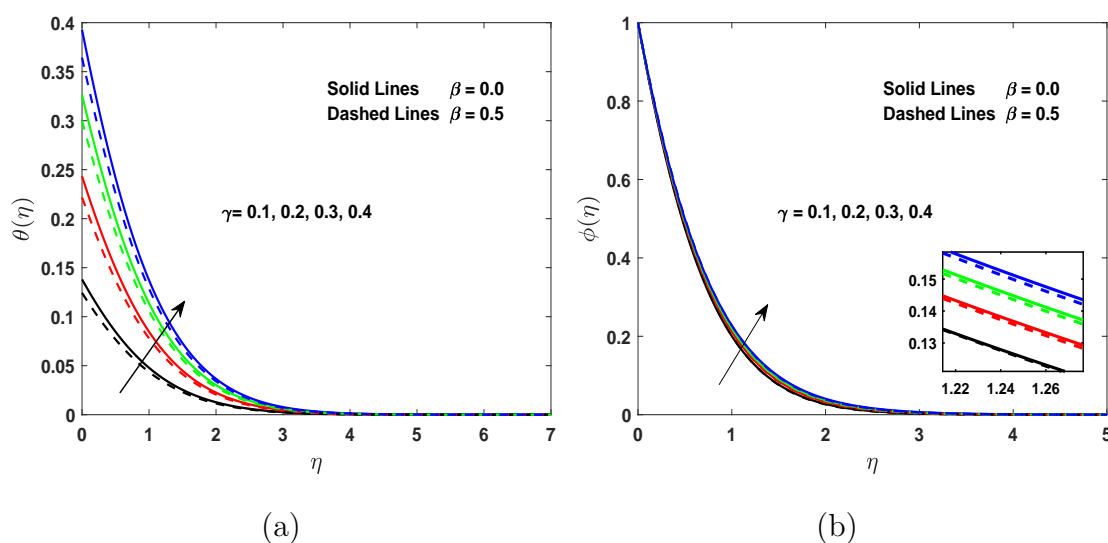


Fig. 5.9: Impact of  $\gamma$  on (a) temperature and (b) concentration profile.

## 5.5 Conclusions

Two dimensional magnetohydrodynamic tangent hyperbolic fluid flow past a static and stretching wedge in the presence of nanoparticles has been inspected. In this chapter, features of the dimensionless flow fields affected by various pertinent parameters are investigated in detail. Some of the key findings are:

- The velocity distribution is amplified for the large value of unsteadiness parameter  $A$  in both static and the stretching wedge case.
- An enhancement in the thermal profile is noticed for the enhancement in each of the Weissenberg number  $We$  and the generalized Biot number  $\gamma$ .
- A decrement in the concentration distribution is observed for gradually mounting values of each of the thermal radiation parameter  $Rd$ , the magnetic parameter  $M$ , the Brownian motion parameter  $Nb$  and the unsteadiness parameter  $A$  whereas opposite trends are noticed for the Weissenberg number  $We$  and the generalized Biot number  $\gamma$ .
- The Nusselt and Sherwood numbers are diminished for the increasing values of the Hartree pressure gradient  $\beta$ .

## Chapter 6

# MHD Stratified Bioconvective Flow of Micropolar Nanofluid due to Gyrotactic Micro-Organisms

The aim of this chapter is to analyze the flow of magnetohydrodynamic (MHD) stratified micropolar bioconvective fluid containing nanoparticles and gyrotactic micro-organism. Ohmic heating and linear thermal radiation effects have also been incorporated. The phenomenon of bioconvection is used to stabilize the suspended nanoparticles. There is wide usage of micro-organism in industry to produce fertilizers, ethanol, production of the biofuel from waste, promising renewable power source and so on. They are additionally utilized in water treatment plants. Hydrogen gas and biodiesel, promising renewable power source, are created by those micro-organisms [71–77]. The bioconvection phenomenon is established by using the combination of magnetic and buoyancy force effects. Governing set of PDEs are remodeled into the ODEs by invoking the appropriate similarity transformation. The solution of the system of nonlinear ODEs is achieved by shooting technique. The interesting aspects of sundry physical parameters on the axial and angular velocities, temperature, concentration and micro-organism density distributions are sketched and examined in detail.



## 6.1 Problem Formulation

Unsteady magnetohydrodynamic micropolar nanofluid with mixed convection past a vertically stretching surface has been analyzed. Stratification, Ohmic heating and thermal radiation effects have also been incorporated. The micro-organisms are induced to stabilize the nanoparticles. Direction of swimming and velocity of these micro-organisms is not affected by the nanoparticles. The sheet is positioned along  $x$  – axis having stretching velocity  $\tilde{u} = ax$  and  $y$  – axis is normal to the sheet. The flow is confined in positive  $y$  – axis region. In the positive  $y$  direction, a magnetic field  $B_0$  is implemented as displayed in Fig. 6.1.

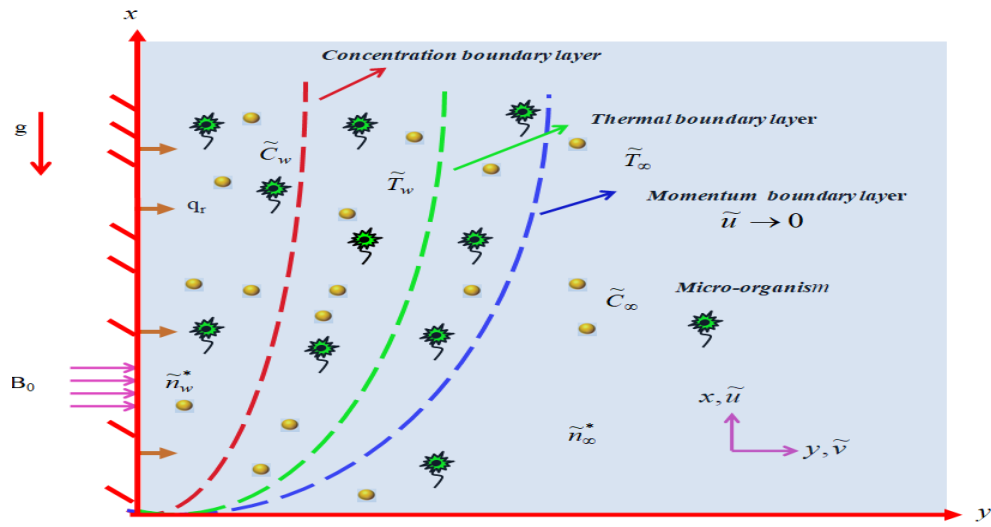


**Fig. 6.1:** Schematic illustration of the physical problem.

Subject to above mentioned constraints, the governing set of equations are expressed as follows:

$$\frac{\partial \tilde{u}}{\partial x} + \frac{\partial \tilde{v}}{\partial y} = 0, \quad (6.1)$$

$$\begin{aligned} \tilde{u} \frac{\partial \tilde{u}}{\partial x} + \tilde{v} \frac{\partial \tilde{u}}{\partial y} = & \left( \nu + \frac{k^*}{\rho} \right) \frac{\partial^2 \tilde{u}}{\partial y^2} + \frac{k^*}{\rho} \frac{\partial \tilde{N}}{\partial y} + \frac{1}{\rho} \left[ (1 - \tilde{C}_f) \rho \beta^* g (\tilde{T} - \tilde{T}_\infty) \right. \\ & \left. - g (\rho_p - \rho) (\tilde{C} - \tilde{C}_f) - \gamma^* g (\tilde{n}^* - \tilde{n}_\infty^*) (\rho_m - \rho) \right] - \frac{1}{\rho} \sigma B_0^2 \tilde{u}, \end{aligned} \quad (6.2)$$

$$\tilde{u} \frac{\partial \tilde{N}}{\partial x} + \tilde{v} \frac{\partial \tilde{N}}{\partial y} = \frac{\gamma_1}{(\rho j)} \frac{\partial^2 \tilde{N}}{\partial y^2} - \frac{k^*}{(\rho j)} \left( 2\tilde{N} + \frac{\partial \tilde{u}}{\partial y} \right), \quad (6.3)$$

$$\begin{aligned} \tilde{u} \frac{\partial \tilde{T}}{\partial x} + \tilde{v} \frac{\partial \tilde{T}}{\partial y} = \alpha \frac{\partial^2 \tilde{T}}{\partial y^2} + \frac{Q_0}{(\rho C_p)_f} (\tilde{T} - \tilde{T}_\infty) - \frac{1}{(\rho C_p)_f} \frac{\partial q_r}{\partial y} \\ + \frac{\sigma B_0^2}{(\rho C_p)_f} \tilde{u}^2 + \frac{(\rho C_p)_p}{(\rho C_p)_f} \left[ D_B \frac{\partial \tilde{C}}{\partial y} \frac{\partial \tilde{T}}{\partial y} + \frac{D_T}{\tilde{T}_\infty} \left( \frac{\partial \tilde{T}}{\partial y} \right)^2 \right], \end{aligned} \quad (6.4)$$

$$\tilde{u} \frac{\partial \tilde{C}}{\partial x} + \tilde{v} \frac{\partial \tilde{C}}{\partial y} = \frac{D_T}{\tilde{T}_\infty} \frac{\partial^2 \tilde{T}}{\partial y^2} + D_B \frac{\partial^2 \tilde{C}}{\partial y^2}, \quad (6.5)$$

$$\tilde{u} \frac{\partial \tilde{n}^*}{\partial x} + \tilde{v} \frac{\partial \tilde{n}^*}{\partial y} + \frac{b^* W_c}{\tilde{C}_w - \tilde{C}_0} \frac{\partial}{\partial y} \left( \tilde{n}^* \frac{\partial \tilde{C}}{\partial y} \right) = D_m \frac{\partial^2 \tilde{n}^*}{\partial y^2}. \quad (6.6)$$

The associated BCs are as follows:

$$\left. \begin{aligned} \tilde{u}_w = ax, \quad \tilde{v} = 0, \quad \tilde{N} = 0, \quad \tilde{T} = \tilde{T}_w = \tilde{T}_0 + b_1 x, \\ \tilde{C} = \tilde{C}_w = \tilde{C}_0 + d_1 x, \quad \tilde{n}^* = \tilde{n}_w^* = \tilde{n}_0^* + e_1 x \end{aligned} \right\} \quad \text{at} \quad y = 0, \quad (6.7)$$

$$\left. \begin{aligned} \tilde{u} \rightarrow 0, \quad \tilde{N} \rightarrow 0, \quad \tilde{T} = \tilde{T}_\infty = \tilde{T}_0 + b_2 x, \\ \tilde{C} = \tilde{C}_\infty = \tilde{C}_0 + d_2 x, \quad \tilde{n} = \tilde{n}_\infty^* = \tilde{n}_0^* + e_2 x \end{aligned} \right\} \quad \text{as} \quad y \rightarrow \infty.$$

Here  $\sigma$  represents the electrical conductivity,  $\beta^*$  the volume expansion coefficient,  $\alpha$  thermal diffusivity,  $\gamma^*$  average volume of micro-organism,  $g$  is the gravity,  $\rho_f$ ,  $\rho_p$  and  $\rho_m$  represents the nanofluid density, nanoparticles density and micro-organism particle density respectively. The reference temperature, concentrations of nanoparticles and micro-organisms are considered as  $\tilde{T}_0$ ,  $\tilde{C}_0$  and  $\tilde{n}_0^*$  respectively. The temperature at surface, concentrations of the nanoparticles and concentrations of the micro-organisms at surface are represented by  $\tilde{T}_w$ ,  $\tilde{C}_w$  and  $\tilde{n}_w^*$  respectively. The ambient temperature, ambient concentration of the nanoparticles and ambient concentration of the micro-organisms are denoted by  $\tilde{T}_\infty$ ,  $\tilde{C}_\infty$  and  $\tilde{n}_\infty^*$  respectively.  $\tilde{N}$  denotes the angular velocity,  $C_p$  the specific heat,  $b_1, b_2, d_1, d_2, e_1$  and  $e_2$  are the dimensionless constants.

In (6.3),  $\gamma_1$  denoted the spin gradient viscosity which is given by

$$\gamma_1 = \left( \mu + \frac{k^*}{2} \right) j,$$

here  $j = \nu/a$  and  $k^*$  represents the micro-inertia density and vortex viscosity respectively. Furthermore, in (4.3),  $q_r$  is the Rosseland radiative heat flux as defined in (3.7) of chapter 3. In Eq (6.6),  $D_m$  represents the diffusion coefficient of micro-organisms,  $\frac{b^*W_c}{\Delta\tilde{C}}\nabla\tilde{C}$  is the velocity related to cell swimming,  $b^*$  is the chemotaxis constant and  $W_c$  is the maximum swimming speed of cell.

By using the following transformation [25, 76], Eqs. (6.2)-(6.6) are transformed into the system of ODEs.

$$\left. \begin{aligned} \eta &= y\sqrt{\frac{a}{\nu}}, \quad \tilde{u} = axf'(\eta), \quad \tilde{v} = -f(\eta)\sqrt{a\nu}, \quad \tilde{N} = ax\sqrt{\frac{a}{\nu}}g(\eta), \\ \theta(\eta) &= \frac{\tilde{T} - \tilde{T}_\infty}{\tilde{T}_w - \tilde{T}_0}, \quad \phi(\eta) = \frac{\tilde{C} - \tilde{C}_\infty}{\tilde{C}_w - \tilde{C}_0}, \quad \xi(\eta) = \frac{\tilde{n}_w^* - \tilde{n}_0^*}{\tilde{n}_w^* - \tilde{n}_0^*}. \end{aligned} \right\} \quad (6.8)$$

As a result Eq. (6.1) is satisfied identically and Eqs. (6.2)-(6.6) yield

$$(1 + K)f''' - f'^2 + ff'' + Kg' - Mf' + \lambda(\theta - Nr\phi - Rb\epsilon) = 0, \quad (6.9)$$

$$\left(1 + \frac{K}{2}\right)g'' - gf' + fg' - K(2g + f'') = 0. \quad (6.10)$$

$$\left. \begin{aligned} \left(1 + \frac{4}{3}Rd\right)\theta'' + Prf\theta' - Prf'\theta - Prf'S + Pr\delta_1\theta + PrMEcf'^2 \\ + PrNb\theta'\phi' + PrNt\theta^2 = 0, \end{aligned} \right\} \quad (6.11)$$

$$\phi'' + Sc(f\phi' - f'\phi - Qf') + \frac{Nt}{Nb}\theta'' = 0. \quad (6.12)$$

$$\xi'' - Lb(f'\xi - f\xi' + Bf') - Pe(\phi''(\xi + \Omega) + \xi'\phi') = 0. \quad (6.13)$$

The associated BCs takes the form:

$$\left. \begin{aligned} f = 0, \quad f' = 1, \quad g = 0, \quad \theta = 1 - S, \quad \phi = 1 - Q, \quad \xi = 1 - B \text{ at } \eta = 0, \\ f' \rightarrow 0, \quad g \rightarrow 0, \quad \theta \rightarrow 0, \quad \phi \rightarrow 0, \quad \xi \rightarrow 0 \text{ as } \eta \rightarrow \infty. \end{aligned} \right\} \quad (6.14)$$

In the above equations,  $Pr$  represents the Prandtl number,  $Pe$  the bioconvection Peclet number,  $\lambda$  the mixed convection parameter,  $K$  the micropolar constant,  $Gr$

the Grashof number,  $Re_x$  the local Reynolds number,  $B$  the motile density stratification,  $Lb$  the bioconvection Lewis parameter,  $\Omega$  the micro-organism concentration difference parameter,  $Ec$  the Eckert number,  $S$  the thermal stratification parameter,  $M$  the magnetic number,  $Sc$  the Schmidt number,  $Nb$  the Brownian motion parameter,  $Rb$  the Rayleigh number,  $Q$  the mass stratification parameter,  $Nr$  the buoyancy ratio parameter,  $Rd$  the thermal radiation parameter,  $Nt$  the thermophoresis parameter and  $\delta_1$  is the heat generation coefficient. The formulation of these parameters is as follows:

$$\begin{aligned}
Pr &= \frac{\nu}{\alpha}, \quad Pe = \frac{b^*W_c}{D_m}, \quad \lambda = \frac{Gr}{Re_x^2}, \quad K = \frac{k^*}{\mu}, \quad Gr = \frac{\beta^*g(1 - \tilde{C}_\infty)(\tilde{T}_w - \tilde{T}_0)x^3}{\nu^2}, \\
Re_x &= \frac{ax^2}{\nu}, \quad B = \frac{e_2}{e_1}, \quad Lb = \frac{\nu}{D_m}, \quad \Omega = \frac{\tilde{n}_\infty^*}{\tilde{n}_w^* - \tilde{n}_0^*}, \quad Ec = \frac{a^2x^2}{(C_p)_f(\tilde{T}_w - \tilde{T}_0)}, \quad S = \frac{b_2}{b_1}, \\
M &= \frac{\sigma B_0^2}{a\rho}, \quad Sc = \frac{\nu}{D_B}, \quad Nb = \frac{(\rho C_p)_p D_B (\tilde{C}_w - \tilde{C}_\infty)}{(\rho C_p)_f \nu}, \quad Rb = \frac{\gamma^*(\tilde{n}_w^* - \tilde{n}_0^*)(\rho_m - \rho)}{\beta^*\rho(1 - \tilde{C}_\infty)(\tilde{T}_w - \tilde{T}_0)}, \\
Q &= \frac{d_2}{d_1}, \quad Nr = \frac{(\rho_p - \rho)(\tilde{C}_w - \tilde{C}_0)}{\beta^*(1 - \tilde{C}_\infty)\rho(\tilde{T}_w - \tilde{T}_0)}, \quad Rd = \frac{4\sigma^*\tilde{T}_\infty^3}{3k\kappa^*}, \quad Nt = \frac{(\rho C_p)_p D_T (\tilde{T}_w - \tilde{T}_\infty)}{(\rho C_p)_f \tilde{T}_\infty \nu_f}, \\
\delta_1 &= \frac{Q_0}{a(\rho C_p)_f}.
\end{aligned}$$

### 6.1.1 Quantities of Interest

The quantities which play vital role in engineering and industrial applications are the skin friction coefficient, the local Nusselt number, the local Sherwood number and the local density number. These dimensionless parameters are defined as:

$$\begin{aligned}
C_f &= \frac{\tau_w}{\rho_f \tilde{u}_w^2}, & Nu_x &= \frac{xq_w}{k(\tilde{T}_w - \tilde{T}_0)}, \\
Sh_x &= \frac{xq_m}{D_B(\tilde{C}_w - \tilde{C}_0)}, & Nn_x &= \frac{xq_n}{D_n(\tilde{n}_w^* - \tilde{n}_0^*)}.
\end{aligned}$$

For this problem, the quantities  $\tau_w$ ,  $q_w$ ,  $q_m$  and  $q_n$  are wall shear stress, wall heat flux, wall mass flux and motile micro-organism flux and defined as

$$\tau_w = \mu \left[ (1 + K) \frac{\partial \tilde{u}}{\partial y} \right]_{y=0}, \quad q_m = -D_B \left( \frac{\partial \tilde{C}}{\partial y} \right)_{y=0},$$

$$q_w = -k \left[ \left( 1 + \frac{16\sigma^* \tilde{T}_\infty}{3k\kappa^*} \right) \frac{\partial \tilde{T}}{\partial y} \right]_{y=0}, \quad q_n = -D_n \left( \frac{\partial \tilde{n}^*}{\partial y} \right)_{y=0}.$$

In dimensionless form

$$\left. \begin{aligned} C_f Re_x^{1/2} &= (1 + K) f''(0), & Sh_x Re_x^{-1/2} &= -\phi'(0), \\ Nu_x Re_x^{-1/2} &= - \left( 1 + \frac{4}{3} Rd \right) \theta'(0), & Nn_x Re_x^{-1/2} &= -\xi'(0), \end{aligned} \right\} \quad (6.15)$$

## 6.2 Implementation of the Numerical Scheme

The system of ODEs (6.9)-(6.13) along with BCs (6.14) is solved numerically by utilizing the shooting technique [92]. A system of first order ODEs is required for the implementation of shooting technique. For this purpose we introduce the new variables,  $f = \zeta_1$ ,  $f' = \zeta_2$ ,  $f'' = \zeta_3$ ,  $g = \zeta_4$ ,  $g' = \zeta_5$ ,  $\theta = \zeta_6$ ,  $\theta' = \zeta_7$ ,  $\phi = \zeta_8$ ,  $\phi' = \zeta_9$ ,  $\xi = \zeta_{10}$  and  $\xi' = \zeta_{11}$  to have the following set of eleven first order ODEs:

$$\left. \begin{aligned} \zeta_1' &= \zeta_2, \\ \zeta_2' &= \zeta_3, \\ \zeta_3' &= \frac{1}{1 + K} \left[ \zeta_2^2 - \zeta_1 \zeta_3 - K \zeta_5 + M \zeta_2 - \lambda^* (\zeta_6 - Nr \zeta_8 - Rb \zeta_{10}) \right], \\ \zeta_4' &= \zeta_5, \\ \zeta_5' &= \frac{2}{2 + K} \left[ \zeta_2 \zeta_4 - \zeta_1 \zeta_5 + K (2\zeta_4 + \zeta_3) \right], \\ \zeta_6' &= \zeta_7, \\ \zeta_7' &= \frac{3Pr}{3 + 4Rd} \left[ \zeta_2 \zeta_6 - \zeta_1 \zeta_7 + S \zeta_2 - \delta_1 \zeta_6 - MEc \zeta_2^2 \right. \\ &\quad \left. - Nb \zeta_7 \zeta_9 - Nt \zeta_7^2 \right], \\ \zeta_8' &= \zeta_9, \\ \zeta_9' &= Sc (\zeta_2 \zeta_8 - \zeta_1 \zeta_9 + Q \zeta_2) - \frac{Nt}{Nb} \zeta_7', \\ \zeta_{10}' &= \zeta_{11}, \\ \zeta_{11}' &= Lb (\zeta_2 \zeta_{10} - \zeta_1 \zeta_{11} + B \zeta_2) + Pe (y_9' (\zeta_{10} + \Omega) + \zeta_{11} \zeta_9). \end{aligned} \right\} \quad (6.16)$$

The associated BCs are as follows:

$$\left. \begin{aligned} \zeta_1 = 0, \quad \zeta_2 = 1, \quad \zeta_4 = 0, \quad \zeta_6 = 1 - S, \\ \zeta_8 = 1 - Q, \quad \zeta_{10} = 1 - B, \\ \zeta_2 \rightarrow 0, \quad \zeta_4 \rightarrow 0, \quad \zeta_6 \rightarrow 0, \quad \zeta_8 \rightarrow 0, \quad \zeta_{10} \rightarrow 0 \end{aligned} \right\} \begin{array}{l} \text{at } \eta = 0 \\ \text{as } \eta \rightarrow \infty. \end{array} \quad (6.17)$$

To find the solutions of the system of ODEs (6.16), with the assistance of the shooting method, eleven initial conditions are required. Therefore, we guess five missing initial conditions  $\zeta_3(0) = s_1, \zeta_5(0) = s_2, \zeta_7(0) = s_3, \zeta_9(0) = s_4, \zeta_{11} = s_5$  and  $s_1, s_2, s_3, s_4$  and  $s_5$  are chosen arbitrarily. The Newton’s iterative scheme is applied to improve the accuracy of  $s_1, s_2, s_3, s_4$  and  $s_5$  until the desired approximation is met. Simulations have been performed for the various emerging parameters and for the appropriate bounded domain  $[0, \eta_{max}]$  instead of  $[0, \infty)$ , where the positive real number  $\eta_{max}$  is chosen in such that no significant variations appeared in the results for the values greater than  $\eta_{max}$ . The process will continued till the following criteria is met.

$$\max\{|\zeta_2(\eta_{max}) - 0|, |\zeta_4(\eta_{max}) - 0|, |\zeta_6(\eta_{max}) - 0|, |\zeta_8(\eta_{max}) - 0|, |\zeta_{10}(\eta_{max}) - 0|\} < 10^{-6}.$$

### 6.2.1 Validation of Code

For the reliability and validation of the MATLAB code, the results for  $-f''(0)$  and  $g'(0)$ , which were reported by Eldabe [22] and Hsiao [25], are successfully reproduced.

		$-f''(0)$			$g'(0)$		
$M$	$K$	[22]	[25]	Present	[22]	[25]	Present
0.0	0.2	0.9098	0.90976	0.909737	0.0950	0.09500	0.094997
	0.5	1.1148	1.11437	1.114376	0.1051	0.10509	0.105090
	1.0	1.2871	1.28711	1.287152	0.1121	0.11212	0.112061
	0	1.4142	1.41423	1.414216	0	0	0
	0.5	1.1408	1.14073	1.140786	0.2112	0.21116	0.211162
	2	0.7697	0.76958	0.769757	0.3586	0.35855	0.358664

Table 6.1: Comparison of the presently computed values of  $-f''(0)$  and  $g'(0)$  with those of Eldabe [22] and Hsiao [25].

### 6.3 Results and Discussion

The fluctuation in the skin friction, microrotation parameter, Nusselt number, Sherwood number and density number due to the assorted parameter have been computed and discussed in detail in this section. Moreover the effect of different governing parameters on velocity, angular velocity, temperature, mass and density profile has been displayed graphically and discussed in detail.

#### 6.3.1 The Skin Friction Coefficient and the Microrotation Parameter

Table 6.2 has been displayed to view the behaviour of the skin friction and microrotation parameter due to assorted parameter. It is observed that for gradually boosting values of the material parameter  $K$ , the buoyancy ratio parameter  $Nr$ , the magnetic number  $M$  and the bioconvection Rayleigh number  $Rb$  both the

$K$	$M$	$\lambda^*$	$Nr$	$Rb$	$-C_f Re_x^{1/2}$	$g'(0)$
0.2	0.05	0.1	0.1	0.1	1.0736	0.1032
0.5					1.1926	0.2180
2					1.6197	0.5749
0.2	0				1.0468	0.1020
	0.5				1.2930	0.1128
	1				1.5025	0.1207
	0.05	0.1			1.0736	0.1032
		0.2			1.0302	0.1009
		0.3			0.9883	0.0988
		0.1	0.2		1.0845	0.1042
			0.4		1.1024	0.1056
			0.6		1.1204	0.1071
			0.1	0.2	1.0795	0.1036
				0.4	1.0870	0.1038
				0.6	1.0946	0.1041

Table 6.2: Variation in the  $C_f Re_x^{1/2}$  and  $g'(0)$  parameter for different parameters when  $S = Q = B = \delta_1 = Nb = Nt = 0.1$ ,  $\Omega = Sc = 0.2$ ,  $Ec = 0.02$ ,  $Pr = Pe = Lb = 1.2$ .

microrotation parameter and the skin friction coefficient are upsurged whereas both are diminished for an increment in the mixed convection parameter  $\lambda^*$ .

### 6.3.2 The Nusselt Number

Table 6.3 is presented to study the impact of prominent physical parameters on the Nusselt number. It is noticed that due to an acclivity in each of the mass stratification parameter  $Q$ , the Prandtl number  $Pr$ , the thermal radiation  $Rd$  and the material parameter  $K$ , the Nusselt number is enhanced. When the Prandtl number  $Pr$  is increased the thermal boundary thickness becomes thin and allows more heat to flow due to which heat transfer rate at the surface is enhanced. With an increment in the material parameter  $K$  means an increment in the viscosity of the fluid due to which the temperature difference between the surface and the sheet is declined which causes more heat to flow. The rate of heat transfer is declined as each of the thermal stratification  $S$ , the magnetic parameter  $M$ , the thermophoresis parameter  $Nt$ , the heat generation coefficient  $\delta_1$ , the Eckert number  $Ec$  and the Brownian motion parameter  $Nb$  is enhanced. The Eckert number  $Ec$  measures the viscous dissipation effect. Greater the value of  $Ec$  means more heat is produced inside the fluid due to viscous effects which causes the rate of heat transfer to decline. By increasing Brownian motion parameter  $Nb$ , the thermal diffusivity decreases due to which the thermal boundary layer thickness increases which causes the Nusselt number to decrease. The effect of thermophoresis  $Nt$  is similar to that of  $Nb$ . An increment in the thermophoresis  $Nt$  causes more application of the thermophoretic force on the other particles and more particles move from one place to the other place due to which the temperature difference is declined as a result the rate of heat transfer at the surface is also declined. Due to an increment in the magnetic parameter  $M$ , the Lorentz force is enhanced and the wall temperature gradient of the fluid is declined which causes a decrement in the rate of heat transfer at the surface. The local heat flux is declined as the heat generation coefficient  $\delta_1$  is increased. It is due to the fact that the heat generation



coefficient enhances the temperature of the fluid due to which a decline in the heat rate transfer is obvious.

$K$	$M$	$Pr$	$Rd$	$S$	$\delta_1$	$Ec$	$Nt$	$Nb$	$Q$	$Nu_x Re_x^{-1/2}$
0.2	0.05	1.2	1	0.1	0.1	0.02	0.1	0.1	0.1	1.3804
	0.5									1.4285
	2									1.5595
0.2	0									1.3934
	0.5									1.2765
	1									1.1836
	0.05	2								1.9114
		5								3.3285
		7								4.0218
		1.2	2							1.6409
			3							1.8720
			4							2.0910
			1	0.2						1.3266
				0.3						1.2724
				0.4						1.2177
				0.1	0.2					1.2666
					0.3					1.1351
					0.4					0.9780
					0.1	0.2				1.3756
						0.3				1.3730
						0.4				1.3704
						0.02	0.2			1.3647
							0.4			1.3337
							0.6			1.3032
							0.1	0.2		1.3656
								0.4		1.3336
								0.6		1.3016
								0.1	0.2	1.3825
									0.4	1.3867
									0.6	1.3908

Table 6.3: Variation in  $Nu_x Re_x^{-1/2}$  for various parameters when  $\Omega = Sc = 0.2$ ,  $Pe = Lb = 1.2$ ,  $\lambda^* = Nr = B = Rb = 0.1$ .

### 6.3.3 The Sherwood Number

The objective of the Table 6.4 is to observe the influence of sundry parameters on the Sherwood number. From this table it is observed that accelerating each of the heat generation coefficient  $\delta_1$ , the thermal stratification parameter  $S$ , the Eckert number  $Ec$ , the Brownian motion parameter  $Nb$  and the Schmidt number  $Sc$  cause an enhancement in the Sherwood number whereas opposite trend is noticed for the mass stratification parameter  $Q$  and the thermophoresis parameter  $Nt$ .

$S$	$\delta_1$	$Ec$	$Sc$	$Nt$	$Nb$	$Q$	$Sh_x Re_x^{-1/2}$
0.1	0.1	0.02	0.2	0.1	0.1	0.1	-0.1501
0.2							-0.1383
0.3							-0.1275
0.1	0.1						-0.1501
	0.2						-0.0768
	0.3						0.0239
	0.1	0.3					-0.1471
		0.4					-0.1460
		0.5					-0.1449
		0.02	0.3				0.0029
			0.4				0.1328
			0.5				0.2460
			0.2	0.3			-1.0517
				0.5			-1.8608
				0.7			-2.5954
				0.1	0.2		0.0903
					0.3		0.2114
					0.4		0.2357
					0.1	0.3	-0.1816
						0.5	-0.2130
						0.7	-0.2440

Table 6.4: Variation in  $Sh_x Re_x^{-1/2}$  for various parameters when  $\Omega = K = 0.2$ ,  $Pe = Pr = Lb = 1.2$ ,  $Rd = 1$ ,  $M = 0.05$ ,  $B = Rb = Nr = \lambda^* = 0.1$ .

### 6.3.4 The Density Number

Table 6.5 has been prepared to portray the effect of the physical parameters on density number. The results show that the density number is enhanced as each

of the buoyancy ratio parameter  $Nr$ , the Eckert number  $Ec$ , the bioconvection Lewis number  $Lb$  and the Schmidt number  $Sc$  is hiked whereas reverse situation is observed in case of motile density stratification  $B$ , the concentration difference parameter of micro-organism  $\Omega$ , the Peclet number  $Pe$  and the Rayleigh number  $Rb$ .

$Nr$	$Rb$	$Ec$	$Sc$	$Lb$	$B$	$Pe$	$\Omega$	$Nn_xRe_x^{-1/2}$
0.2	0.1	0.02	0.2	1.2	0.1	1.2	0.2	0.9509
								0.9560
								0.9634
	0.2							0.9520
	0.4							0.9512
	0.6							0.9503
	0.1	0.2						0.9541
		0.4						0.9564
		0.6						0.9587
		0.02	0.4					1.2086
			0.6					1.4164
			0.8					1.5957
			0.2	1				0.8306
				2				1.3561
				3				1.7573
				1.2	0.2			0.9256
					0.3			0.8991
					0.4			0.8725
					0.1	2		0.8489
						3		0.7213
						4		0.5950
						1.2	0.4	0.9235
							0.6	0.8949
							0.8	0.8663

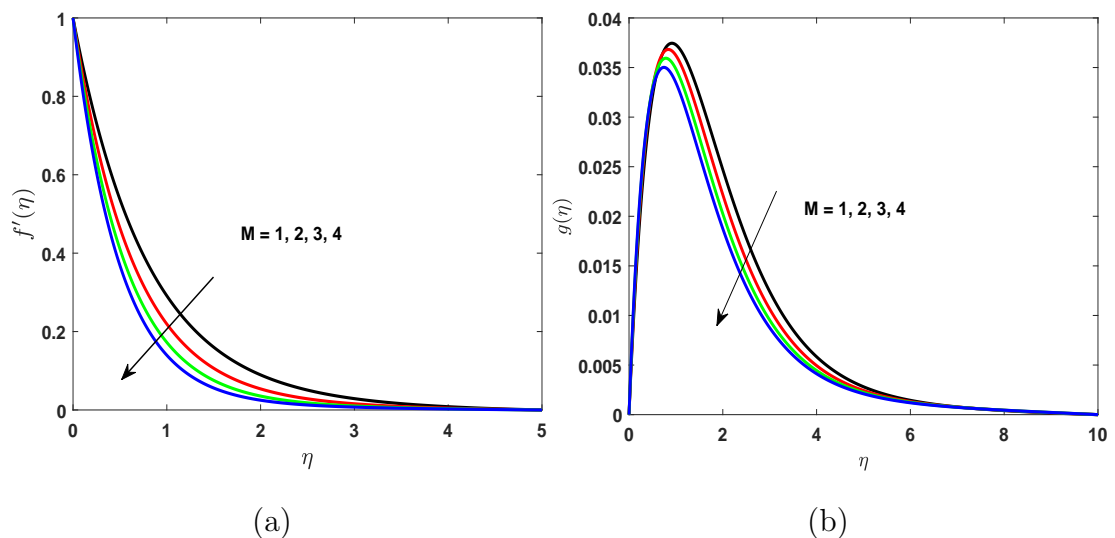
Table 6.5: Variation in  $Nn_xRe_x^{-1/2}$  for various parameters when  $Pr = 1.2$ ,  $\lambda^* = Nt = \delta_1 = Nb = 0.1$ ,  $Rd = 1$ ,  $M = 0.05$ ,  $K = 0.2$ .

In the subsequent section, the fluctuations in the axial velocity, angular velocity, temperature, concentration and motile density fields due to the pertinent parameters has been presented graphically and discussed in detail. In order to execute the

numerical simulations, the non-dimensional parameters are assigned fixed values as  $K = \Omega = 0.2$ ,  $Rb = S = \lambda^* = Nb = \delta_1 = B = Nr = Nt = Q = 0.1$ ,  $Sc = Rd = M = 1$ ,  $Lb = Pe = Pr = 1.2$  and  $Ec = 0.02$ . For the whole investigation, the varying parameter is presented in the respective figure and all other parameters are kept constant.

### 6.3.5 Effect of Magnetic Number $M$

Figs. 6.2(a)-(d) are sketched to visualize the variation in the flow fields due to changes in the magnetic number  $M$ . From Fig. 6.2(a) it is noticed that a small amplification in the magnetic number  $M$  causes slowness in the motion of the fluid. This verifies the general behavior of the magnetic effect in stretching sheet. The velocity field decreases because the drag force is enhanced for the gradually mounting values of  $M$ . As a result the resistance is increased, due to which the velocity is declined. Fig. 6.2(b) is displayed to scrutinize the impact of  $M$  on the angular velocity  $g(\eta)$ . The dimensionless angular velocity is declined when  $M$  is raised. An increment in the magnitude of the opposing force also leads the temperature field to enhance as displayed in Fig. 6.2(c). The aim of the Fig. 6.2(d) is to analyze the motile density profile for an increasing values of magnetic number  $M$ . These curves reflect that an increment in  $M$  results an enhancement in the density profile.



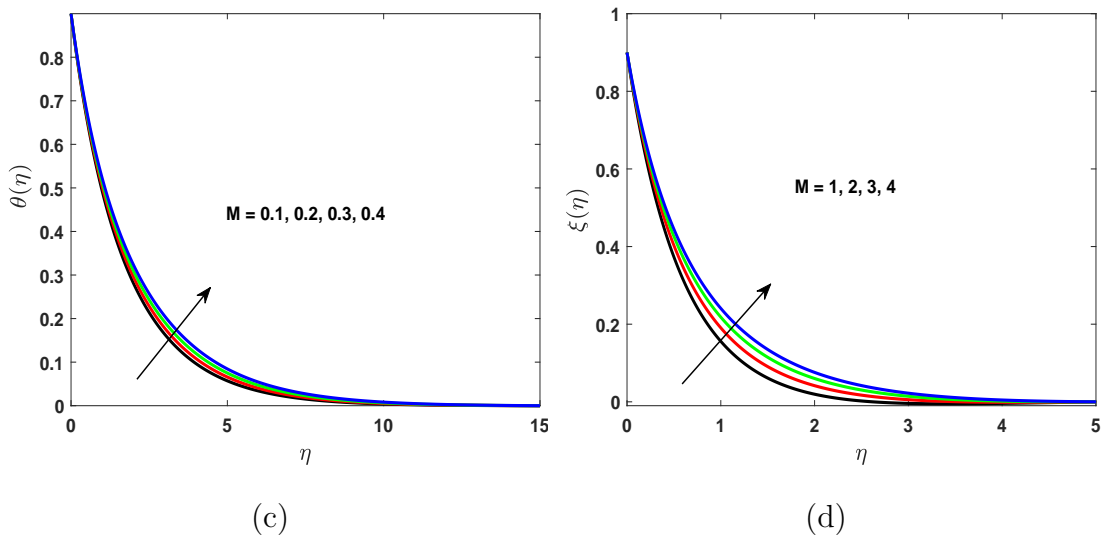
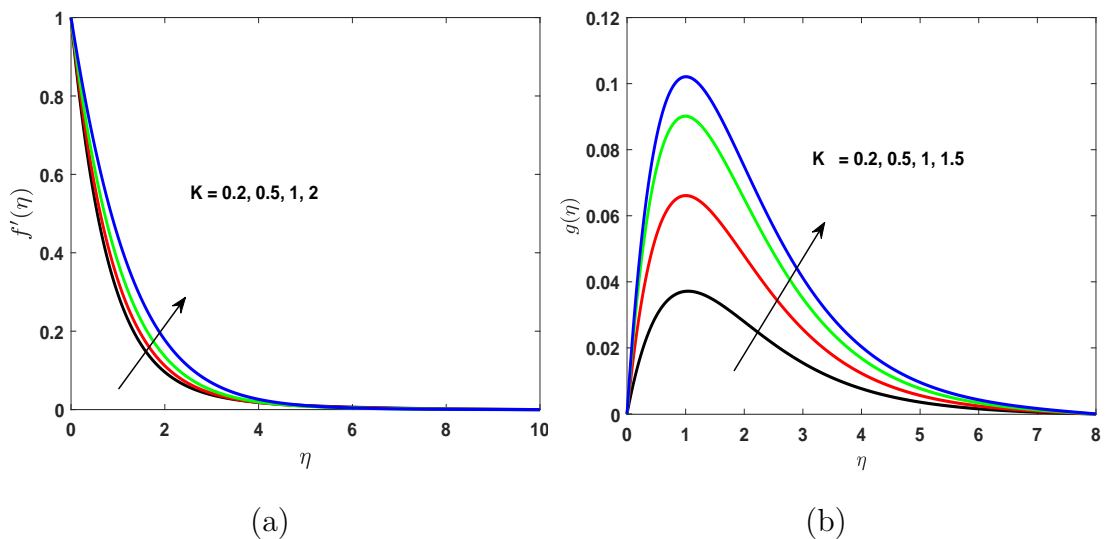
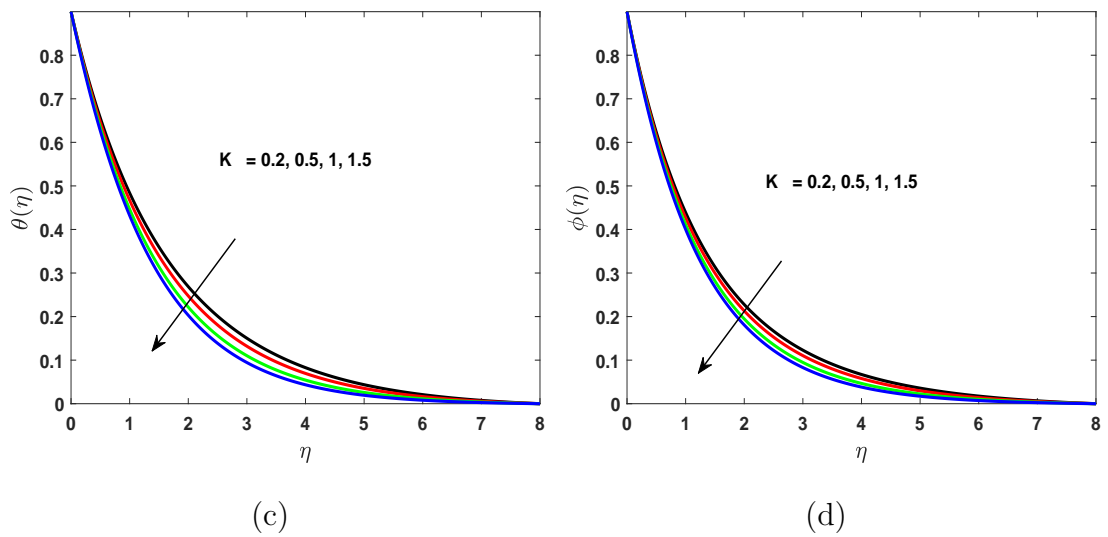


Fig. 6.2: Impact of  $M$  on (a) velocity, (b) angular velocity, (c) temperature and (d) motile density profile.

### 6.3.6 Effect of Material Parameter $K$

Figs. 6.3(a)-(d) are divulged to study the changes in axial velocity, angular velocity, thermal and concentration fields due to changes in the material parameter  $K$ . Fig. 6.3(a) shows that the fluid velocity is hiked for growing values of the material parameter  $K$ . Fig. 6.3(b) is presented to study the impact of  $K$  on the angular velocity. These curves reflect that the angular velocity is boosted for the acceleration in  $K$ . Physically, an acclivity in the material parameter  $K$  results an

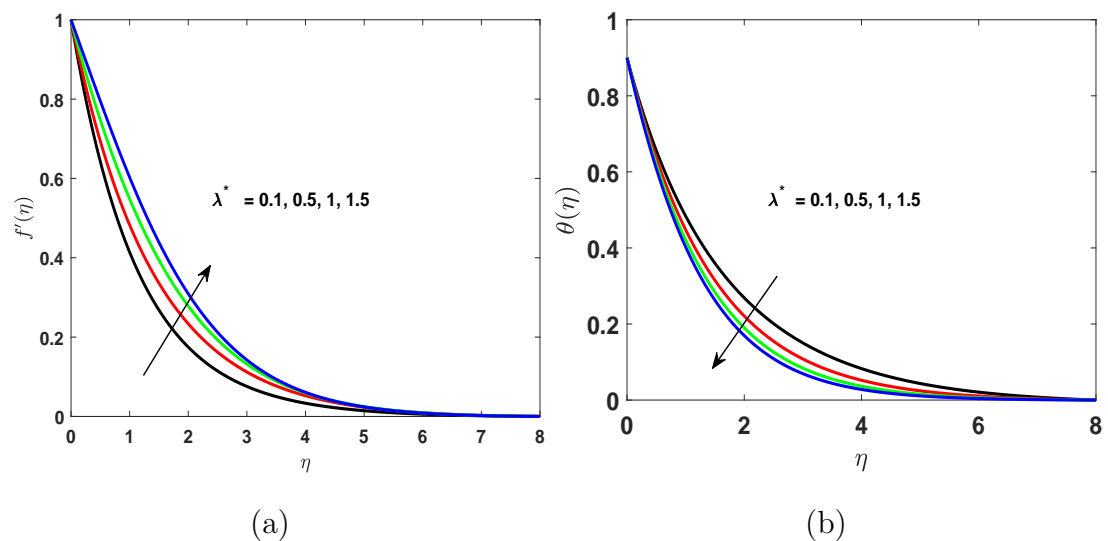




**Fig. 6.3:** Impact of  $K$  on (a) velocity, (b) angular velocity, (c) temperature and (d) concentration profile.

enhancement in the viscosity of the fluid, due to which the angular velocity of the fluid is upsurged. Figs. 6.3(c)-(d) are disseminated to visualize the effect of the material parameter  $K$  on dimensionless temperature and concentration fields respectively. It is noticed that increasing the values of the dimensionless angular velocity  $K$  causes a decline in both dimensionless temperature and concentration profiles.

### 6.3.7 Effect of Mix Convection Parameter $\lambda^*$



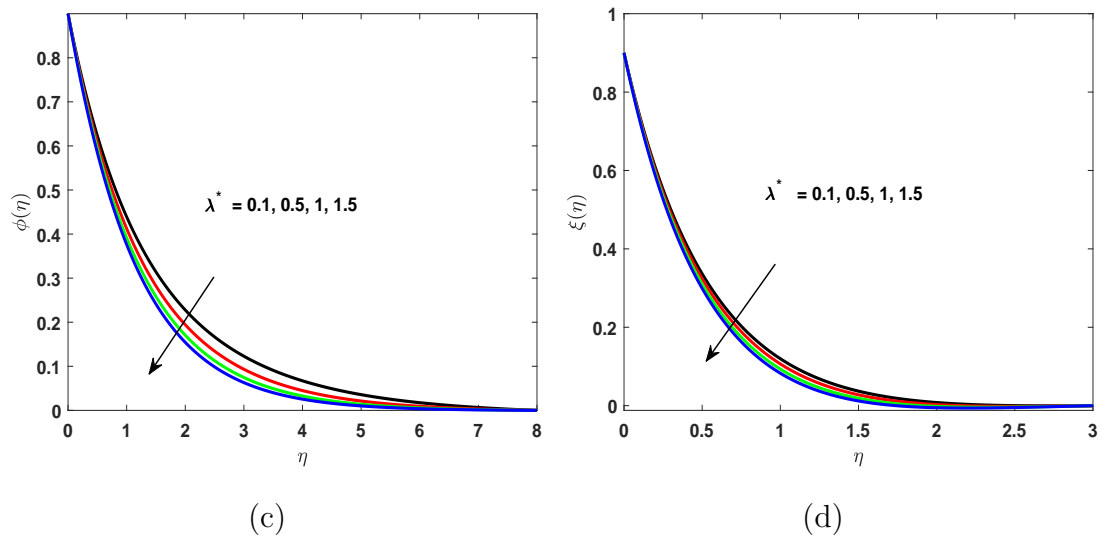


**Fig. 6.4:** Impact of  $\lambda^*$  on (a) velocity, (b) temperature, (c) concentration and (d) motile density profile.

Figs. 6.4(a)-(d) are sketched to visualize the variation in the flow fields due to variation in the mix convection parameter  $\lambda^*$ . Fig. 6.4(a) reflects that an enhancement in the mix convection parameter  $\lambda^*$  results an increment in the fluid motion which is due to increment in the buoyancy force, while the thermal and concentration profiles are diminished, which is evident from the Figs. 6.4(b)-(c). The effect of  $\lambda^*$  on the motile density distribution  $\xi(\eta)$  is delineated in the Fig. 6.4(d). The motile density profile  $\xi(\eta)$  is a decreasing function of  $\lambda^*$ .

### 6.3.8 Effect of Buoyancy Ratio Parameter $Nr$

Figs. 6.5(a)-(d) are sketched to analyze of the buoyancy ratio parameter  $Nr$  on the fluid motion, concentration, temperature and motile density distributions. The dimensionless velocity profile is declined as  $Nr$  is increased. Fig. 6.5(a) indicates the influence of  $Nr$  on energy profile. From these curves it is clear that an increment in  $Nr$  enhances the temperature. Fig. 6.5(d) is plotted to visualize the variation in motile density profile due to the buoyancy ratio parameter  $Nr$ . An increment in  $Nr$  increases the motile density profile  $\xi(\eta)$ . Solutal buoyancy force is increased due to an increment in  $Nr$  which causes an enhancement in the density of the fluid.

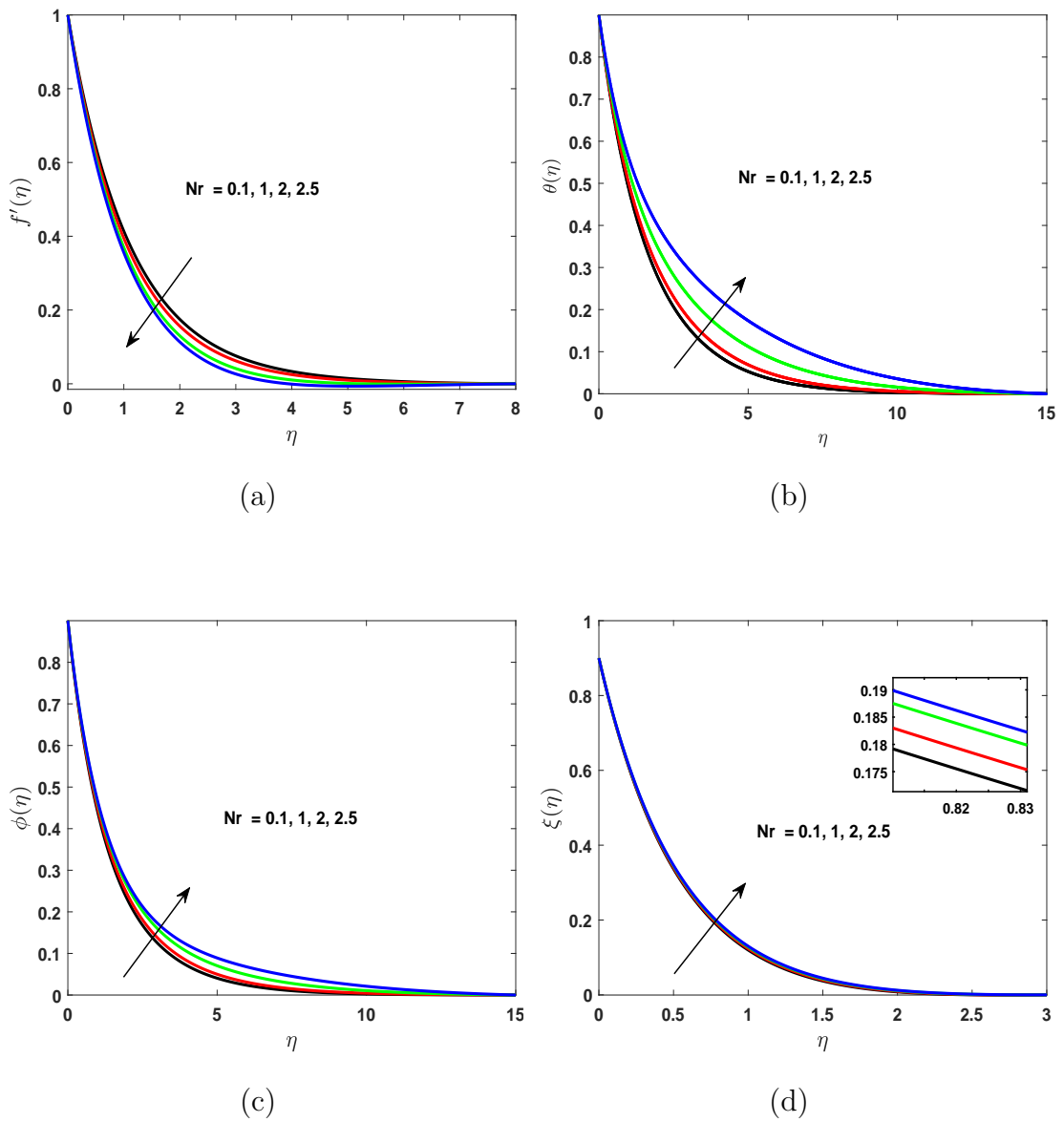


**Fig. 6.5:** Impact of  $Nr$  on (a) velocity, (b) temperature, (c) concentration and (d) motile density profile.

### 6.3.9 Effect of Thermal Stratification Parameter $S$

The effect on fluid velocity, energy and concentration distributions due to change in the thermal stratification parameter  $S$  are chalked out in Figs. 6.6(a)-(c). Physically, higher values of the thermal stratification parameter means the fluid present in the lower region becomes more denser. This increase in the density causes a reduction in the convective flow due to which the fluid motion slows down. This



phenomenon is presented in Fig. 6.6(a). To study the impact of thermal stratification parameter  $S$  on temperature and concentration fields, Fig. 6.6(b) and 6.6(c) are drawn. Due to the stratification effect the density of the fluid in the lower region is enhanced. This increase in the density of fluid causes a decline in the temperature difference between the surface at higher temperature and away from the surface. Similarly concentration profile is also declined due to decline in the concentration difference between the higher concentration surface and away from the surface. This phenomenon is evident from the Figs. 6.6(b)-(c).

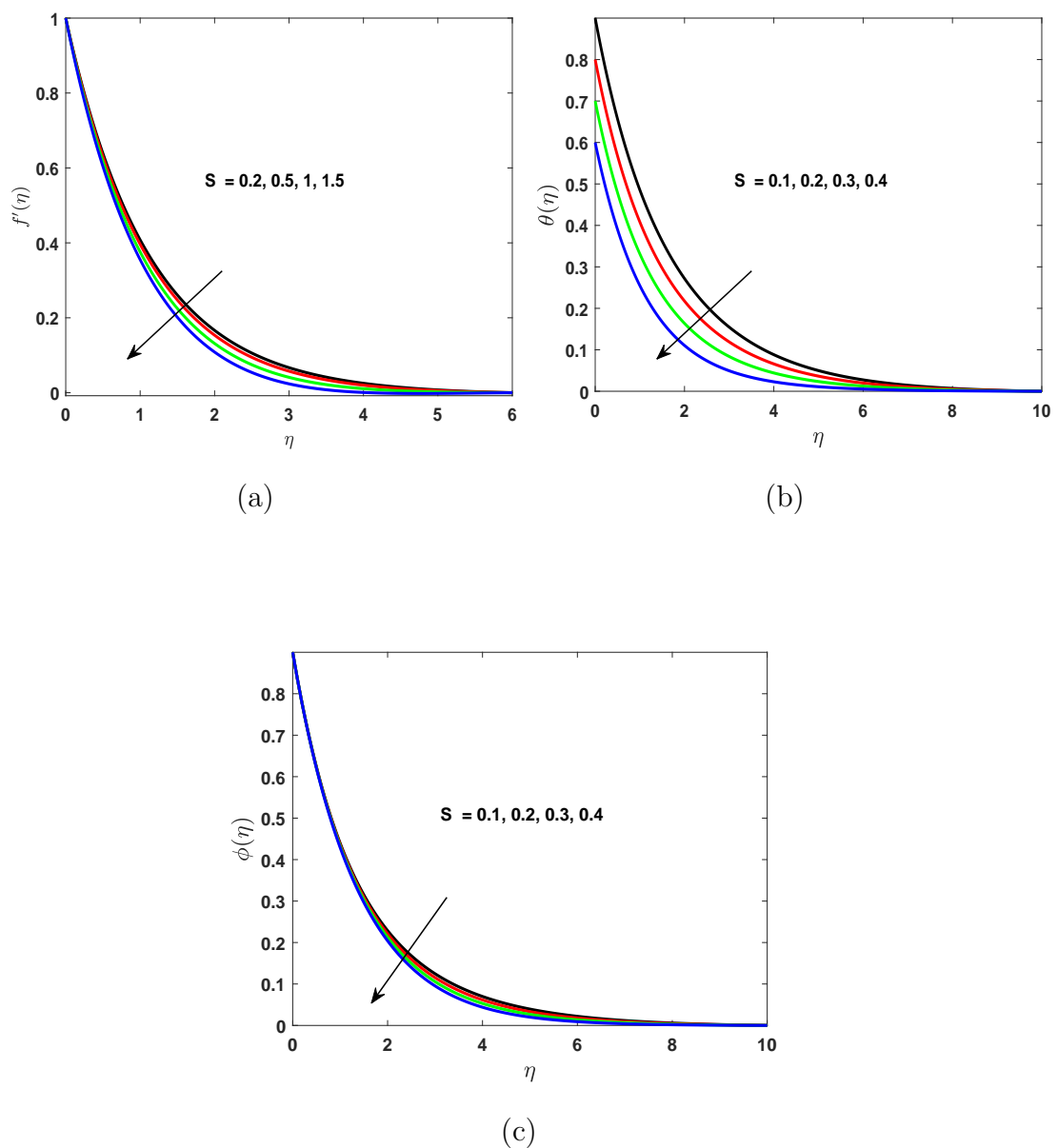


**Fig. 6.6:** Impact of  $S$  on (a) velocity, (b) temperature and (c) concentration profile.

### 6.3.10 Effect of Thermal Radiation Parameter $Rd$

Figs. 6.7(a)-(b) are depicted to visualize the behaviour of the thermal and concentration profile due to deviation in the thermal radiation  $Rd$ . The dimensionless energy field is upsurged as  $Rd$  is raised which is shown in Fig. 6.7(a). Physically, it strengthens the fact that more heat is produced due in the radiation process. Fig. 6.7(b) is illustrated to analyze the impact of  $Rd$  on the dimensionless concentration field. Graphs of this figure indicate that concentration distribution is reduced as  $Rd$  is hiked.

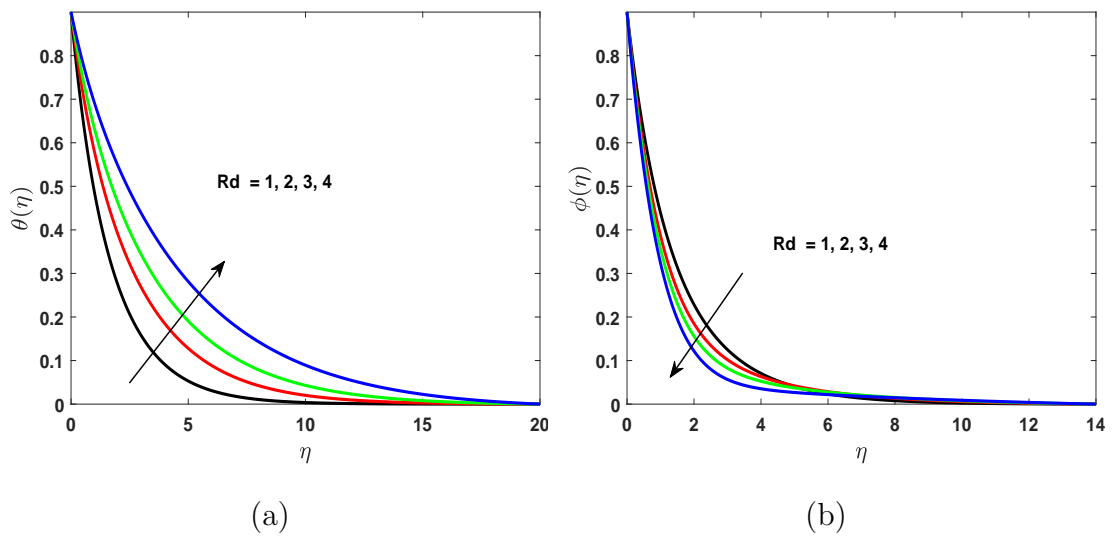


**Fig. 6.7:** Impact of  $Rd$  on (a) temperature and (b) concentration profile.

### 6.3.11 Effect of Thermophoresis Parameter $Nt$

In thermophoresis the particles at higher temperature are pulled away to the colder region, which increases the fluid temperature. Fig. 6.8(a) is chalked out to visualize the fluctuations in the temperature due to the thermophoresis parameter  $Nt$ . This figure indicates that the temperature profile is heightened as the  $Nt$  is increased. The impact of  $Nt$  on concentration is sketched in Fig. 6.8(b). These curves show that concentration profile is hiked for the accelerating values of  $Nt$ . Fig. 6.8(c) is illustrated to visualize the impact of the thermophoresis parameter

$Nt$  on motile density profile. An acclivity in the thermophoresis parameter  $Nt$  causes an augmentation in the motile density profile.

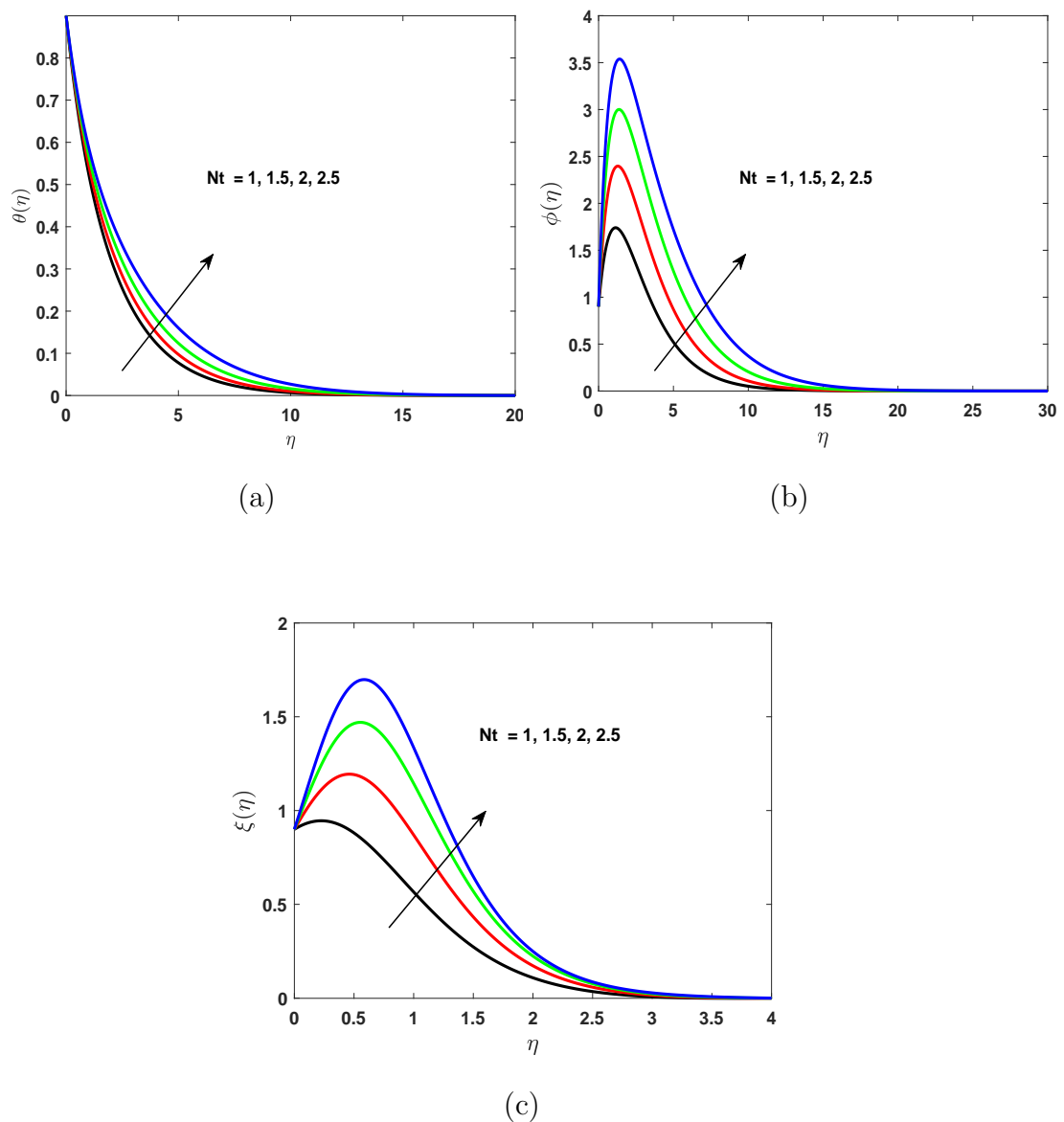


**Fig. 6.8:** Impact of  $Nt$  on (a) temperature, (b) concentration and (c) motile density profile.

### 6.3.12 Effect of Brownian Motion Parameter $Nb$

The temperature is proportional to the speed. When the speed of the nanoparticles is increased, the kinetic energy is increased due to which the temperature of the fluid is enhanced. To support that phenomenon Fig. 6.9(a) is drawn. Fig. 6.9(b)

is chalked out to visualize the effect of the Brownian motion parameter  $Nb$  on concentration profile. An acclivity in  $Nb$  causes a decrement in concentration profile. Physically, the Brownian motion heats up the fluid and also aggravates the particles away from the fluid regime, therefore a decrement is seen in concentration profile. To visualize the influence of the dimensionless Brownian motion parameter  $Nb$  on motile density profile  $\xi$ , Fig. 6.9(c) is sketched. An increment in the random motion of the particles also decreases the dimensionless motile density profile.

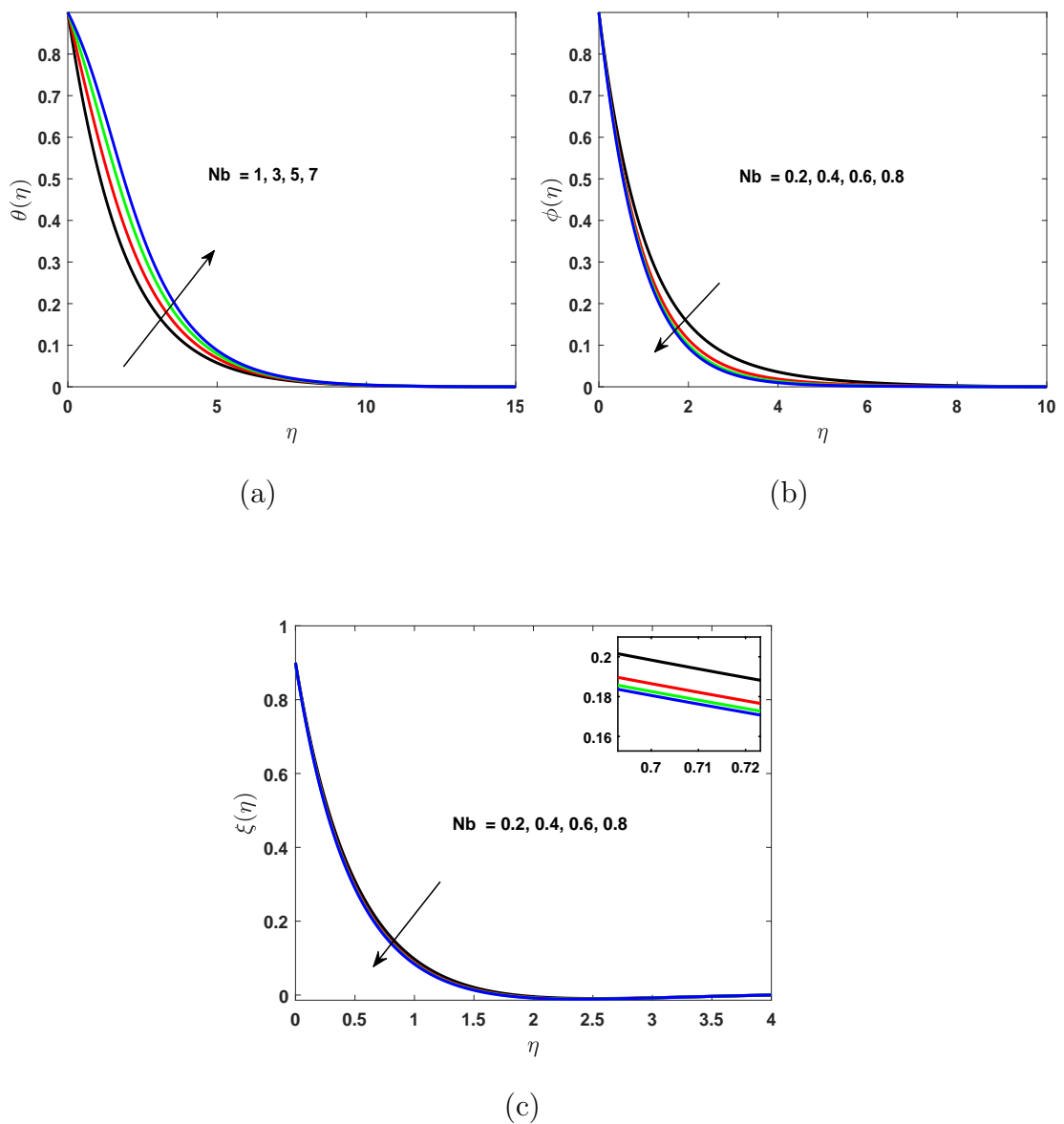
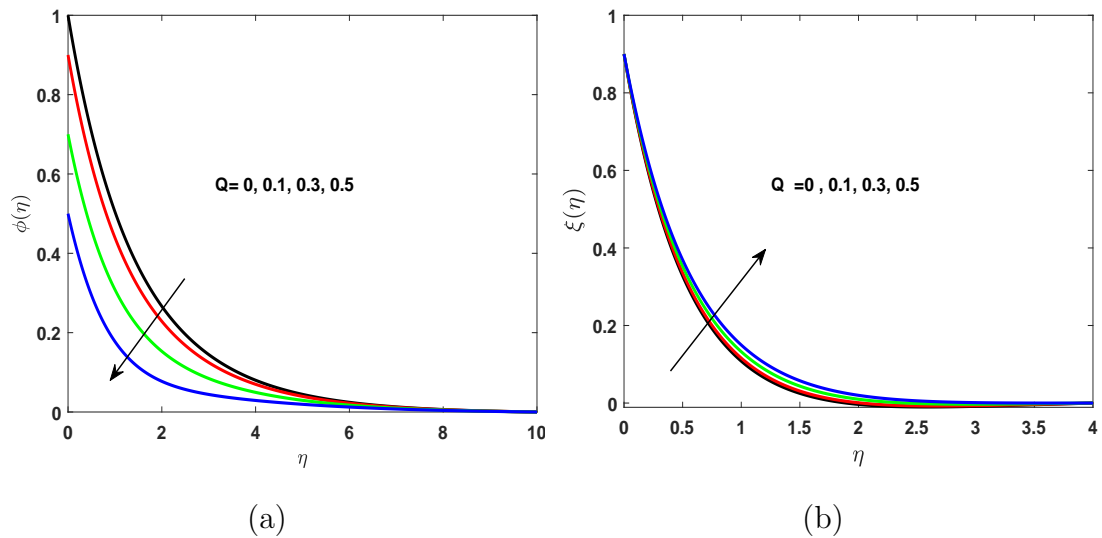


Fig. 6.9: Impact of  $Nb$  on (a) temperature, (b) concentration and (c) motile density profile.

### 6.3.13 Effect of Mass Stratification Parameter $Q$

Fig. 6.10(a) is drawn to study the fluctuation in concentration field due to increment in the mass stratification parameter  $Q$ . An enhancement in  $Q$  causes a diminution in the concentration profile. An acclivity in the mass stratification parameter  $Q$  causes an increment in the motile density profile as shown in the Fig. 6.10(b). Physically, intensifying the mass stratification parameter  $Q$  reduces the nanoparticles concentration between the surface and away from surface due to which concentration profile is declined whereas the density profile is hiked.



**Fig. 6.10:** Impact of  $Q$  on (a) temperature and (b) concentration profile.

### 6.3.14 Effect of Concentration Difference Parameter $\Omega$ and Peclet Number $Pe$

In Fig. 6.11(a), the effect of the concentration difference parameter  $\Omega$  on motile density profile is analyzed. It is noticed that the amplifying  $\Omega$  causes a decline in the density profile. The motile density profile is decreased as the Peclet number  $Pe$  is enhanced. This phenomenon as represented in Fig. 6.11(b). Gradually mounting values of  $Pe$  result a decrement in the diffusivity of the micro-organism due to which the motile density profile is diminished. It is due to the reason that the fluid particles motion increases as the Peclet number is enhanced.

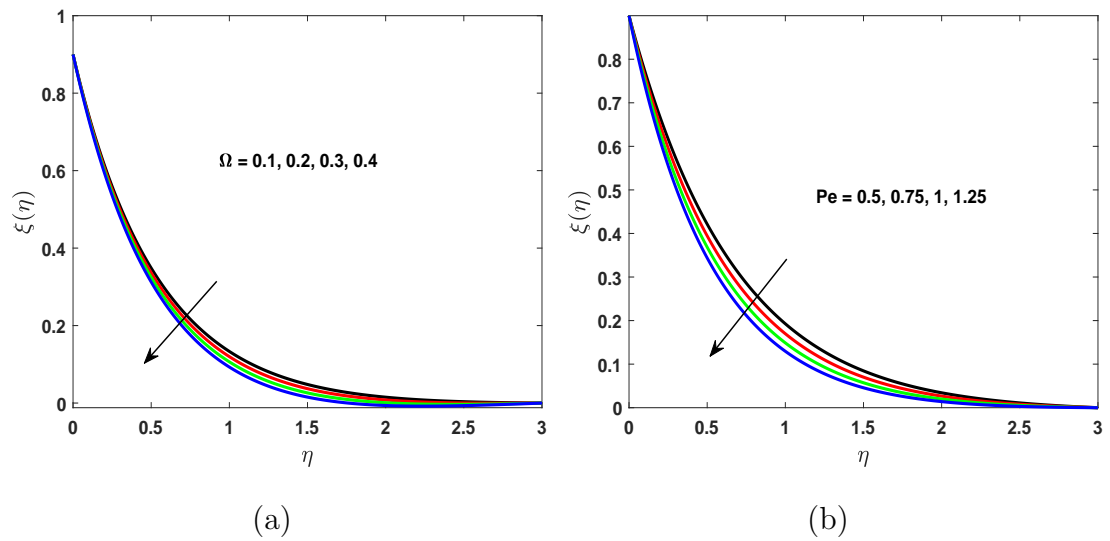


**Fig. 6.11:** Impact of  $\Omega$  and  $Pe$  on concentration profile.

## 6.4 Conclusions

In this chapter, two dimensional magnetohydrodynamic micropolar nanofluid with gyrotactic micro-organism has been analyzed. Some of the key findings are:

- Both the axial velocity and the angular velocity is increased as the material parameter  $K$  are upsurged but a decrement is noticed for the magnetic number  $M$ .
- The energy profile is enhanced for an acclivity in the buoyancy ratio parameter  $Nr$ , the thermophoresis parameter  $Nt$  and the thermal radiation parameter  $Rd$ .
- A decline in the concentration profile is noticed for an acclivity in the Brownian motion parameter  $Nb$ , the mix convection parameter  $\lambda^*$  and the thermal stratification parameter  $S$ .
- A diminution in energy profile is seen as thermal stratification parameter  $S$  and the material parameter  $K$  is enhanced.

- The density profile is upsurged for an enhancement in each of the mass stratification parameter  $Q$  and the buoyancy ratio parameter  $Nr$  whereas opposite trend is noticed as the concentration difference parameter  $\Omega$ , the Peclet number  $Pe$  and the mixed convection parameter  $\lambda^*$ .

# Chapter 7

## Conclusions and Future Work

### 7.1 Conclusions

In this dissertation, the numerical analysis of nonlinear differential equations, governing the flow problems of some non-Newtonian fluids past through different geometries along with some realistic effects have been presented. Regarding the nanofluid, the Buongiorno model has been used to study the flow field and heat transfer. Governing equations of the modeled problems are based on the conservation laws under the boundary layer approximation. With the assistance of appropriate similarity transformation, the governing set of PDEs are rendered into the coupled nonlinear ODEs. The solution of the resulting ODEs in all cases are obtained by the utilization of the well known shooting technique. Furthermore, for all presented problems, an authentication of the computed results is obtained through benchmark with the published results in literature. Graphs of the prominent parameters has been displayed and discussed. Engineering and industrial quantities of interest like local skin friction, local heat and mass transfer rates have been computed and discussed in detail. Some of the key findings are:

- The velocity field is declined for an enhancement in the magnetic number  $M$  in stretching sheet whereas it is enhanced for squeezed channel and wedge shape geometry.



- The temperature distribution is augmented for an increment in the thermal radiation parameter  $Rd$  and Weissenberg number  $We$ .
- The velocity field is diminished for rising values of the power-law index  $n$  for the squeezed channel and stretching sheet where as it is enhanced for wedge shape geometry.
- The Nusselt and Sherwood numbers are diminished for the increasing values of the Hartree pressure gradient  $\beta$ .
- The temperature profile is enhanced and concentration profile is declined as the Brownian motion parameter  $Nb$  is enhanced.
- Both energy and concentration profile is enhanced for an accelerating values of  $Nt$  in all geometries.
- In squeezed channel velocity profile is declined and temperature profile is enhanced for suction whereas reverse trend is observed for injection.
- The energy profile is enhanced for an increment in the power-law index  $n$  for squeezed channel and stretching sheet where as it is depressed for wedge shape geometry.
- The concentration profile is enhanced for the increasing values of the power-law index  $n$  for wedge geometry whereas it declined for stretching sheet.
- The density profile is upsurged for an enhancement in each of the mass stratification parameter  $Q$  and the buoyancy ratio parameter  $Nr$  whereas opposite trend is noticed as the concentration difference parameter  $\Omega$ , the Peclet number  $Pe$  and the mixed convection parameter  $\lambda^*$  and thermal conductivity parameter  $\epsilon$

## 7.2 Future Work

The work of this dissertation emphasised on the heat and mass transfer analysis of the some non-Newtonian fluids. The presented work in this thesis can be extended in many directions. Few of them are as follows:

- In Chapter 3, we have considered the Carreau fluid. The same problem can be modeled for the different fluid models like Casson fluid, tangent hyperbolic fluid, micropolar fluid, Sisko fluid etc.
- The articles mentioned in Chapter 3 can be extended with some other effects such as internal heating, viscous dissipation, non-linear thermal radiation, activation energy etc.
- It will be very interesting to solve the problem of Chapter 3 by taking blood as base fluid with different nanoparticles like gold, silver copper etc.
- The problem of Chapter 4 and 5 can be extended for some other parameters like electrical magnetohydrodynamics, exponential space dependent heat source, bioconvection, cross-diffusion effects etc.
- Chapter 6 can be extended by using non Fourier law, nonlinear thermal radiation, oxytactic micro-organism, quartic autocatalysis etc.
- The model of Chapter 6 can be analyzed with different fluid models.
- Different geometries can be considered like permeable surfaces, rotating geometries, cylinder etc.

# Bibliography

- [1] T. S. Gregory, R. Cheng, G. Tang, L. Mao, and Z. T. H. Tse, “The magnetohydrodynamic effect and its associated material designs for biomedical applications: A state-of-the-art review,” *Advanced Functional Materials*, vol. 26(22), pp. 3942–3952, 2016.
- [2] T. S. Kumar and B. R. Kumar, “Effect of homogeneous-heterogeneous reactions in MHD stagnation point nanofluid flow towards a cylinder with nonuniform heat source or sink,” *Trends in Mathematics*, pp. 287–299, 2019.
- [3] S. A. Gaffar, V. R. Prasad, and O. A. Beg, “Numerical study of flow and heat transfer of non-Newtonian tangent hyperbolic fluid from a sphere with Biot number effects,” *Alexandria Engineering Journal*, vol. 54(4), pp. 829–841, 2015.
- [4] V. R. Prasad, S. A. Gaffar, and O. A. Beg, “Free convection flow and heat transfer of tangent hyperbolic fluid past a vertical porous plate with partial slip,” *Journal of Applied Fluid Mechanics*, vol. 9, pp. 1667–1678, 2016.
- [5] K. G. Kumar, R. G. K., and B. J. Gireesha, “Melting heat transfer of tangent hyperbolic fluid over a stretching sheet with fluid particle suspension and thermal radiation,” *Communications in Numerical Analysis*, vol. 2017(2), pp. 125–140, 2017.
- [6] W. Ibrahim, “Magnetohydrodynamics (MHD) flow of a tangent hyperbolic fluid with nanoparticles past a stretching sheet with second order slip and convective boundary condition,” *Results in Physics*, vol. 7, pp. 3723–3731, 2017.

- 
- [7] T. Salahuddin, M. Y. Malik, A. Hussain, M. Awais, I. Khan, and M. Khan, “Analysis of tangent hyperbolic nanofluid impinging on a stretching cylinder near the stagnation point,” *Results in Physics*, vol. 7, pp. 426–434, 2017.
- [8] A. Hussain, M. Malik, T. Salahuddin, and M. K. A. Rubab, “Effects of viscous dissipation on (MHD) tangent hyperbolic fluid over a nonlinear stretching sheet with convective boundary conditions,” *Results in Physics*, vol. 7, pp. 3502–3509, 2017.
- [9] T. Hayat, M. Waqas, A. Alsaedi, G. Bashir, and F. Alzahrani, “Magneto-hydrodynamic (MHD) stretched flow of tangent hyperbolic nanoliquid with variable thickness,” *Journal of Molecular Liquids*, vol. 229, pp. 178–184, 2017.
- [10] V. Nagendramma, A. Leelarathnam, C. S. K. Raju, S. A. Shehzad, and T. Hussain, “Doubly stratified MHD tangent hyperbolic nanofluid flow due to permeable stretched cylinder,” *Results in Physics*, vol. 9, pp. 23–32, 2018.
- [11] J. M. J. Uddin and S. T. Thoroddsen, “Squeeze flow of a Carreau fluid during sphere impact,” *AIP Advances*, vol. 24(7), 2012.
- [12] T. Hayat, S. Asad, M. Mustafa, and A. Alsaedi, “Boundary layer flow of Carreau fluid over a convectively heated stretching sheet,” *Applied Mathematics and Computations*, vol. 246, pp. 12–22, 2014.
- [13] M. Khan and Hashim, “Boundary layer flow and heat transfer to Carreau fluid over a nonlinear stretching sheet,” *AIP Advances*, vol. 5, 107203, 2015.
- [14] B. Ramadevi, V. Sugunamma, K. A. Kumar, and J. R. Reddy, “MHD flow of Carreau fluid over a variable thickness melting surface subject to Cattaneo-Christov heat flux,” *Multidiscipline Modeling in Materials and Structures*, vol. 15(1), pp. 2–25, 2018.
- [15] M. I. Khan, A. Kumar, T. Hayat, M. Waqas, and R. Singh, “Entropy generation in flow of Carreau nanofluid,” *Journal of Molecular Liquids*, vol. 278, pp. 677–687, 2019.

- 
- [16] A. C. Eringen, "Theory of micropolar fluids," *International Journal of Mathematics and Mechanics*, vol. 16, pp. 1–18, 1966.
- [17] A. C. Eringen, "Theory of thermomicrofluids," *Journal of Mathematical Analysis and Applications*, vol. 38(2), pp. 480–496, 1972.
- [18] V. M. Soundalgekar and H. S. Takhar, "Flow of micropolar fluid past a continuously moving plate," *International Journal of Engineering Science*, vol. 21(8), pp. 961–965, 1983.
- [19] C. Perdikis and A. Raptis, "Heat transfer of a micropolar fluid by the presence of radiation," *Heat and Mass Transfer*, vol. 31, pp. 381–382, 1996.
- [20] A. Ishak, "Thermal boundary layer flow over a stretching sheet in a micropolar fluid with radiation effect," *International Journal of Heat and Mass transfer*, vol. 45(3), pp. 367–373, 2010.
- [21] J. V. R. Murthy, K. S. Sai, and N. K. Bahali, "Steady flow of micropolar fluid in a rectangular channel under transverse magnetic field with suction," *AIP Advances*, vol. 1, 032123, 2011.
- [22] N. T. Eldabe, A. Y. Ghaly, R. R. Rizkallah, K. M. Ewis, and A. S. Al-Bareda, "Numerical solution of MHD flow of micropolar fluid with heat and mass transfer towards a stagnation point on a vertical plate," *American Journal of Computational Mathematics*, vol. 5, pp. 158–174, 2015.
- [23] K. Das and A. Sarkar, "Effect of melting on a MHD micropolar fluid flow towards a shrinking sheet with thermal radiation," *Journal of Applied Mechanics and Technical Physics*, vol. 57(4), pp. 681–689, 2016.
- [24] M. Bilal, S. Hussain, and M. Sagheer, "Boundary layer flow of magneto-micropolar nanofluid flow with Hall and ion-slip effects using variable thermal diffusivity," *Bulletin of the Polish Academy of Sciences*, vol. 65(3), 2017.
- [25] K. L. Hsiao, "Micropolar nanofluid flow with MHD and viscous dissipation effects towards a stretching sheet with multimedia feature," *International Journal of Heat and Mass Transfer*, vol. 112, pp. 983–990, 2017.

- [26] H. Alfven, "Existence of electromagnetic-hydrodynamic waves," *Nature*, vol. 150(3850), pp. 405–406, 1942.
- [27] M. H. Yazdi, S. Abdullah, I. Hashim, and K. Sopian, "Effects of viscous dissipation on the slip MHD flow and heat transfer past a permeable surface with convective boundary conditions," *energies*, vol. 4, pp. 2273–2294, 2011.
- [28] L. Zheng, J. Niu, X. Zhang, and Y. Gao, "MHD flow and heat transfer over a porous shrinking surface with velocity slip and temperature jump," *International Journal of Biomathematics*, vol. 56(5-6), pp. 133–144, 2012.
- [29] K. Bhattacharyya, "MHD stagnation-point flow of Casson fluid and heat transfer over a stretching sheet with thermal radiation," *Journal of Thermodynamics*, vol. 2013, 2013.
- [30] D. S. Chauhan and R. Agrawal, "MHD flow and heat transfer in a channel bounded by a shrinking sheet and a porous medium bed," *International Scholarly Research Notices*, vol. 2013, 2013.
- [31] M. Fathizadeh, M. Madani, Y. Khan, N. Faraz, A. Yildirim, and S. Tutkun, "An effective modification of the homotopy perturbation method for MHD viscous flow over a stretching sheet," *Journal of King Saud University Science*, vol. 25, pp. 107–113, 2013.
- [32] S. Abbasbandy, T. Hayat, A. Alsaedi, and M. Rashidi, "Numerical and analytical solutions for Falkner-Skan flow of MHD Oldroyd-B fluid," *International Journal of Numerical Methods for Heat and Fluid Flow*, vol. 24(2), pp. 390–401, 2014.
- [33] S. Das, R. N. Jana, and O. D. Makinde, "Magnetohydrodynamic mixed convective slip flow over an inclined porous plate with viscous dissipation and Joule heating," *Alexandria Engineering Journal*, vol. 54(2), pp. 251–261, 2015.

- [34] S. Khalili, H. Tamim, A. Khalili, and M. M. Rashidi, “Unsteady convective heat and mass transfer in pseudoplastic nanofluid over a stretching wall,” *Advanced Powder Technology*, vol. 26(5), pp. 1319–1326, 2015.
- [35] S. Hussain, “Finite element solution for MHD flow of nanofluids with heat and mass transfer through a porous media with thermal radiation, viscous dissipation and chemical reaction effects,” *Advances in Applied Mathematics and Mechanics*, vol. 9(4), pp. 904–923, 2017.
- [36] M. Kwak and B. Lkhagvasuren, “Global wellposedness for Hall-MHD equations,” *Nonlinear Analysis*, vol. 174, pp. 104–117, 2018.
- [37] A. Rahbari, M. Abbasi, I. Rahimipetroudi, B. Sunden, D. D. Ganji, and M. Gholami, “Heat transfer and MHD flow of non-Newtonian Maxwell fluid through a parallel plate channel: analytical and numerical solution,” *Mechanical Sciences*, vol. 9, pp. 61–70, 2018.
- [38] K. G. Kumar, M. Archana, B. J. Giresha, M. R. Krishnamurthy, and N. G. Rudraswamy, “Cross diffusion effect on MHD mixed convection flow of non-linear radiative heat and mass transfer of Casson fluid over a vertical plate,” *Results in Physics*, vol. 8, pp. 694–701, 2018.
- [39] S. U. S. Choi and J. A. Eastman, “Enhancing thermal conductivity of fluids with nanoparticles,” *ASME Fluids Engineering*, vol. 231, pp. 99–105, 1995.
- [40] F. Garoosi, F. Hoseininejad, and M. M. Rashidi, “Numerical study of natural convection heat transfer in a heat exchanger filled with nanofluids,” *Energy*, vol. 109, pp. 664–678, 2016.
- [41] R. S. Raju, G. J. Reddy, J. A. Rao, M. M. Rashidi, and R. S. R. Gorla, “Analytical and numerical study of unsteady MHD free convection flow over an exponentially moving vertical plate with heat absorption,” *International Journal of Thermal Sciences*, vol. 107, pp. 303–315, 2016.

- [42] A. Kamran, S. Hussain, M. Sagheer, and N. Akmal, "A numerical study of magnetohydrodynamics flow in Casson nanofluid combined with Joule heating and slip boundary conditions," *Results in Physics*, vol. 7, pp. 3037–3048, 2017.
- [43] M. M. Rashidi and M. A. Abbas, "Effect of slip conditions and entropy generation analysis with an effective Prandtl number model on a nanofluid flow through a stretching sheet," *Entropy*, vol. 19(8), pp. 414–429, 2017.
- [44] S. K. Soid, A. Ishak, and I. Pop, "Boundary layer flow past a continuously moving thin needle in a nanofluid," *Applied Thermal Engineering*, vol. 114, pp. 58–64, 2017.
- [45] M. Fakour, A. Rahbari, E. Khodabandeh, and D. D. Ganji, "Nanofluid thin film flow and heat transfer over an unsteady stretching elastic sheet by LSM," *Journal of Mechanical Science and Technology*, vol. 32(1), pp. 177–183, 2018.
- [46] N. Akmal, M. Sagheer, and S. Hussain, "Numerical study focusing on the entropy analysis of MHD squeezing flow of a nanofluid model using Cattaneo-Christov theory," *AIP Advances*, vol. 8, 055201, 2018.
- [47] T. Sajid, M. Sagheer, S. Hussain, and M. Bilal, "Darcy-Forchheimer flow of Maxwell nanofluid flow with nonlinear thermal radiation and activation energy," *AIP Advances*, vol. 8, 035102, 2018.
- [48] R. Mohebbi, M. M. Rashidi, M. Izadi, N. A. C. Sidik, and H. W. Xian, "Forced convection of nanofluids in an extended surfaces channel using lattice Boltzmann method," *International Journal of Heat and Mass Transfer*, vol. 117, pp. 1291–1303, 2018.
- [49] M. M. Rashidi, Z. Yang, M. Awais, M. Nawaz, and T. Hayat, "Generalized magnetic field effects in Burgers nanofluid model," *PLoS ONE*, vol. 2(1): e 0168923, 2017.
- [50] Y. Feng and C. Kleinstreuer, "Nanofluid convective heat transfer in a parallel-disk system," *International Journal of Heat and Mass Transfer*, vol. 53(21-22), pp. 4619–4628, 2010.



- [51] G. J. Reddy, M. Kumar, B. Kethireddy, and A. Chamka, “Colloidal study of unsteady magnetohydrodynamic couple stress fluid flow over an isothermal vertical flat plate with entropy heat generation,” *Journal of Molecular Liquids*, vol. 253, pp. 169–179, 2018.
- [52] S. Bhattacharyya and S. K. Pal, “Enhanced electroosmotic flow in a nano-channel patterned with curved hydrophobic strips,” *Applied Mathematical Modelling*, vol. 54, pp. 567–579, 2018.
- [53] K. Hiemenz, “Die Grenzschicht an einem in den gleichförmigen Flüssigkeitsstrom eingetauchten geraden Kreiszyylinder,” Ph.D. dissertation, 1911.
- [54] I. S. Awaludin, P. D. Weidman, and A. Ishak, “Stability analysis of stagnation point flow over a stretching/shrinking sheet,” *AIP Advances*, vol. 6, 045308, 2016.
- [55] J. Merkina and I. Pop, “Stagnation point flow past a stretching/shrinking sheet driven by Arrhenius kinetics,” *Applied Mathematics and Computation*, vol. 337, pp. 583–590, 2018.
- [56] I. Pop, N. C. Roca, and A. V. Roca, “MHD stagnation-point flow and heat transfer of a nanofluid over a stretching/shrinking sheet with melting, convective heat transfer and second-order slip,” *International Journal of Numerical Methods for Heat and Fluid Flow*, vol. 28(9), pp. 2089–2110, 2018.
- [57] T. M. Agbaje, S. Mondal, Z. G. Makukula, S. S. Motsa, and P. Sibanda, “A new numerical approach to MHD stagnation point flow and heat transfer towards a stretching sheet,” *Ain Shams Engineering Journal*, vol. 9 (2), pp. 233–243, 2018.
- [58] M. M. Bhatti, M. A. Abbas, and M. Rashidi, “A robust numerical method for solving stagnation point flow over a permeable shrinking sheet under the influence of MHD,” *Applied Mathematics and Computation*, vol. 316, pp. 381–389, 2018.

- [59] B. I. Olajuwon, "Convection heat and mass transfer in a hydromagnetic flow of a second grade fluid in the presence of thermal radiation and thermal diffusion," *International Communications in Heat and Mass Transfer*, vol. 38, pp. 377–382, 2011.
- [60] R. Choudhury and S. K. Das, "Visco-elastic MHD free convective flow through porous media in presence of radiation and chemical reaction with heat and mass transfer," *Journal of Applied Fluid Mechanics*, vol. 7(4), pp. 603–609, 2014.
- [61] P. B. A. Reddy, "Magnetohydrodynamic flow of a Casson fluid over an exponentially inclined permeable stretching surface with thermal radiation and chemical reaction," *Ain Shams Engineering Journal*, vol. 7(2), pp. 593–602, 2016.
- [62] S. Shah, S. Hussain, and M. Sagheer, "MHD effects and heat transfer for the UCM fluid along with Joule heating and thermal radiation using Cattaneo-Christov heat flux model," *AIP Advances*, vol. 6, 2016.
- [63] M. Madhua, N. Kishan, and A. J. Chamkha, "Unsteady flow of a Maxwell nanofluid over a stretching surface in the presence of magnetohydrodynamic and thermal radiation effects," *Propulsion and Power Research*, vol. 6, pp. 31–40, 2017.
- [64] M. F. Endalew and A. Nayak, "Thermal radiation and inclined magnetic field effects on MHD flow past a linearly accelerated inclined plate in a porous medium with variable temperature," *Heat Transfer-Asian Research*, pp. 1–20, 2018.
- [65] M. R. Eid, K. L. Mahny, T. Muhammad, and M. Sheikholeslami, "Numerical treatment for Carreau nanofluid flow over a porous nonlinear stretching surface," *Results in Physics*, vol. 8, pp. 1185–1193, 2018.
- [66] A. R. A. Khaled and K. Vafai, "Hydromagnetic squeezed flow and heat transfer over a sensor surface," *International Journal of Engineering Science*, vol. 42(5-6), pp. 509–519, 2004.

- [67] M. Khan, M. Y. Malik, T. Salahuddin, and I. Khan, "Heat transfer squeezed flow of Carreau fluid over a sensor surface with variable thermal conductivity," *Results in Physics*, vol. 6, pp. 940–945, 2016.
- [68] R. Kandasamy, R. Mohammad, N. A. B. M. Zailani, and N. F. B. Jaafar, "Nanoparticle shapes on squeezed MHD nanofluid flow over a porous sensor surface," *Journal of Molecular Liquids*, vol. 233, pp. 156–165, 2017.
- [69] T. Salahuddin, M. Malik, A. Hussain, S. Bilal, M. Awais, and I. Khan, "MHD squeezed flow of Carreau-Yasuda fluid over a sensor surface," *Alexandria Engineering Journal*, vol. 56, pp. 27–34, 2017.
- [70] A. Hussain, R. Zetoon, S. Ali, and S. Nadeem, "Magnetically driven flow of pseudoplastic fluid across a sensor surface," *Journal of the Brazilian Society of Mechanical Sciences and Engineering*, vol. 41, pp. 185–197, 2019.
- [71] A. V. Kuznetsov, "The onset of nanofluid bioconvection in a suspension containing both nanoparticles and gyrotactic micro-organism," *International Communications in Heat and Mass Transfer*, vol. 37, pp. 1421–1425, 2010.
- [72] A. V. Kuznetsov, "Bio-thermal convection induced by two different species of micro-organism," *International Communications in Heat and Mass Transfer*, vol. 38, pp. 548–553, 2011.
- [73] A. V. Kuznetsov, "Nanofluid bioconvection in porous media: Oxytactic micro-organism," *Journal of Porous Media*, vol. 15, pp. 233–248, 2012.
- [74] H. Xu and I. Pop, "Fully developed mixed convection flow in a horizontal channel filled by a nanofluid containing both nanoparticles and gyrotactic micro-organism," *European Journal of Mechanics - B/Fluids*, vol. 46, pp. 37–45, 2014.
- [75] C. S. K. Raju and N. Sandeep, "Heat and mass transfer in MHD non-Newtonian bio-convection flow over a rotating cone/plate with cross diffusion," *Journal of Molecular Liquids*, vol. 215, pp. 115–126, 2016.

- [76] C. S. K. Raju, M. M. Hoque, and T. Sivasankar, "Radiative flow of Casson fluid over a moving wedge filled with gyrotactic micro-organism," *Advanced Powder Technology*, vol. 28(2), pp. 575–583, 2017.
- [77] E. Ramya, M. Muthtamiselan, and D. H. Doh, "Absorbing/emitting radiation and slanted hydromagnetic effects on micropolar liquid containing gyrostatic micro-organism," *Applied Mathematics and Computation*, vol. 324, pp. 69–81, 2018.
- [78] V. M. Falkner and S. W. Skan, "Some approximate solutions of the boundary-layer equations," *Philosophical Magazine*, vol. 7(12), pp. 865–896, 1931.
- [79] K. R. Rajagopal, A. S. Gupta, and T. Y. Na, "A note on the Falkner-Skan flows of a non-Newtonian fluid," *International journal of Non Linear Mechanics*, vol. 18(4), pp. 313–320, 1983.
- [80] H. T. Lin and L. K. Lin, "Similarity solutions for laminar forced convection heat transfer from wedges to fluids of any Prandtl number," *International Journal of Heat and Mass Transfer*, vol. 30(6), pp. 1111–1118, 1987.
- [81] B. L. Kuo, "Application of the differential transformation method to the solutions of Falkner-Skan wedge flow," *Acta Mechanica*, vol. 164(2-3), pp. 161–174, 2003.
- [82] A. J. Chamkha, M. Mujtaba, A. Quadri, and C. Issa, "Thermal radiation effects on MHD forced convection flow adjacent to a non-isothermal wedge in the presence of a heat source or sink," *Heat and Mass Transfer*, vol. 39(4), pp. 305–312, 2003.
- [83] A. Ishak, R. Nazar, and I. Pop, "Falkner-Skan equation for flow past a moving wedge with suction or injection," *Journal of Applied Mathematics and Computing*, vol. 25 (1-2), pp. 67–83, 2007.
- [84] S. Ganganapalli, S. Kata, and V. Bhumarapu, "Unsteady boundary layer flow of a Casson fluid past a wedge with wall slip velocity," *Journal of Heat and Mass Transfer Research*, vol. 4, pp. 91–102, 2017.

- [85] <http://www.freestudy.co.uk/fluid%20mechanics/t3203.pdf>.
- [86] T. C. Papanastasiou, G. C. Georgiou, and A. N. Alexandrou, *Viscous Fluid Flow*. LLC, 2000 N.W. Corporate Blvd., Boca Raton, Florida: CRC Press, 1999.
- [87] R. Chhabra and J. Richardson, *Non-Newtonian Flow and Applied Rheology (Second Edition)*. Butterworth-Heinemann, 2008.
- [88] J. A. Eastman, S. R. Phillpot, S. U. S. Choi, and P. Keblinski, “Thermal transport in nanofluids,” *Annual Review of Materials Research*, vol. 34, pp. 219–246, 2004.
- [89] J. Buongiorno, “Convective transport in nanofluids,” *ASME Journal Heat Transfer Transactions*, vol. 128(3), pp. 240–250, 2006.
- [90] [https://warwick.ac.uk/fac/sci/physics/research/cfsa/people/valery/teaching/px420/addres/mhd int1.pdf](https://warwick.ac.uk/fac/sci/physics/research/cfsa/people/valery/teaching/px420/addres/mhd%20int1.pdf).
- [91] P. G. Gopinath, S. A. Mastani, and V. R. Anitha, “Mems microcantilevers sensor modes of operation and transduction principles,” *International Journal of Computer Engineering Science*, vol. 4(2), 2014.
- [92] T. Y. Na, *Computational Methods in Engineering Boundary Value Problems*. Academic Press, 1979, vol. 145.
- [93] A. V. Kuznetsov and D. A. Nield, “The Cheng-Minkowycz problem for natural convective boundary layer flow in a porous medium saturated by a nanofluid: A revised model,” *International Journal of Heat and Mass Transfer*, vol. 65, pp. 682–685, 2013.
- [94] T. Hayat, R. Sajjad, T. Muhammad, A. Alsaedi, and R. Ellahi, “On MHD nonlinear stretching flow of Powell-Eyring nanomaterial,” *Results in Physics*, vol. 7, pp. 535–543, 2017.
- [95] N. S. Khashiie, N. M. Arifin, R. Nazar, E. H. Hafidzuddin, N. Wahi, and I. Pop, “A stability analysis for magnetohydrodynamics stagnation point flow

with zero nanoparticles flux condition and anisotropic slip,” *energies*, vol. 12(7), 2019.